# Model inference and uncertainty quantification in complex resistivity imaging

**Dissertation**

zur Erlangung des Doktorgrades (Dr. rer. nat)
der Mathematisch-Naturwissenschaftlichen Fakultät
der Rheinischen Friedrich-Wilhelms-Universität Bonn

vorgelegt von

**Joost Hase**

aus
Steinheim, Deutschland

Bonn, 2025

Angefertigt mit Genehmigung der
Mathematisch-Naturwissenschaftlichen Fakultät
der Rheinischen Friedrich-Wilhems-Universität Bonn

Gutachter / Betreuer: Prof. Dr. Andreas Kemna
Gutachter: Prof. Dr. Florian Wagner

Tag der Promotion: 22. Oktober 2025

Erscheinungsjahr: 2026

# Summary

The objective of this thesis is to contribute to the solution of the complex resistivity imaging problem by introducing an inversion workflow that emphasizes accurate model inference and uncertainty quantification in a probabilistic framework. Complex resistivity imaging is a frequency-domain technique for the analysis of tomographic induced polarization measurements, inferring the complex electrical conductivity distribution in the subsurface at a specific frequency from measurements of the complex electrical impedance. Applications can be found across earth sciences and include hydrogeological characterization, investigation of permafrost dynamics, monitoring of contaminated sites, mineral exploration, and more. As earth scientists gain a better understanding of how the macroscopic electrical conduction and polarization properties of earth materials relate to the structures and mechanisms at the pore scale, imaging techniques must meet the increasing demand for accuracy and uncertainty quantification. This is necessary to ensure that advances made in laboratory studies translate into improved interpretations of tomographic resistivity and induced polarization measurements in the field.

Resistivity and induced polarization measurements can be performed in the time domain and in the frequency domain. Although there has been an increase in the practical utilization of frequency-domain measurements during recent years, time-domain measurements remain the predominant methodology used in field surveys. In order to analyze time-domain induced polarization measurements using complex resistivity imaging, a suitable approach for converting time-domain voltage transients into frequency-domain spectra of complex electrical impedance is essential. Besides the extraction of spectral information from time-domain measurements, an appropriate conversion approach must also allow for an accurate propagation of uncertainties. The first contribution of this thesis is such a conversion approach, which is based on the Debye decomposition of the transients into relaxation-time distributions and the subsequent calculation of the equivalent spectra. The conversion scheme is tested in a synthetic study, confirming the accuracy of the extracted spectral information and the validity of the propagated uncertainties. Based on a tomographic time-domain induced polarization data set from Kamchatka (Russia), the application of the conversion approach to field measurements is demonstrated, followed by the inversion of the obtained complex electrical impedances into subsurface images of complex electrical conductivity at different

frequencies, using the established deterministic approach to complex resistivity imaging.

The second contribution of this thesis introduces a probabilistic framework for the solution of non-linear geophysical inverse problems in complex variables, specifically focusing on the application to complex resistivity imaging. By formulating the likelihood and prior terms as complex probability distributions and combining them into a posterior distribution using Bayes' theorem, the approach can simultaneously account for individual data errors of the real and imaginary data parts, independently regularize the real and imaginary parts of the complex model, and still take into account cross-sensitivities that originate from a complex forward calculation. The introduced framework reduces to the established deterministic inversion approach in complex variables under simplifying assumptions with regard to data errors and regularization characteristics, thereby offering theoretical insight into the positioning of the established inversion approach in a broader probabilistic context. The complex conductivity image with the highest probability under the posterior distribution is determined by means of optimization, using a Gauss-Newton scheme that operates in complex variables. Based on the estimated maximum a posteriori solution, the variances and covariances of the inversion result are approximated locally under the simplifying assumption of a linearized forward calculation and normally distributed model parameters. In a synthetic study, the advantages of the probabilistic framework over the established inversion approach are demonstrated.

In the third contribution of this thesis, the probabilistic framework is used as the basis for a probabilistic inversion of complex resistivity measurements using the Hamiltonian Monte Carlo method, aiming at a comprehensive characterization of the posterior distribution and an accurate global uncertainty quantification, both of which have not been fully achieved within the second contribution. As complex resistivity imaging is associated with a tomographic inverse problem that is non-linear, of high dimension and features strong correlations between model parameters, sampling from the posterior distribution is challenging. Hamiltonian Monte Carlo is a Markov chain Monte Carlo method that is suited to meet this challenge, as it incorporates gradient information on the negative log-posterior into a random walk to achieve efficient model updates. Using a variant of Hamiltonian Monte Carlo called the No-U-Turn sampler, a representative sample can be obtained for the complex resistivity imaging problem, as demonstrated in an exemplary study. Convergence criteria are monitored to assess the quality of the probabilistic inversion result, and the final sample is analyzed with regard to the expected complex conductivity image, global variances and covariances, as well as Spearman correlations between the inferred model parameters. Based on the Hamiltonian Monte Carlo inversion result, the validity of the locally approximated variances and covariances obtained on the basis of the deterministic inversion result is assessed, and deviations between the expected image and the maximum a posteriori solution are interpreted in the context of non-linearity.

The collective contribution of this thesis is an enhanced workflow for complex resistivity imaging based on time-domain and frequency-domain induced polarization measurements. It allows for an improved quantitative interpretability of derived complex conductivity images with respect to target parameters and a more reliable assessment of their uncertainty.

# Acknowledgments

I want to use this opportunity to thank Andreas Kemna for giving me the chance to pursue the research that forms the basis of this thesis within the Geophysics Group at the University of Bonn and for supervising my studies. Furthermore, I am very grateful for having had the possibility to publish alongside my other co-authors Maximilian Weigand, Florian Wagner, Konstantin Titov and Grigori Gurin, who greatly supported the results presented in this thesis by contributing their insight of geophysical inverse modeling and induced polarization measurements.

Going through the excitement and struggles of writing a dissertation is easier when you have good companions along the way. I was very lucky to share this time with my fellow students Arne Mansfeld, Valentin Michels, Jonas Limbrock, Daria Pankova and Larissa Reineccius. I also want to thank my other colleagues in the working group, Niklas Heidemann, Anna Zoporowski, Lisa Takacs, Dirk Handwerk, Kristoffer Kerkhof and Daniela Domgörgen, who helped me to overcome the daily problems of university business, while also creating a fun and supportive working environment.

Finally, I want to thank my friends and family, who supported me during this journey.

Joost Hase

February 10, 2025
Bonn, Germany

*Gewidmet meinem Opa Rudi Hase.*

# Contents

# CHAPTER 1

# Introduction

## 1.1 Motivation

A comprehensive understanding of the characteristics and mechanisms that control the Earth system is crucial to successfully address the environmental challenges of the future. Due to the high complexity and interconnectedness of environmental processes, earth scientists must work together to provide a scientific basis for political, social and technological advancement. The role of applied geophysics is to provide (quantitative) information on the state of the subsurface and the processes that control its change over time. In geophysical imaging, this information is inferred from indirect measurements of the subsurface's macroscopic physical properties, which are closely related to lithological, geochemical, hydrological, and petrophysical parameters of interest. Geophysical measurements play a role in many disciplines across earth and climate sciences (e.g., Kneisel et al. 2008; Krautblatter et al. 2010; Wenzel et al. 2024), as well as agriculture (e.g., Ehosioke et al. 2020) and archaeology (e.g., Griffiths and Barker 1994). All these disciplines profit from the non-invasive nature and effectiveness of geophysical methods. Across applications, researchers highlight the need for an improved accuracy and uncertainty quantification within geophysical imaging (e.g., Wagner and Uhlemann 2021), to enhance the interpretability of the obtained results.

Geoelectric imaging techniques represent a valuable tool with regard to a range of critical near-surface applications. These include, but are not limited to, hydrological and hydrogeophysical characterization (e.g., Grünenbaum et al. 2023), assessment of natural risks (e.g., Whiteley et al. 2019), investigation of permafrost degradation (e.g., Wagner et al. 2019; Mudler et al. 2022; Herring et al. 2023), monitoring of contaminated sites (e.g., Caterina et al. 2017) and mineral exploration (e.g., Sasaki and Matsuo 1990; Moreira et al. 2019). As the quantitative demands of applications continue to increase, researchers improve the capabilities of the employed data acquisition techniques, while also enhancing the understanding of the relations that link the macroscopic electrical response of a given rock to its properties at pore scale. A significant advancement that improved the quantitative diagnostic potential of the geoelectric method was the transition from direct current (DC) resistivity measurements, which provide information on the subsurface's ability to conduct electrical current, to induced polarization (IP) measurements, analyzing the capability of the subsurface to develop electrical polarization (e.g., Bleil 1953; Seigel 1959; Van Voorhis et al. 1973; Nabighian and Elliot 1976; Pelton et al. 1978) and focusing primarily on the frequency range below 1 kHz. The additional information on the polarizability can be used to reduce the ambiguities that arise during an interpretation of the isolated resistivity, while also providing a basis for an extensive petrophysical characterization of the subsurface (e.g., Kemna et al. 2004; Weigand and Kemna 2017; Römhild et al. 2024).

Complex resistivity (CR) imaging is a technique to invert tomographic IP data into a model of the subsurface's distributed electrical conduction and polarization properties. The subsurface is parameterized in terms of a complex electrical conductivity distribution, the data are given by complex electrical impedance readings, and the imaging problem is solved in the frequency domain (FD). For a given subsurface model, the forward calculation is performed efficiently by solving the Poisson equation at a single angular frequency, meaning that it can be carried out exclusively for those frequencies that are of interest. This is contrasted by the need to evaluate the convolution of the time-dependent electrical conductivity with the time-dependent electric field during a time-domain (TD) forward calculation (e.g., Hördt et al. 2006), implying a higher computational cost. By imaging the complex electrical conductivity of the subsurface at individual frequencies, a minimal amount of assumptions on the spectral characteristics of the polarization phenomenon is enforced during the inversion. To analyze TD IP measurements using CR imaging, the data must be converted from the TD into the FD, using an appropriate conversion approach. If the conversion approach is not sufficiently accurate, or imposes inappropriate constraints on the spectral characteristics of the medium under investigation, interpretation errors are inevitable.

The deterministic inversion of tomographic CR measurements in complex variables was first developed by Kemna (2000), elegantly using complex algebra to extend the weighted-least square inversion approach for electrical resistivity tomography to the complex domain. Note that the formulation of the inverse problem in complex variables remains true to the underlying physical phenomenon, as described above. During the following years, complex resistivity (CR) imaging has been established for a large number of applications (e.g., Flores Orozco et al. 2011; Martin and Günther 2013; Kemna et al. 2012; Maierhofer et al. 2022). To achieve an accurate uncertainty quantification alongside a more comprehensive analysis and characterization of the CR imaging problem, it is useful to transition from deterministic to probabilistic inversion approaches, an objective that is subject of current research (e.g., Tso et al. 2024; Roudsari et al. 2024). To fully exploit the capabilities of the probabilistic formulation, the corresponding posterior distribution must be characterized appropriately. While the maximum a posteriori (MAP) solution can be found by means of optimization, the accurate estimation of integral estimators that characterize the posterior distribution remains a challenge. In an attempt to meet this challenge, Markov chain Monte Carlo (McMC) methods have been increasingly applied to a variety of geophysical inverse problems, including geoelectric imaging (e.g., De Pasquale et al. 2019; Aleardi et al. 2022). These algorithms have the ability to iteratively simulate a targeted random state, creating a sample that can be used to perform a numerical propagation of the aleatoric (stochastic) uncertainties formalized within the posterior distribution.

## 1.2 Research objectives and document structure

As researchers continue to enhance the quantitative diagnostic potential of the IP method by extending the understanding of the related physical and chemical phenomena at pore scale, it is necessary that the applied geophysical imaging techniques keep pace with the increasing demand for accuracy and uncertainty quantification. The objective of this thesis is to contribute to the solution of the CR imaging problem, by introducing an inversion workflow that emphasizes accurate model inference and uncertainty quantification in a probabilistic framework, allowing for the quantitative use of established relations between IP characteristics and target properties (e.g., hydraulic conductivity, ice content, biomass) in various emerging applications.

This thesis is structured as follows: First, an overview is provided of the theoretical background regarding the probabilistic geophysical inverse problem, the electrical conduction and polarization behavior of geological materials, and the state of the art in CR imaging. The chapters that follow describe in detail the scientific contributions made in this thesis.

- **Chapter 3** introduces a method to convert TD IP transients into FD spectra of complex electrical impedance. It allows for the tomographic inversion of TD IP data into images of complex electrical conductivity at single or multiple frequencies. The method is based on the Debye decomposition of the transients into relaxation-time distributions and is complemented by an appropriate error propagation scheme. A minimal number of assumptions is imposed onto the spectral characteristics of the converted transients, allowing for a general applicability of the conversion method. The conversion of the transients and the subsequent tomographic inversion into images of complex electrical conductivity is demonstrated on a field data set from Kamchatka, Russia.

- **Chapter 4** introduces a probabilistic framework for the solution of geophysical inverse problems in complex variables. The underlying likelihood and prior terms are formulated using complex variables and are set up to account for all associated uncertainties and cross-sensitivities accurately. The resulting posterior distribution represents a probabilistic generalization of the weighted-least squares cost function underlying the established deterministic inversion approach for CR data in complex variables. The MAP solution is estimated deterministically by means of Gauss-Newton optimization. From the MAP solution, uncertainties are approximated locally under the simplifying assumption of normally distributed model parameters and a linearized forward calculation. The theoretical considerations are complemented by a demonstration of the probabilistic framework's capabilities and advantages over the established deterministic inversion approach, with regard to model inference and uncertainty quantification.

- **Chapter 5** introduces the probabilistic geophysical inversion of CR measurements using the Hamiltonian Monte Carlo (HMC) method. Operating on the posterior distribution from Chapter 4, HMC creates an unbiased sample that allows to evaluate integral estimators of interest. The obtained sample is analyzed with regard to the expected complex conductivity image, namely the mean model, and correlations between model parameters. Furthermore, the probabilistic inversion result allows for a global uncertainty quantification by evaluating the posterior covariance matrix over the complete posterior distribution, which is then used to assess the validity of the local uncertainty quantification done in Chapter 4. Although the created sample allows for the evaluation of integral estimators, the algorithm is unable to efficiently maximize the posterior distribution and to create an image that fits the data within the bounds of their uncertainties, while defaulting exactly to the prior assumption in regions of low resolution. The implications of the results are discussed and it is concluded that the probabilistic inversion by means of HMC sampling (Chapter 5) and the deterministic inversion by means of optimization (Chapter 4) complement each other in the context of CR imaging.

The final chapter serves to conclude the work and to provide an outlook into future research perspectives.

# CHAPTER 2

# Theoretical background

## 2.1 Model inference and uncertainty quantification in geophysical inversion

In geophysical inversion, indirect observations in the form of data, subject to uncertainties, are used to infer the state of a physical parameter, which is referred to as the model[1]. Inverse problems play a key role in many different areas of geophysics. They are prominently found in geophysical imaging, where the spatial distribution of a physical parameter in the subsurface is derived from indirect and non-invasive measurements. Although the underlying physical principles vary depending on the specific geophysical method that is used, the mathematical formulation of the inverse problem is often similar across different applications. The geophysical inverse problem can be formalized using a probabilistic formulation that describes data and model as random variables, imposing a well defined structure on their uncertainties through the construction of a conditional posterior distribution for the model, given the data. All aleatoric uncertainties formalized within the posterior distribution are stochastic in nature and are propagated into the solution of the inverse problem. However, it is important to note the existence of epistemic uncertainties, which are generally outside the mathematical formalism used to define the probabilistic inverse problem, and are not accounted for within the formulation. As a consequence, their effect is not propagated into the uncertainty estimate of the inversion result. While the forward problem is governed by the underlying physical principles, being deterministic and unique in its solution, geophysical inverse problems are often mixed-determined or under-determined and are typically characterized by a non-unique solution, as well as by a limited resolution of the inferred model. To constrain geophysical inverse problems, it is therefore common practice to rely heavily on prior assumptions regarding the characteristics of the inferred model, which can be formalized using a prior term. The data space and model space are related by the likelihood term, which assigns a conditional

---

[1] This thesis uses the naming convention in which the term *model* refers to the state which is to be inferred from the measured data. Please note that there are other naming conventions in which the term *model* refers to the forward calculation.

probability to the data, given the model. Based on the likelihood term and prior term, a conditional posterior distribution can be formulated for the model, given the data. Depending on the aspect of the solution that is of practical interest, one might aim to find the model that maximizes the posterior distribution, or evaluate integral estimators such as the mean, correlations, variances, and covariances.

This section offers an overview of the construction of the probabilistic geophysical inverse problem and outlines its solution using optimization and McMC sampling.

### 2.1.1 The probabilistic geophysical inverse problem

The probabilistic geophysical inverse problem can be formalized using Bayes' theorem (Bayes 1763). The posterior distribution

$$p(\mathbf{x}|\mathbf{y}) = \frac{p(\mathbf{y}|\mathbf{x})\,p(\mathbf{x})}{p(\mathbf{y})} \propto p(\mathbf{y}|\mathbf{x})\,p(\mathbf{x}), \tag{2.1}$$

assigns a conditional probability to the state $\mathbf{x} \in \mathbb{R}^M$, given the observations $\mathbf{y} \in \mathbb{R}^N$. It is formulated as the product of the likelihood term and the prior term, divided by the evidence $p(\mathbf{y}) = \text{const.}$

The likelihood term

$$p(\mathbf{y}|\mathbf{x}) \propto \exp\left(-\frac{1}{2}(\mathbf{y} - \mathbf{f}(\mathbf{x}))^T \mathbf{C}_{\mathbf{y}}^{-1} (\mathbf{y} - \mathbf{f}(\mathbf{x}))\right), \tag{2.2}$$

relates the state space and the observation space via the forward operator $\mathbf{f}(\cdot)$, implying normally distributed measurement and modeling errors. Uncertainties are accounted for by the covariance matrix $\mathbf{C}_{\mathbf{y}}$. Given an appropriate forward operator, the observation uncertainties are much larger that the modeling uncertainties, therefore dominating $\mathbf{C}_{\mathbf{y}}$. While theoretically providing the ability to account for covariances between individual observations, $\mathbf{C}_{\mathbf{y}}$ is usually assumed to be a diagonal matrix, implying uncorrelated observation uncertainties.

The prior term introduces independent information on the state into the posterior distribution. Various kinds of probability distributions can be used as priors. The simplest kind of priors are uniform, potentially limited to a given range. A different formulation that relates closely to the regularized least-squares solution of the geophysical inverse problem reads as:

$$p(\mathbf{x}) \propto \exp\left(-\frac{1}{2}(\mathbf{x} - \mathbf{x}_p)^T \mathbf{R}_{\mathbf{x}} (\mathbf{x} - \mathbf{x}_p)\right), \tag{2.3}$$

with the inverse prior covariance matrix $\mathbf{R}_{\mathbf{x}}$ and the prior state $\mathbf{x}_p$. The inverse prior covariance matrix can be modified to enforce different characteristics on the state. If $\mathbf{R}_{\mathbf{x}} \sim \mathbf{I}$, the prior term favors solutions that show minimal deviation from the prior state. In a least-squares sense, this corresponds to the minimum norm solution of the inverse problem. Correlations between parameters can be introduced to enforce structural characteristics. Common choices for such spatial regularization operators are smoothness constraints that minimize differences between neighboring parameters and geostatistical regularization operators, which allow for more detailed control of the spatial characteristics that are favored by the prior term (e.g., Maurer et al. 1998). Figure 2.1 shows three examples for spatial correlations that may be enforced by geostatistical regularization operators. Favoring appropriate structural characteristics can lead to an improved state inference, whereas favoring inappropriate characteristics can significantly reduce the quality of the inferred state (e.g., Jordi et al. 2018). It is therefore crucial that the employed mathematical formalism is sufficiently flexible and allows for the prior information to be adjusted on an individual basis for each inferred parameter.

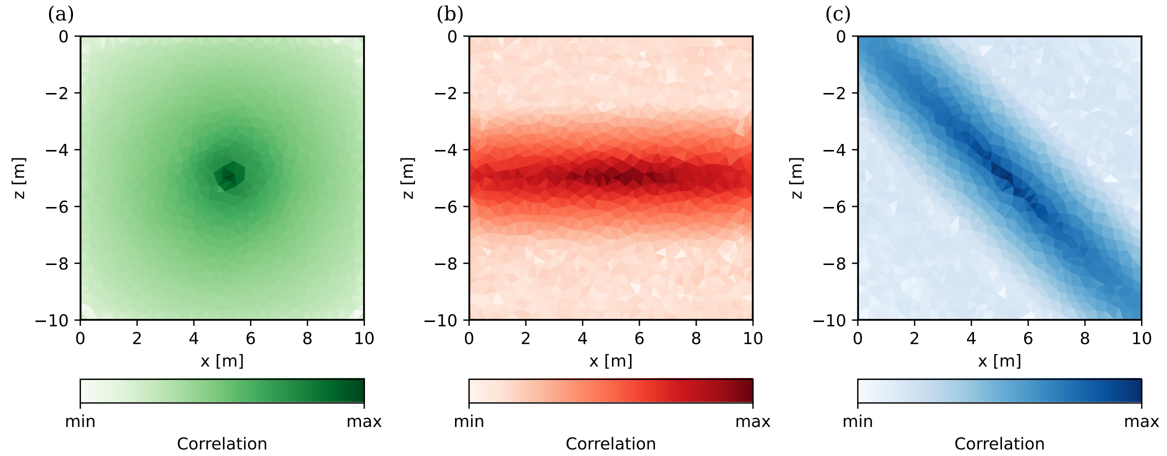

**Figure 2.1:** Correlations between imaged parameters enforced using geostatistical regularization for different cases: **(a)** isotropic; **(b)** anisotropic without dip; **(c)** anisotropic with dip.

### 2.1.2 Extension to complex random variables

To extend the formulation of the probabilistic inverse problem to complex variables, i.e. considering a complex valued state vector and a complex valued observation vector, this thesis follows Picinbono (1996) in the construction of the associated likelihood and prior term, as described in detail in Chapter 4. This section provides an overview on how probability distributions must be set up to accurately characterize complex random vectors.

To describe the second-order statistics of a zero-mean complex random vector $\tilde{\mathbf{x}} = \mathbf{x}' + i\mathbf{x}'' \in \mathbb{C}^M$, with real part $\mathbf{x}'$ and imaginary part $\mathbf{x}''$, consideration of the isolated covariance matrix $\tilde{\mathbf{C}} \triangleq E\left(\tilde{\mathbf{x}}\tilde{\mathbf{x}}^T\right)$ is insufficient and has to be complemented by consideration of the relation matrix $\tilde{\mathbf{\Gamma}} \triangleq E\left(\tilde{\mathbf{x}}\tilde{\mathbf{x}}^H\right)$. Choosing $\tilde{\mathbf{\Gamma}} = \mathbf{0}$ implicitly assumes second-order circularity of the complex random vector, meaning that the second-order statistics of $\tilde{\mathbf{x}}$ and $\tilde{\mathbf{x}} \exp(i\theta)$ are the same for all $\theta$ (Picinbono 1996), which is of course not desirable for our purposes. To proceed from here, the formulation of the complex random vector $\tilde{\mathbf{x}}$ has to be extended, using the conjugate coordinate representation of complex vectors (e.g., Kreutz-Delgado 2009). For the complex vector $\tilde{\mathbf{x}}$ let $\overset{c}{\mathbf{x}} \triangleq \frac{1}{\sqrt{2}}\left(\tilde{\mathbf{x}}, \tilde{\mathbf{x}}^*\right)^T \in \mathbb{C}^{2M}$ be its representation in conjugate coordinates, with $^*$ denoting the complex conjugation and $^T$ denoting the transpose. The representation in conjugate coordinates is related to the representation of $\tilde{\mathbf{x}}$ in terms of its real and imaginary parts $\overset{r}{\mathbf{x}} \triangleq (\mathbf{x}', \mathbf{x}'')^T \in \mathbb{R}^{2M}$ by the linear transformations

$$\overset{c}{\mathbf{x}} = \underbrace{\frac{1}{\sqrt{2}} \begin{bmatrix} \mathbf{I} & i\mathbf{I} \\ \mathbf{I} & -i\mathbf{I} \end{bmatrix}}_{\tilde{\mathbf{S}}} \overset{r}{\mathbf{x}} \tag{2.4}$$

and

$$\overset{r}{\mathbf{x}} = \tilde{\mathbf{S}}^{-1} \overset{c}{\mathbf{x}} = \tilde{\mathbf{S}}^H \overset{c}{\mathbf{x}} . \tag{2.5}$$

The covariance matrix of $\overset{c}{\mathbf{x}}$ evaluates to (Picinbono 1996):

$$\begin{pmatrix} \tilde{\mathbf{C}} & \tilde{\mathbf{\Gamma}} \\ \tilde{\mathbf{\Gamma}}^H & \tilde{\mathbf{C}}^* \end{pmatrix}, \tag{2.6}$$

which is positive definite. Explicitly, $\tilde{\mathbf{C}}$ and $\tilde{\mathbf{\Gamma}}$ can be calculated from the covariance matrices associated with the real and imaginary parts of $\tilde{\mathbf{x}}$ according to:

$$\tilde{\mathbf{C}} = \mathrm{Cov}(\mathbf{x}', \mathbf{x}') + \mathrm{Cov}(\mathbf{x}'', \mathbf{x}'') + i\left(\mathrm{Cov}(\mathbf{x}'', \mathbf{x}') - \mathrm{Cov}(\mathbf{x}', \mathbf{x}'')\right), \tag{2.7a}$$

$$\tilde{\mathbf{\Gamma}} = \mathrm{Cov}(\mathbf{x}', \mathbf{x}') - \mathrm{Cov}(\mathbf{x}'', \mathbf{x}'') + i\left(\mathrm{Cov}(\mathbf{x}'', \mathbf{x}') + \mathrm{Cov}(\mathbf{x}', \mathbf{x}'')\right). \tag{2.7b}$$

If the uncertainties of $\mathbf{x}'$ and $\mathbf{x}''$ are equal and no correlations exist between $\mathbf{x}'$ and $\mathbf{x}''$, the covariance matrix (2.6) can be simplified significantly, as in that case second-order circularity of $\tilde{\mathbf{x}}$ is given. Assuming that $\tilde{\mathbf{x}}$ is normally distributed, Picinbono (1996) formulates the generalized distribution of $\overset{c}{\mathbf{x}}$ as:

$$p(\overset{c}{\mathbf{x}}) \propto \exp\left(-\frac{1}{2}\begin{pmatrix} \tilde{\mathbf{x}}^H & \tilde{\mathbf{x}}^T \end{pmatrix} \begin{pmatrix} \tilde{\mathbf{C}} & \tilde{\mathbf{\Gamma}} \\ \tilde{\mathbf{\Gamma}}^H & \tilde{\mathbf{C}}^* \end{pmatrix}^{-1} \begin{pmatrix} \tilde{\mathbf{x}} \\ \tilde{\mathbf{x}}^* \end{pmatrix}\right). \tag{2.8}$$

In Section 4.2, the concepts above are used to construct a posterior distribution for geophysical inverse problems in complex variables.

### 2.1.3 Optimization approaches

In the context of probabilistic inversion, optimization approaches aim at finding a state that maximizes the posterior distribution. This can be formalized using the minimization problem:

$$\min_{\mathbf{x}} \left(-\ln\, p(\mathbf{x}|\mathbf{y})\right) = \min_{\mathbf{x}} \left(\Psi(\mathbf{x})\right). \tag{2.9}$$

To simplify the notation in the following section, the cost function is given by the negative log-posterior:

$$\Psi(\mathbf{x}) = -\ln p(\mathbf{x}|\mathbf{y}). \tag{2.10}$$

If the forward operator is independent of the state, i.e. $\mathbf{f}(\mathbf{x}) = \mathbf{G}\mathbf{x}$, an analytic solution for problem (2.9) may be obtained alongside an analytic propagation of uncertainties (e.g., Tarantola 2005). If the forward calculation is non-linear, problem (2.9) has to be solved iteratively. Minimization schemes can be derived by developing $\Psi$ into a Taylor series around a given state $\mathbf{x}_q$. Here, we consider terms up to the second degree:

$$\hat{\Psi}(\Delta\mathbf{x}_q) = \Psi(\mathbf{x}_q) + \frac{\partial\,\Psi}{\partial\,\mathbf{x}^T}\Delta\mathbf{x}_q + \frac{1}{2}\Delta\mathbf{x}_q^T\frac{\partial^2\,\Psi}{\partial\,\mathbf{x}\partial\,\mathbf{x}^T}\Delta\mathbf{x}_q. \tag{2.11}$$

The first-order necessary condition

$$\frac{\partial\,\hat{\Psi}}{\partial\,\Delta\mathbf{x}_q} \overset{!}{=} \mathbf{0} \tag{2.12}$$

yields the Gauss-Newton scheme:

$$\frac{\partial^2\,\Psi}{\partial\,\mathbf{x}\partial\,\mathbf{x}^T}\Delta\mathbf{x}_q = -\frac{\partial\,\Psi}{\partial\,\mathbf{x}^T}, \tag{2.13}$$

with the state update $\Delta\mathbf{x}_q$. Neglecting second derivatives of the forward operator during the calculation of the Hessian $\frac{\partial^2\,\Psi}{\partial\,\mathbf{x}\partial\,\mathbf{x}^T}$, the system of normal equations that corresponds to the iterative solution of Equation (2.9) reads:

$$\mathbf{B}_q\,\Delta\mathbf{x}_q = \mathbf{b}_q, \tag{2.14a}$$

$$\mathbf{B}_q = \mathbf{G}_q^T\mathbf{C}_\mathbf{y}^{-1}\mathbf{G}_q + \mathbf{R}_\mathbf{x}, \tag{2.14b}$$

$$\mathbf{b}_q = \mathbf{G}^T\mathbf{C}_\mathbf{y}^{-1}\left(\mathbf{y} - \mathbf{f}(\mathbf{x}_q)\right) - \mathbf{R}_\mathbf{x}\left(\mathbf{x} - \mathbf{x}_p\right), \tag{2.14c}$$

with

$$\mathbf{G}_q = \left(\frac{\partial\,\mathbf{f}}{\partial\,\mathbf{x}}\right)_q \tag{2.15}$$

being the Jacobian matrix and $\Delta\mathbf{x}_q$ the state update. The Gauss-Newton scheme is a deterministic and local optimization method, implying that it is not guaranteed to find the global minimum of the cost function and can be very sensitive to the choice of starting parameters. Nonetheless, it has seen a widespread and successful use in geophysical inversion, including geoelectric imaging, due to its efficiency and adaptability. The use of global optimization methods in geophysical inversion has seen some exciting developments (e.g., Shaw and Srivastava 2007; Datta and Sen 2016; Gao et al. 2022), suggesting that such methods will be increasingly available for applications where the Gauss-Newton scheme fails to provide good results.

The posterior covariance is a global property of the posterior distribution and can be used to describe the uncertainty of the inferred parameters. For a given deterministic inversion result, the posterior covariance matrix can be approximated locally as the inverse Hessian under the assumption of normally distributed parameters and a linearized forward calculation in the vicinity of the inferred state (Tarantola 2005):

$$\mathbf{C}_\mathbf{x} \approx \left(\mathbf{G}^T\mathbf{C}_\mathbf{y}^{-1}\mathbf{G} + \mathbf{R}_\mathbf{x}\right)^{-1}. \tag{2.16}$$

Equation (2.16) estimates the posterior covariance matrix exactly, if the inverse problem is linear. In that case, the posterior distribution is fully characterized by the posterior covariance matrix and the mean state, which is not the case for non-linear inverse problems.

Extending the concepts introduced above to inverse problems that feature complex-valued state vectors $\tilde{\mathbf{x}}$ is non-trivial, as one has to optimize a real function (the cost function) of a complex variable. Generally speaking, for a function $\tilde{h}(x' + ix'') = h'(x', x'') + ih''(x', x'')$ to be complex differentiable, the Cauchy-Riemann equations have to hold:

$$\frac{\partial h'}{\partial x'} = \frac{\partial h''}{\partial x''}, \tag{2.17a}$$

$$\frac{\partial h'}{\partial x''} = -\frac{\partial h''}{\partial x'}. \tag{2.17b}$$

This is not the case for the straight forward adaptation of the cost function (2.9) to complex variables (compare Section 2.3.2), implying that it can not be developed into a converging Taylor series at $\tilde{\mathbf{x}}_q$, using its complex derivative with respect to the complex state. Instead, one has restate the underlying concept of the optimization problem in complex variables and exploit the partial differentiability of the cost function with respect to the real variables $\mathbf{x}'$ and $\mathbf{x}''$.[2] Formulating the complex state vector in terms of conjugate coordinates $\overset{c}{\mathbf{x}}$ allows to achieve this while also retaining the complex-valued notation, due to Equation (2.4), resulting in a mathematical description that reflects the physical phenomenon underlying CR imaging (compare Section 2.2). Note how this neatly connects to the necessity of using conjugate coordinates for the accurate formulation of complex probability distributions (Section 2.1.2). Sorber et al. (2012) derived a Gauss-Newton scheme for the iterative solution of

$$\min_{\overset{c}{\mathbf{x}}} \left( \Psi(\overset{c}{\mathbf{x}}) \right), \tag{2.18}$$

which was adapted for the work presented in this thesis. Their derivation and the adaptation are outlined in Section 4.2.

### 2.1.4 Markov chain Monte Carlo

Two defining characteristics of the probabilistic inverse problem dictate the selection of methods that can be used for its solution. First, the probability of a given state under the posterior distribution can be evaluated. Second, for a non-linear forward operator $\mathbf{f}(\cdot)$, uncorrelated realizations of the random state $\mathbf{x}$ can not be drawn directly from the posterior distribution. To overcome this problem, the random state $\mathbf{x}$ can be simulated iteratively by drawing correlated realizations from a sequence of distributions that converges against the posterior distribution (Gelman and Rubin 1992). McMC methods sample from a target probability distribution $p(\mathbf{x})$, such as the posterior distribution (2.1), by performing a random walk through the state space. The generated sample characterizes the target distribution up to a constant factor (e.g., Mosegaard and Tarantola 1995) and is guaranteed to converge, as its size grows to infinity.

---

[2] In this context, the Wirtinger derivatives $\frac{\partial}{\partial \tilde{x}} = \left(\frac{\partial}{\partial x'} - i\frac{\partial}{\partial x''}\right)$ and $\frac{\partial}{\partial \tilde{x}^*} = \left(\frac{\partial}{\partial x'} + i\frac{\partial}{\partial x''}\right)$ establish a relationship between the partial derivatives with respect to the state's real and imaginary parts, and the partial derivatives with respect to the complex state and its complex conjugate.

During McMC sampling, the iterative simulation of the random state $\mathbf{x}$ is performed as follows (e.g., Bishop 2006; Fichtner et al. 2019): At the beginning, the random walk is initialized at an arbitrary state $\mathbf{x}_0$, which is updated during each iteration. The sample consists of all generated states. The following transition rules between the states of the random walk ensure that the McMC algorithm samples the target distribution. Given a current state $\mathbf{x}_j$, the conditional transition probability to move to the subsequent state $\mathbf{x}_{j+1}$ is independent of all previously generated states:

$$T(\mathbf{x}_{j+1}|\mathbf{x}_0, ..., \mathbf{x}_j) = T(\mathbf{x}_{j+1}|\mathbf{x}_j). \tag{2.19}$$

Each iteration must result in an update of the state, implying that the sum of the conditional transition probabilities $T(\mathbf{x}^{(m)}|\mathbf{x}^{(n)})$ from state $\mathbf{x}^{(n)}$ to any state $\mathbf{x}^{(m)}$ must be 1:

$$\sum_{(m)} T(\mathbf{x}^{(m)}|\mathbf{x}^{(n)}) = 1, \tag{2.20}$$

including the transition $\mathbf{x}^{(m)} \leftarrow \mathbf{x}^{(n)}$ for $n = m$. Note the change in notation with regard to the index. While the lower index $\mathbf{x}_j$ refers to iteration $j$ of the random walk, the upper index $\mathbf{x}^{(n)}$ refers to a specific realization $(n)$ of the random state $\mathbf{x}$, which can be generated repeatedly during the random walk. The product of the conditional transition probability from state $\mathbf{x}^{(n)}$ to state $\mathbf{x}^{(m)}$ and the probability of being at state $\mathbf{x}^{(n)}$ gives the unconditional probability of moving to state $\mathbf{x}^{(m)}$ from any given state:

$$T(\mathbf{x}^{(m)}|\mathbf{x}^{(n)})p(\mathbf{x}^{(n)}). \tag{2.21}$$

If the sum of all unconditional transition probabilities to a state $\mathbf{x}^{(m)}$ is equal to the probability of that state under the target distribution:

$$\sum_{(n)} T(\mathbf{x}^{(m)}|\mathbf{x}^{(n)})p(\mathbf{x}^{(n)}) = p(\mathbf{x}^{(m)}), \tag{2.22}$$

the sample is guaranteed to converge. A sufficient condition to achieve this is fulfilled if the unconditional transition probability from state $\mathbf{x}^{(n)}$ to state $\mathbf{x}^{(m)}$ is equal to the unconditional transition probability from state $\mathbf{x}^{(m)}$ to state $\mathbf{x}^{(n)}$:

$$T(\mathbf{x}^{(m)}|\mathbf{x}^{(n)})p(\mathbf{x}^{(n)}) = T(\mathbf{x}^{(n)}|\mathbf{x}^{(m)})p(\mathbf{x}^{(m)}). \tag{2.23}$$

This sufficient condition is commonly referred to as detailed balance (e.g., Bishop 2006). One of the simplest McMC methods is the Metropolis Hastings (MH) algorithm (Metropolis et al. 1953; Hastings 1970). Given a current state $\mathbf{x}$, a proposed state is drawn from a conditional proposal distribution

$$\mathbf{x}^{+} \leftarrow g(\mathbf{x}^{+}|\mathbf{x}) \tag{2.24}$$

and accepted with the probability:

$$\alpha = \min\left(1, \frac{p(\mathbf{x}^+)\, g(\mathbf{x}|\mathbf{x}^+)}{p(\mathbf{x})\, g(\mathbf{x}^+|\mathbf{x})}\right) \in [0, 1], \tag{2.25}$$

ensuring that Equation (2.23) is fulfilled. The MH algorithm is a basis for many more advanced McMC methods, including Hamiltonian Monte Carlo.

Due to the nature of the iterative simulation, subsequent realizations generated during the random walk are correlated with each other (e.g., Geyer 1992), making the effective size of the generated sample (e.g., Vehtari et al. 2021) smaller than the length of the random walk. Realizations generated early in the random walk can show significant correlation with the arbitrarily chosen state at which the simulation was initialized, making it necessary to classify them as burn-in and exclude them from the analysis of the sample. Given the fact that the simulation can only be performed for a finite number of iterations, it is of high practical importance to assess whether the generated sample has reached approximate convergence and is suited for further analysis. Cowles and Carlin (1996) provide a review of different diagnostics that can be used for this purpose, emphasizing that none of them is infallible. As a recommendation, they suggest that a good convergence assessment should be based on the manual monitoring of different diagnostics, evaluated for multiple random walks performed in parallel. This allows for the visual inspection and comparison of the sampled values between random walks, as well as for the evaluation of non-subjective convergence diagnostics like the potential-scale reduction factor (Gelman and Rubin 1992).

The primary objective of McMC methods is the efficient unbiased approximation of integral estimators, like the mean, which can be evaluated on the basis of the generated sample. In theory, as the length of the random walk approaches infinity, McMC methods will also detect all local and global maxima in the target distribution. In practice, for a random walk of finite length, the curse of dimensionality (Bishop 2006) requires a compromise between exploring regions of high probability and regions that contribute significantly to integrals over the state space. Regions that satisfy this compromise are referred to as the typical set (Betancourt 2017). As efficient McMC methods focus their exploration of the taret distribution on the typical set, they are generally inferior to optimization methods when it comes to estimating local and global maxima, since states maximizing the target distribution only contribute little to integrals over the state space.

The use of McMC methods for geophysical inversion dates back several years (e.g., Sambridge and Mosegaard 2002), with examples being given by Keilis-Borok and Yanovskaja (1967) and Press (1968). The growth in computational resources available to researchers has led to a significant increase in the development and utilization of McMC methods in geophysical inversion. In the following, a non-exhaustive list of exemplary studies is provided. Applications include FD electromagnetic inversions (e.g., Minsley 2011) and joint inversion of electromagnetic and geoelectric measurements (e.g., Peng et al. 2021). The field of seismic imaging has seen applications of McMC methods to seismic traveltime tomography (e.g., Dębski 2010), surface wave tomography (e.g., Zhang et al. 2018) and computational challenging full-waveform tomography (e.g., Zhao and Sen 2021). In the context of geoelectric imaging, Andersen et al. (2003) used a McMC approach to invert ERT measurements into subsurface images that were parameterized in terms of colored polygons to represent individual regions of uniform resistivity, delineated by boundaries whose positions were dynamically adapted during the probabilistic inversion. The ability of McMC methods to accurately characterize uncertainties and detect equivalent solutions was further demonstrated by Ramirez et al. (2005). Recently, De Pasquale et al. (2019) used an McMC approach to invert ERT measurements using a parameterization that explicitly accounts for the geometry of an interface between two inhomogeneous geological structures. Many attempts have been made to improve the applicability of McMC methods to geoelectric imaging problems, utilizing more sophisticated McMC inversion schemes (e.g., Vinciguerra et al. 2020) and accelerating the forward calculation using machine-learning (e.g., Aleardi et al. 2022). Besides geophysical imaging, McMC methods are also used for the inversion of electrical tomography measurements in the context of medical imaging (e.g., Kaipio et al. 2000; West et al. 2004).

### 2.1.5 Hamiltonian Monte Carlo

As discussed above, many McMC methods suffer from a strong autocorrelation between the subsequent states that are generated during the random walk. The random walk moves slowly through the state space and in many cases an unfeasible amount of proposal steps has to be performed in order to reach approximate convergence of the generated sample. An example for this is the MH algorithm. Proposed states that are located in the vicinity of the current state are associated with a high acceptance probability (compare Equation (2.25)) and will be accepted frequently, but the overall exploration of the target distribution will be slow. If the proposed states are further away, i.e. the variance of the proposal distribution is larger, the mean acceptance probability will usually drop significantly, if the proposal distribution is not a very good approximation of the target distribution. This results in more proposals being rejected, also causing a slow exploration of the target distribution and a drop in the algorithm's efficiency.

Hamiltonian Monte Carlo (HMC) is a McMC algorithm that addresses this problem by incorporating gradient information on the negative logarithm of the target distribution into the proposal step. Utilizing the physical analogy of a particle moving through the state space, HMC is able to generate distant proposals with high MH acceptance probabilities, avoiding strong correlations between subsequent states of the random walk and a slow exploration of the target distribution. The particle's position in the state space $\mathbf{x}$ and its momentum $\mathbf{p}$ give its joint state ($\mathbf{x}$, $\mathbf{p}$). The Hamiltonian $H(\mathbf{x}, \mathbf{p})$ represents the total energy of the system, given by the sum of the particle's potential $U(\mathbf{x})$ and kinetic $K(\mathbf{p})$ energy:

$$H(\mathbf{x}, \mathbf{p}) = U(\mathbf{x}) + K(\mathbf{p}). \tag{2.26}$$

Here, the potential energy is defined as the negative logarithm of the target distribution

$$U(\mathbf{x}) = -\ln\left(p(\mathbf{x})\right), \tag{2.27}$$

and can be thought of as the topography the particle moves on. The kinetic energy of the particle

$$K(\mathbf{p}) = \frac{1}{2}\mathbf{p}^T\mathbf{M}^{-1}\mathbf{p} \tag{2.28}$$

is a function of its momentum. While the mass matrix $\mathbf{M}$ has no direct analogy in the context of the geophysical inverse problem, it can be used to enhance the efficiency of the algorithm (Fichtner et al. 2019; 2021). Based on the total energy of the system, the canonical distribution

$$p_c(\mathbf{x},\mathbf{p}) \propto \exp\left(-H(\mathbf{x},\mathbf{p})\right) = p(\mathbf{x})\exp\left(-\frac{1}{2}\mathbf{p}^T\mathbf{M}^{-1}\mathbf{p}\right) \tag{2.29}$$

assigns a probability to any joint state of the particle. HMC samples from distribution (2.29), creating random realizations of the joint state, from which a sample of the target distribution $p(\mathbf{x})$ can be obtained by marginalizing over the momentum values.

The proposal step is initialized by generating a random momentum value:

$$\mathbf{p} \leftarrow p(\mathbf{p}) \propto \exp\left(-\frac{1}{2}\mathbf{p}^T\mathbf{M}^{-1}\mathbf{p}\right). \tag{2.30}$$

The joint state $(\mathbf{x},\mathbf{p})$ is then propagated through fictitious time $t$ by numerically solving Hamilton's equations of motion:

$$\frac{\mathrm{d}\,\mathbf{p}}{\mathrm{d}\,t} = -\frac{\partial\,H}{\partial\,\mathbf{x}}, \tag{2.31a}$$

$$\frac{\mathrm{d}\,\mathbf{x}}{\mathrm{d}\,t} = \frac{\partial\,H}{\partial\,\mathbf{p}}, \tag{2.31b}$$

simulating movement of the particle along trajectories governed by classical mechanics. To achieve this, Equations (2.31) have to be solved numerically, using an appropriate numerical integration scheme. A common choice, which is also used in this thesis, is the Leapfrog scheme (e.g., Neal et al. 2011; Betancourt 2017; Fichtner et al. 2019):

$$\mathbf{p}\left(t+\frac{\varepsilon}{2}\right) = \mathbf{p}(t) - \frac{\varepsilon}{2}\nabla_{\mathbf{x}}U(\mathbf{x}(t)), \tag{2.32a}$$

$$\mathbf{x}(t+\varepsilon) = \mathbf{x}(t) + \varepsilon\,\mathbf{M}^{-1}\mathbf{p}\left(t+\frac{\varepsilon}{2}\right), \tag{2.32b}$$

$$\mathbf{p}(t+\varepsilon) = \mathbf{p}\left(t+\frac{\varepsilon}{2}\right) - \frac{\varepsilon}{2}\nabla_{\mathbf{x}}U(\mathbf{x}(t+\varepsilon)). \tag{2.32c}$$

As Equations (2.32) have to be evaluated for each time step of the numerical simulation, the ability to evaluate the potential energy's gradient $\nabla_{\mathbf{x}}U(\mathbf{x}(t))$ efficiently is crucial for the practical applicability of HMC. After the simulation of the trajectory, the proposed joint state is then subjected to a modified version of the MH acceptance criterion:

$$\alpha = \min\left[1, \frac{p_c(\mathbf{x}^+,\mathbf{p}^+)}{p_c(\mathbf{x},\mathbf{p})}\right] = \min\left[1, e^{-H(\mathbf{x}^+,\mathbf{p}^+)+H(\mathbf{x},\mathbf{p})}\right]. \tag{2.33}$$

It can be seen that (2.33) satisfies detailed balance (2.23):

$$\min\left[1, \frac{p_c(\mathbf{x}^+, \mathbf{p}^+)}{p_c(\mathbf{x}, \mathbf{p})}\right] p_c(\mathbf{x}, \mathbf{p}) = \min\left[1, \frac{p_c(\mathbf{x}, \mathbf{p})}{p_c(\mathbf{x}^+, \mathbf{p}^+)}\right] p_c(\mathbf{x}^+, \mathbf{p}^+). \tag{2.34}$$

HMC features three main hyperparameters which have to be tuned to ensure a good performance of the algorithm. These hyperparameters are the mass matrix $\mathbf{M}$, the step length $\varepsilon$ used for the numerical integration of Hamilton's equations, and the number of time steps for which the trajectory is simulated. The mass matrix can be used to adapt the proposal to the expected variability of the individual parameters. This is very useful, as the variances and covariances of the individual parameters in geophysical inverse problems tend to vary a lot, due to variations in sensitivity and resolution. Furthermore, the mass matrix can be used to stabilize the algorithm if the inferred parameters represent different physical quantities. This is the case for CR imaging, which can be interpreted as an inverse problem where a joint inversion is performed for the complex conductivity's magnitude and phase, using a forward operator that is physically coupled (compare Section 2.2). By adapting the mass matrix to account for the individual variability of the different parameters, the proposal is stabilized without changing the underlying formulation of the posterior distribution. Fichtner et al. (2019; 2021) demonstrated that an appropriate choice, or even automated tuning, of the mass matrix drastically improves the efficiency of HMC in practice.

Depending on the topography of the target distribution's negative logarithm (2.27) in the vicinity of the current state, some trajectory lengths might be more efficient than others. As a consequence, the ideal choice for the length of the simulated trajectory might vary over the course of the random walk. Generally speaking, one wants to maximize the effective distance of the proposal, which is the norm of the difference between the current state and the proposed state, as this minimizes autocorrelation within the random walk. A trajectory length that is too short fails to achieve this goal for obvious reasons. However, also trajectories that are very long might not maximize the effective distance of the proposal, as the simulation can begin to loop back on itself, leading to a decrease in the effective distance. To adaptively tune the trajectory length during each proposal step, Hoffman et al. (2014) introduced the No-U-Turn sampler (NUTS). Their algorithm is based on the construction of the fictitious particle trajectories by repeated doubling of a binary tree, creating a set $\mathcal{C}$ of joint states. Before each doubling of the tree, the direction in which to extend the trajectory is chosen at random. To define an upper limit for efficient trajectory lengths, a break criterion is formulated based on the derivative of the distance between the leftmost $\mathbf{x}^l$ and rightmost $\mathbf{x}^r$ state of the trajectory with respect to fictitious time[3]:

$$\frac{\mathrm{d}}{\mathrm{d}t} \frac{\left(\mathbf{x}^l - \mathbf{x}^r\right)^T \left(\mathbf{x}^l - \mathbf{x}^r\right)}{2} = \left(\mathbf{x}^l - \mathbf{x}^r\right)^T \frac{\mathrm{d}}{\mathrm{d}t}\left(\mathbf{x}^l - \mathbf{x}^r\right) = \left(\mathbf{x}^l - \mathbf{x}^r\right)^T \left(\mathbf{M}^{-1}\mathbf{p}^l\right). \tag{2.35}$$

If the distance between the leftmost and rightmost state of the trajectory decreases, Equation (2.35) becomes negative, indicating that a further extension of the trajectory would decrease

---

[3] Note that the mass matrix $\mathbf{M}$ is not included explicitly in the original publication.

efficiency. Consequently, the break criterion is defined as:

$$\left[\left(\mathbf{x}^l - \mathbf{x}^r\right)^T \left(\mathbf{M}^{-1}\mathbf{p}^r\right) < 0\right] \vee \left[\left(\mathbf{x}^l - \mathbf{x}^r\right)^T \left(\mathbf{M}^{-1}\mathbf{p}^l\right) < 0\right]. \tag{2.36}$$

Hoffman et al. (2014) describe different versions of the NUTS. In the most basic version, the updated state is sampled uniformly from the created trajectory, after the set $\mathcal{C}$ was modified in a slice sampling step. However, this is can be inefficient, as it does not favor large effective distances of the state update and only prevents trajectories from becoming too long. Furthermore, it requires that all generated joint states are stored. Hoffman et al. (2014) also introduce a more sophisticated version of the NUTS that divides the set $\mathcal{C}$ into two subsets. The subset $\mathcal{C}_{new}$ contains the joint states added during the final doubling, while the subset $\mathcal{C}_{old}$ contains all other joint states, including the initial joint state from which the trajectory was created. The transition kernel

$$T\left((\mathbf{x},\mathbf{p})^+ \middle| (\mathbf{x},\mathbf{p}), \mathcal{C}\right) = \begin{cases} \frac{\mathbb{I}[(\mathbf{x},\mathbf{p})^+ \in \mathcal{C}_{new}]}{|\mathcal{C}_{new}|} & \text{if } |\mathcal{C}_{new}| > |\mathcal{C}_{old}| \\ \frac{|\mathcal{C}_{new}|}{|\mathcal{C}_{old}|} \frac{\mathbb{I}[(\mathbf{x},\mathbf{p})^+ \in \mathcal{C}_{new}]}{|\mathcal{C}_{new}|} + \left(1 - \frac{|\mathcal{C}_{new}|}{|\mathcal{C}_{old}|}\right) \mathbb{I}[(\mathbf{x},\mathbf{p})^+ = (\mathbf{x},\mathbf{p})] & \text{if } |\mathcal{C}_{new}| \leq |\mathcal{C}_{old}| \end{cases} \tag{2.37}$$

proposes a move from $\mathcal{C}_{old}$ to a random state in $\mathcal{C}_{new}$ and accepts it with the probability $\frac{|\mathcal{C}_{new}|}{|\mathcal{C}_{old}|}$, while satisfying detailed balance (2.23). Algorithm 3 in the original paper (Hoffman et al. 2014), which was used for the probabilistic inversion in Chapter 5, applies the transition kernel (2.37) after each doubling of the tree, which does not break detailed balance and maximizes the effective distance of the model update.

While a constant step length can be used for the numerical integration of Equations (2.31) over time, it is often better to dynamically adjust it in order to reach a desired average acceptance probability $\bar{\alpha}$. For HMC, an optimal value for $\bar{\alpha}$ is 0.65, as described by Neal et al. (2011). Usually, the step length is tuned during the burn-in phase, which is excluded from the further analysis of the sample. Many approaches can be used to tune the step length. While Hoffman et al. (2014) pair the NUTS with a dual averaging scheme, a vanishing adaption scheme described by Andrieu and Thoms (2008) is used in this thesis, which yields good results as demonstrated in Chapter 5.

HMC was first applied to probabilistic geophysical inverse problems by Muir and Tkalčić (2015; 2020) and Sen and Biswas (2017). Fichtner et al. (2019) introduced the solution of geophysical imaging problems by HMC, applying it to linear and non-linear traveltime tomography, as well as reflection seismology. Since then, HMC has been used for efficient null-space exploration and uncertainty quantification (Fichtner and Zunino 2019; Fichtner et al. 2021) in geophysical imaging. Gebraad et al. (2020), de Lima et al. (2023) and Dhabaria and Singh (2024) applied HMC to the seismic full-waveform inverse problem, pushing the feasibility with regard to computationally expensive applications. Outside of a seismic or seismological context, HMC has been applied to joint inverse problems, with Zunino et al. (2022) inverting gravity and magnetic data into subsurface models parameterized in terms of the geometry and properties of polygonal bodies. A 1D joint inversion of long offset TD electromagnetic data and magnetotelluric data was conducted by Carter et al. (2021).

## 2.2 Electrical conduction and polarization behavior of rocks and soils

This section provides an overview of the methods by which researchers describe the electrical conduction and polarization behavior of geological media macroscopically and which phenomena shape the electrical properties at pore scale. While the macroscopic description using Maxwell's equations builds the basis for CR imaging, understanding the phenomena at pore scale is essential for interpreting the results with regard to target parameters and processes.

### 2.2.1 Macroscopic description

On a macroscopic level, Maxwell's equations can be used to describe the electrical conduction and polarization behavior of geological media. Coulomb's law relates the total electric current density to the magnetic field $\tilde{\mathbf{H}}$ [Am$^{-1}$]:

$$\nabla \times \tilde{\mathbf{H}} = \tilde{\mathbf{J}}_c + \frac{\partial \tilde{\mathbf{D}}}{\partial t} + \tilde{\mathbf{J}}_s, \tag{2.38}$$

given conduction currents $\tilde{\mathbf{J}}_c$, displacement currents $\partial_t \tilde{\mathbf{D}}$ and source currents $\tilde{\mathbf{J}}_s$. The electric field $\tilde{\mathbf{E}}$ [Vm$^{-1}$] originates in electric charges $\nabla \cdot \tilde{\mathbf{E}} = \varrho/(\epsilon_0 \tilde{\epsilon}_r)$, with the charge density $\varrho$ [Cm$^{-3}$], and is related to the displacement flux

$$\tilde{\mathbf{D}} = \epsilon_0 \tilde{\epsilon}_r \tilde{\mathbf{E}} \tag{2.39}$$

by the product of the relative permittivity $\tilde{\epsilon}_r$ and the permittivity of the vacuum $\epsilon_0$ [Fm$^{-1}$]. Here, $\tilde{\epsilon}_r$ represents the bulk relative permittivity associated with the geological medium at a macroscopic scale, accounting for all occurring polarization processes. Please note that some authors (e.g., Bücker 2019) subdivide the bulk relative permittivity into its contributions, explicitly accounting for the polarization processes characteristic to geological media with an individual polarization term, a notation which is not used in this thesis. The conduction of electric current through a medium is determined by the electrical conductivity $\sigma$ [Sm$^{-1}$]. Ohm's law

$$\tilde{\mathbf{J}}_c = \sigma \tilde{\mathbf{E}} \tag{2.40}$$

relates the conduction currents $\tilde{\mathbf{J}}_c$ to the electric field. Using Equations (2.39) and (2.40), Equation (2.38) becomes:

$$\nabla \times \tilde{\mathbf{H}} = \sigma \tilde{\mathbf{E}} + \epsilon_0 \tilde{\epsilon}_r \frac{\partial \tilde{\mathbf{E}}}{\partial t} + \tilde{\mathbf{J}}_s. \tag{2.41}$$

Given a harmonic electric field of the form $\tilde{E} = |E| \exp(i\omega t)$, a complex electrical conductivity can be derived that accounts for conduction and displacement processes. Inserting the formulation of the harmonic electric field into Equation (2.41) yields:

$$\nabla \times \tilde{\mathbf{H}} = \tilde{\sigma}(\omega) \tilde{\mathbf{E}} + \tilde{\mathbf{J}}_s, \tag{2.42}$$

with the complex electrical conductivity $\tilde{\sigma}(\omega) = \sigma + i\omega\epsilon_0\tilde{\epsilon}_r(\omega) = \sigma'(\omega) + i\sigma''(\omega)$ representing the macroscopic material property that we want to infer during CR imaging. While this thesis assumes an isotropic complex electrical conductivity, anisotropic conduction and polarization characteristics can be accounted for by formulating the complex electrical conductivity as a tensor (e.g., Kenkel et al. 2012). The complex electrical resistivity is given by $\tilde{\rho} = \tilde{\sigma}^{-1}$ [$\Omega$m]. Neglecting electromagnetic induction effects $\nabla \times \tilde{\mathbf{E}} = -\partial_t\tilde{\mathbf{B}} = 0$, the electric field is rotation free and can therefore be expressed by the negative gradient of the electric potential[4]:

$$\tilde{\mathbf{E}} = -\nabla\tilde{\psi}. \tag{2.43}$$

Evaluating the divergence of Equation (2.42) and replacing the electric field according to Equation (2.43) yields the Poisson equation:

$$\nabla \cdot \Big(\tilde{\sigma}(\omega)\nabla\tilde{\psi}(\omega)\Big) - \nabla \cdot \tilde{\mathbf{J}}_s = 0, \tag{2.44}$$

which is the basis for modeling of the complex electric potential $\tilde{\psi}$ [V] and thereby the geoelectric forward calculation. While forward modeling in the FD can be performed accurately by solving Equation (2.44) at individual frequencies, forward modeling in the TD is generally more challenging, as it involves evaluating a convolution of the time dependent conductivities with the electric field (e.g., Hördt et al. 2006).

### 2.2.2 Conduction and polarization mechanisms

Many geological media can be described as porous structures forming a matrix, which is permeated by a network of pores. Generally, the electrical conductivity of the matrix is negligible compared to the electrical conductivity of the pore fluid. In a first approximation, the bulk electrical conductivity $\sigma_b$ is therefore a function of the pore-space geometry and the electrical conductivity of the pore fluid $\sigma_w$. Archie's law (Archie 1942)

$$\sigma = \sigma_w \Phi^m S_w^n \tag{2.45}$$

formalizes this relation based on the porosity $\Phi \in [0,1]$ of the geological medium and the water saturation $S_w \in [0,1]$. The linear relation between the bulk conductivity and the pore-fluid conductivity suggested by Equation (2.45) does no longer hold if the current is not solely conducted through the pore fluid. This can be caused by a significant contribution of the electrical surface conductivity, e.g., if the electrical conductivity of the pore-fluid is low, which causes current to travel within the interface layer between a charged mineral grain (e.g., Clay) and the pore-fluid. Usually, the contributions of pore-fluid conductivity and surface conductivity are assumed to add in parallel (Waxman and Smits 1968; Binley and Slater 2020):

$$\sigma = \sigma_w \Phi^m S_w^n + \sigma_s, \tag{2.46}$$

---

[4] The assumption of $\partial_t\tilde{\mathbf{B}} = 0$ is strictly speaking not consistent with the assumption of a time-dependent harmonic electric field $\tilde{\mathbf{E}}(t)$. Still, it is implemented in CR modeling codes, as it simplifies the forward calculation on a technical level. While not being within the scope of this thesis, research should be conducted to better understand the effect of this simplification, especially when modeling of the complex electric potential is performed at high frequencies.

which is generally reasonable, but can be challenged on the basis of the implied simplifying assumptions with regard to pore-space geometry. Geological media characterized by a very low porosity, like highly consolidated sediments or crystalline rocks, usually exhibit a very high electrical resistivity, if they are not comprised of a significant amount of interconnected electron conducting minerals.

Different mechanisms underlay the ability of rocks and soils to develop electrical polarization. In the frequency range targeted by IP measurements, diffusion-controlled polarization mechanisms associated with the electrical double layer (EDL) dominate the polarization characteristic of the bulk medium. Generally, they are attributed to ions being unable to move freely through the pore space of the porous medium. In a pore space that is saturated with an aqueous solution, positively charged ions that are strongly attracted by the negative charges at the surface of the grain form the Stern layer. As the grain surface and the Stern layer are not at electro-neutrality, a diffuse layer forms around the Stern layer, characterized by an over-representation of positive ions. Because they are only loosely bound to the grain, these ions can be sheared off easily.

Three major polarization mechanisms originate from the electrical double layer. First, the tangential displacement of counterions in the Stern layer is commonly referred to as Stern layer polarization, whereas, second, the displacement of counterions in the diffuse layer gives rise to Diffuse layer polarization. The third mechanism, Membrane polarization, is caused by a blockage of ions in the diffuse layer and in the aqueous solution at narrow sites within the pore space, causing a local excess or deficiency of charges (Binley and Slater 2020). As the area occupied by the electrical double layer correlates with the inner surface area of the medium, it can be seen that the polarizability of the geological medium correlates with the inner surface area as well (e.g., Börner and Schon 1991; Weller et al. 2015). Furthermore, the dominant time constants associated with the electrical double layer polarization are correlated with the characteristic length scales of the porous medium (e.g., Revil et al. 2012). These relations allow for the estimation of target parameters like the hydraulic conductivity, by providing critical information needed to constrain the pore space geometry, enabling an enhanced hydrogeophysical characterization at field scale (e.g., Börner et al. 1996; Kemna et al. 2004; Römhild et al. 2024).

Independent of the electrical double layer, electrode polarization is caused by electrically conductive minerals that are part of or embedded in a rock or soil. Consideration of the chargeability and the dominant relaxation time can provide information on the volume fraction of the ore within the pore space, as well as the dominant grain size of the ore minerals. Qualitatively, this information may be used to localize deposits, while also providing quantitative insight into their expected yield (e.g., Revil et al. 2022).

Discontinuities between different phases in the porous medium give rise to dielectric Maxwell-Wagner polarization. It is observed from 100 Hz to 100 MHz, and is usually not targeted by geoelectric IP measurements.

### 2.2.3 Phenomenological description of polarization characteristics

Different phenomenological models can be used to describe the polarization behavior observed in rocks and soils, capturing characteristics like the chargeability and dominant time constants. Many of these models are associated with an equivalent electrical circuit. In empirical models, researchers relate the characteristics described by the phenomenological models to rock and soil parameters of interest (e.g., Tong et al. 2006a; Revil et al. 2012).

Depending on the quantitative demands of the application at hand, it can be valid to assume a frequency independent conductivity phase. This characteristic is supported by the constant phase angle model, used in early works by Van Voorhis et al. (1973), whose FD formulation reads as:

$$\tilde{\sigma}(\omega) = \sigma_n (i\omega)^{1-q}, \tag{2.47}$$

with the frequency independent conductivity phase:

$$\phi = \frac{\pi}{2}(1-q). \tag{2.48}$$

In the TD, transients measured over geological media that are characterized by a CPA type polarization behavior follow an inverse power law.

The single term Debye model (e.g., Debye 1929; Limbrock and Kemna 2024)

$$\tilde{\sigma}(\omega) = \sigma_\infty + \frac{\sigma_0 - \sigma_\infty}{1 + i\omega\tau_\sigma} \tag{2.49}$$

introduces a frequency dependence into the conductivity magnitude and phase. It has the spectral characteristics of a circuit in which a resistor is connected in parallel with a series connection of a resistor and a capacitor. Here, $\tau_\sigma$ is a characteristic time constant associated with the polarization process. Formulations of the Debye model exist for the complex permittivity, the complex conductivity and the complex resistivity, as summarized recently by Limbrock and Kemna (2024), who also describe the relations between the different formulations explicitly. Transients measured over geological media that exhibit a Debye type polarization behavior take the form of exponential decays. The superposition of Debye models can be used to represent arbitrary polarization characteristics (e.g., Nordsiek and Weller 2008):

$$\tilde{\sigma}(\omega) = \sigma_\infty + (\sigma_0 - \sigma_\infty) \int_0^\infty \frac{g(\tau_\sigma)}{1 + i\omega\tau_\sigma} \, \mathrm{d}\tau_\sigma. \tag{2.50}$$

Here, $g(\tau_\sigma)$ is a distribution of time constants, representing the contribution of the term at a given value of $\tau_\sigma$ to the total chargeability and integrating to 1. The decomposition of measured transients and spectra into discrete relaxation-time distributions is referred to as the Debye decomposition. It is an effective technique for the analysis of IP measurements (e.g., Tarasov and Titov 2007; Weigand and Kemna 2016). While being generally applicable, the multi-term Debye model requires a large amount of parameters to fit a temporally distributed polarization characteristic. The less parameterized Cole-Cole model (Cole and Cole 1941;

Pelton et al. 1978; Weigand et al. 2017)

$$\tilde{\sigma}(\omega) = \sigma_\infty + \frac{\sigma_0 - \sigma_\infty}{1 + (i\omega\tau_{\sigma,cc})^c} \tag{2.51}$$

can be interpreted as a modification of the Debye model, introducing the Cole-Cole exponent $c \in [0, 1]$. For $0 < c < 1$, the Cole-Cole model formalizes a temporally distributed polarization characteristic around the dominant time constant $\tau_{\sigma,cc}$, using only one more parameter than the Debye model.

## 2.3 Complex resistivity imaging

### 2.3.1 Measurements and error models

IP measurements can be carried out in the TD and in the FD. During TD measurements, the current waveform displayed in Figure 2.2a is injected into the ground and measurements are performed using the four point method. The half-cycle injection features an off-time before the polarity of the current injection is reversed, whereas a full-cycle injection (not displayed) does not use an off-time and reverses the polarity of the current injection instantaneously. Following the termination of the current injection at $t = 0$ during a half-cycle injection, the transient voltage decay $V(t)$ between the potential electrodes is measured. After an abrupt decrease of the voltage from its primary value $V_0$ to its secondary value $V_1$, the voltage decays continuously to the limit:

$$\lim_{t \to \infty} V(t) = 0. \tag{2.52}$$

The primary voltage $V_0$ is associated with the direct current (DC) resistivity measurement, whereas the ratio of the initial voltage drop $\frac{V_1}{V_0}$ is called the chargeability (Seigel 1959). If the subsurface is not able to build up electrical polarization, the chargeability takes a value of $\frac{V_1}{V_0} = 0$. The voltage transient is either discretized at specific time steps, or averaged over finite time gates for a better signal to noise ratio. As it is technically not possible to measure the instantaneous voltage drop at $t = 0$, TD IP measurements are often analyzed in terms of the total chargeability $M_{tot}$. This total chargeability corresponds to the area under the normalized voltage transient and can be approximated by summing up the areas of the time gates (e.g., Flores Orozco et al. 2018b). Additionally, TD IP instruments improve the signal to noise ratio by performing stacks, during which the current injection is repeated multiple times and the measurements of the resulting voltage transients are averaged. During an injection cycle that features multiple stacks, the measured voltage transient at a given point in time is a superposition of the voltage transient induced by the most recent current injection, as well as all previously induced voltage transients. The effect can be accounted for analytically (compare Equations (3.15) and (3.16)). An inversion of TD IP measurements by means of CR imaging requires for the acquired data to be converted into the FD. Assuming a frequency independent phase angle in accordance with the phenomenological model given in Equation (2.47), many studies (e.g., Kemna et al. 1997; Kemna 2000; Flores Orozco et al. 2018b; Binley et al. 2016) approximate the phase angle of the complex electrical impedance $\tilde{Z}$ under the assumption that it scales linearly with the measured total chargeability. However, this conversion approach potentially disregards valuable spectral information in the TD data. In Chapter 3, an alternative approach is presented for the extraction of spectral information from TD IP transients, which imposes a minimal amount of constraints on the spectral characteristics of the measurement.

In the FD, measurements are performed by injecting a harmonic sinusoidal current of a given frequency into the subsurface and measuring the magnitude and phase shift of the corresponding electrical impedance (e.g., Zimmermann et al. 2008), as displayed in Figure 2.2b. Spectral information can be obtained by performing the measurement at multiple frequencies, with FD IP methods usually focusing on frequencies below 1 kHz. Measurements conducted in the FD typically yield a more precise spectral resolution of the IP characteristic and can access higher frequencies. However, they remain challenging to execute in field settings, compared to measurements in the TD, which are typically more robust and can, depending on the application, provide sufficient information.

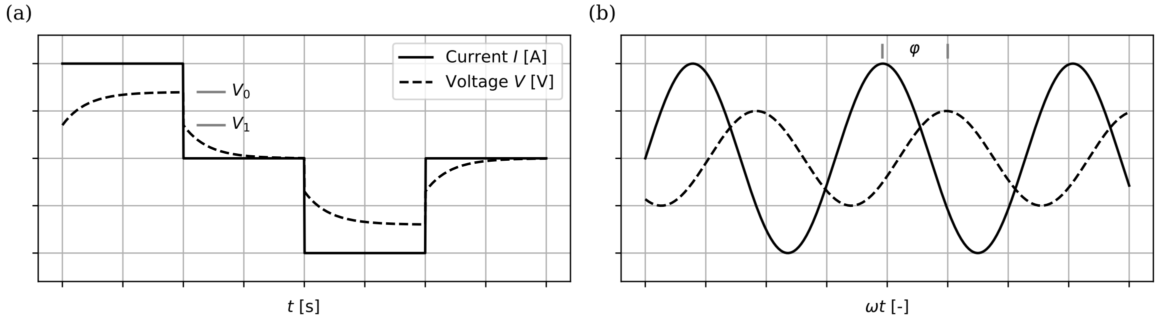

**Figure 2.2:** **(a)** Half-cycle current injection during a time-domain measurement. **(b)** Injection of a sine-wave signal during a frequency domain measurement

During tomographic TD IP and FD IP surveys, measurements are performed using four-point electrode configurations. While this thesis focuses on the field application, tomographic IP measurements can also be carried out in laboratory settings (e.g., Weigand and Kemna 2017). The measured complex electrical impedance $\tilde{Z}$ is given by the ratio of the measured potential difference to the injected current. Let the positions of the current electrodes be $\mathbf{r}_A$ and $\mathbf{r}_B$ and let the positions of the potential electrodes be $\mathbf{r}_P$ and $\mathbf{r}_Q$, then the geometric factor

$$k = 2\pi \left[ \left( \frac{1}{|\mathbf{r}_P - \mathbf{r}_A|} - \frac{1}{|\mathbf{r}_P - \mathbf{r}_B|} \right) - \left( \frac{1}{|\mathbf{r}_Q - \mathbf{r}_A|} - \frac{1}{|\mathbf{r}_Q - \mathbf{r}_B|} \right) \right]^{-1} \tag{2.53}$$

relates the complex electrical impedance $\tilde{Z}$ to the apparent complex conductivity:

$$\tilde{\sigma}_a = \frac{1}{k\tilde{Z}}. \tag{2.54}$$

The probabilistic formulation of the geophysical inverse problem recognizes the data to be subject to stochastic errors by formalizing them as random variables and including their respective uncertainties into the formulation of the likelihood (2.2). Consequently, the choice of error estimates in the data space has a direct influence on the inferred subsurface image and the propagated uncertainty of the inversion result. Systematic data errors can generally not be handled adequately within the mathematical formalism of the probabilistic inverse problem. The stochastic data errors accounted for during the inversion are often challenging to quantify during field surveys, due to the limited possibility of measurement repetition. To obtain robust and consistent data error estimates, error models are widely used to define the underlying characteristic of the data error for the inversion. Here, the uncertainty of a specific data point is defined by the error model, rather than by an individual measure of uncertainty. For the impedance magnitude, the most commonly used error model is linear in $|\tilde{Z}|$:

$$\mathrm{std}\,(|\tilde{Z}|) = a|\tilde{Z}| + b, \tag{2.55}$$

motivated by the linear trend observed for deviations between normal and reciprocal geoelectric data sets (e.g., LaBrecque et al. 1996; Tso et al. 2017).

Based on consistently observed discrepancies between normal and reciprocal complex impedance readings obtained during FD IP measurements at varying frequencies, Flores Orozco et al. (2012b) suggest that the error of the phase measurement is a function of the impedance magnitude and follows an inverse power law:

$$\mathrm{std}(\varphi) = a|\tilde{Z}|^{-c}. \tag{2.56}$$

In their study, they do not report a significant relative dependence of the phase error on the value of the phase measurement itself. Following the reasoning of a constant phase angle model, the approximate proportionality of the total chargeability and the phase angle suggests using a power law as an error model for the total chargeability (Flores Orozco et al. 2018b):

$$\mathrm{std}(M_{tot}) = a|\tilde{Z}|^{-c}, \tag{2.57}$$

considering Equation (2.56).

In practice, the parameters of the error models are determined on the basis of reciprocal measurements performed for the individual survey, or on the basis of additional information, such as instrument specifications and more. With regard to electrical resistivity tomography measurements, Tso et al. (2017) present an overview of the error models and approaches utilized for data uncertainty characterization in a multitude of studies.

### 2.3.2 Inversion approaches

Tomographic IP measurements can be inverted into subsurface models of varying parameterization in the TD and in the FD. The simplest approach for inverting TD IP data follows the concepts introduced by Seigel (1959). The apparent chargeability measured over a subsurface discretized using a mesh of $M$ cells is expressed as (Seigel 1959; Binley and Slater 2020):

$$M_a = \sum_j \hat{m}_j \frac{\partial \log_{10} \rho_a}{\partial \log_{10} \rho_j}, \tag{2.58}$$

based on the intrinsic chargeabilities $\hat{m}_j$ of the different cells. After solving the resistivity imaging problem, the intrinsic chargeabilities are estimated in a one-step linearized inversion, which is possible since the forward operator associated with Equation (2.58) is independent of the intrinsic chargeabilities themselves. This approach and variations of it have been used in multiple studies (e.g., Oldenburg and Li 1994; Sogade et al. 2006).

Assuming the complex electrical conductivity of the subsurface follows a specific polarization characteristic, IP data from TD and FD can be inverted into spatial parameter distributions of predefined phenomenological models, such as the Cole-Cole model (2.51) (e.g., Fiandaca et al. 2012). This allows for easy interpretability of the results and is very sensible if parameters associated with the employed phenomenological model are coupled to target properties of interest, as demonstrated by multiple examples (e.g., Mudler et al. 2022; Römhild et al. 2024). However, as many laboratory experiments have shown, rocks and soils often exhibit polarization characteristics which can not be described by a single Cole-Cole model. Consequently, the narrow parameterization employed by these imaging approaches limits their capacity to represent arbitrary spectral characteristics, rendering them unsuitable for general applications.

Kemna (2000) introduced the deterministic inversion of complex electrical impedances into images of complex electrical conductivity at individual frequencies. As the complex conductivity distribution at each frequency is imaged independently, the approach relies on a minimal amount of prior assumptions with regard to the spectral characteristic of the subsurface. A logarithmic transformation of the complex impedances is used as the data

$$\tilde{d}_i = -\ln|k_i \tilde{Z}_i| + i\varphi_i \tag{2.59}$$

and the model is parameterized as the complex logarithm of the complex electrical conductivity:

$$\tilde{m}_k = \ln|\tilde{\sigma}|_k + i\phi_k. \tag{2.60}$$

The inversion is based on the minimization of the cost function:

$$\Psi(\tilde{\mathbf{m}}) = \frac{1}{2}\left(\tilde{\mathbf{d}} - \tilde{\mathbf{f}}(\tilde{\mathbf{m}})\right)^H \mathbf{C}_{\mathbf{d}}^{-1}\left(\tilde{\mathbf{d}} - \tilde{\mathbf{f}}(\tilde{\mathbf{m}})\right) + \frac{1}{2}\lambda\left(\tilde{\mathbf{m}} - \tilde{\mathbf{m}}_p\right)^H \mathbf{R}_{\mathbf{m}}\left(\tilde{\mathbf{m}} - \tilde{\mathbf{m}}_p\right), \tag{2.61}$$

which represents a straight forward adaptation of the cost function for geophysical inverse problems in real variables to the complex domain (compare Section 2.1.3). The real-valued data covariance matrix holds the squared magnitudes of the complex data error on the main diagonal:

$$\mathbf{C}_{\mathbf{d}} = \left(\tilde{\mathbf{W}}_{\mathbf{d}}^H \tilde{\mathbf{W}}_{\mathbf{d}}\right)^{-1} = \operatorname{diag}\left(|\tilde{e}_1|^2, ..., |\tilde{e}_i|^2, ..., |\tilde{e}_N|^2\right), \tag{2.62}$$

with $\tilde{e}_i = -\operatorname{std}(\ln|Z_i|) - i\operatorname{std}(\varphi_i)$. Reformulation of the data misfit term in Equation (2.61) shows that the real and imaginary parts of the complex residuum are both normalized with respect to the magnitude of the respective complex data error:

$$\Psi_{\mathbf{d}} = \left|\left|\,|\tilde{\mathbf{W}}_{\mathbf{d}}|\Re\left(\tilde{\mathbf{d}} - \tilde{\mathbf{f}}(\tilde{\mathbf{m}})\right)\right|\right|^2 + \left|\left|\,|\tilde{\mathbf{W}}_{\mathbf{d}}|\Im\left(\tilde{\mathbf{d}} - \tilde{\mathbf{f}}(\tilde{\mathbf{m}})\right)\right|\right|^2, \tag{2.63}$$

implying an error ellipse during the inversion that is not equal to the actual error ellipse of

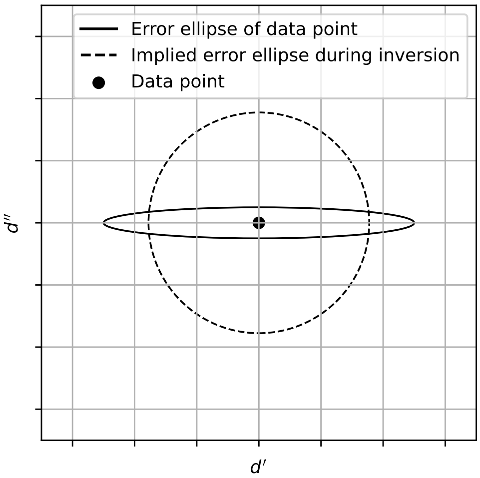

**Figure 2.3:** Data point with error ellipse, given uncorrelated and unequal standard deviations of real and imaginary part, compared to the error ellipse that is implied during the minimization of Equation (2.61).

the data point, if the real and imaginary parts of the data have different standard deviations. This inconsistency is illustrated in Figure 2.3. The same problem arises for the regularization term, where the characteristic and strength of the applied regularization can not be adjusted individually for the real and imaginary part of the model.

As a consequence, minimizing Equation (2.61) can fail to fit the real and imaginary parts of the complex data within their uncertainties, i.e. yield individual root-mean square errors close to 1. This is demonstrated in Section 4.3. Kemna (2000) solves this issue by using a two step approach, during which the conductivity phase image is refined after a solution for the conductivity magnitude has been found. During this final phase improvement, cross-sensitivities are disregarded, since the inversion for the phase image is decoupled from the magnitude image. Applications of the deterministic inversion approach introduced by Kemna (2000) are widespread (e.g., Hördt et al. 2007; Flores Orozco et al. 2012a; 2018a; Weigand and Kemna 2019). Other deterministic approaches for the inversion of CR data include a two step real-valued inversion described in Martin and Günther (2013) and an alternating approach for updating the real and imaginary parts of the complex model introduced by Johnson and Thomle (2018). Recently Wang et al. (2023) compared these approaches and formulated a deterministic least-square inversion scheme that accounts for cross-sensitivities and individual data errors while operating in real variables. Tso et al. (2024) introduced a probabilistic ensemble Kalman inversion scheme, providing an improved uncertainty quantification, while neglecting cross-sensitivities due to the sequentiality of their approach.

In Chapter 4, the CR imaging problem is restated and solved using a probabilistic formulation in complex variables. The introduced probabilistic framework represents a generalization of the inversion approach described by Kemna (2000) and accurately accounts for complex data errors and cross-sensitivities, while simultaneously allowing for the application of independent regularization to the real and imaginary parts of the complex model, thereby improving model inference and uncertainty quantification. Furthermore, it provides theoretical insight into the positioning of the established deterministic inversion approach by Kemna (2000) in a probabilistic context.

# CHAPTER 3

## Conversion of Induced polarization measurements from time domain to frequency domain using Debye decomposition

## Abstract

The time-domain (TD) induced polarization (IP) method is used as an extension of direct current (DC) resistivity measurements to capture information on the ability of the subsurface to develop electrical polarization. In the TD, the transient voltage decay is measured as a function of time after the termination of the current injection. To invert tomographic TD IP data sets into frequency-domain (FD) models of complex electrical resistivity, a suitable approach for converting TD IP transients and their corresponding uncertainties into the FD is essential. To apply existing FD inversion algorithms to TD IP measurements, a conversion scheme must transform the measured decay curves into FD impedances and also propagate the corresponding measurement uncertainties from the TD to the FD. Here, we present such an approach based on a Debye decomposition (DD) of the decay curve into a relaxation-time distribution and the calculation of the equivalent spectrum. The corresponding FD data error can be obtained by applying error propagation through all of these steps. To accomplish the DD we implement a non-linear Gauss-Newton inversion scheme. We test the conversion scheme in a synthetic study and demonstrate its application to field data on a tomographic TD IP data set measured on the Maletoyvaemskoie ore field (Kamchatka, Russia). The proposed conversion scheme yields accurate impedance data for relaxation processes, which are resolved by the TD measurements. The error propagation scheme provides a reasonable FD uncertainty estimate, as confirmed by a Monte Carlo analysis of the underlying parameter distributions.

This chapter was published as:

Hase, J., Gurin, G., Titov, K., & Kemna, A. (2023). Conversion of Induced Polarization Data and Their Uncertainty from Time Domain to Frequency Domain Using Debye Decomposition. *Minerals, 13*(7), 955. https://doi.org/10.3390/min13070955

## 3.1 Introduction

In geoelectrics, the time-domain induced polarization (TD IP) method is used as an extension of direct current (DC) resistivity measurements to capture information on the ability of the subsurface to develop electrical polarization. Theoretical concepts fundamental to the IP method have been studied over the past few decades, primarily motivated by the method's application to mineral and reservoir characterization (e.g., Bleil 1953; Seigel 1959; Van Voorhis et al. 1973; Nabighian and Elliot 1976; Pelton et al. 1978; Yuval and Oldenburg 1996; Seigel et al. 2007). Although many field-scale IP measurements are conducted in the time domain (TD), the lithological, textural, and hydraulic properties of the targeted rock have been found to relate especially to the spectral characteristics of the IP phenomenon in numerous frequency-domain (FD) laboratory studies (e.g., Vanhala 1997; Binley et al. 2005; Slater et al. 2006; Placencia-Gómez et al. 2013; Gurin et al. 2013; Revil et al. 2015; Martin et al. 2022).

In the context of increasing measurement accuracy of laboratory and field instruments, alongside emerging FD IP analysis approaches in terms of complex resistivity, the petrophysical and hydrogeophysical communities have started to establish the diagnostic potential of the IP method in their research fields (e.g., Vinegar and Waxman 1984; Kemna et al. 2004; Binley et al. 2005; Weller et al. 2010; 2013; 2015). Independent of the specific application at hand, an accurate conversion between TD IP and FD IP data is essential to exploit the FD information contained in TD IP measurements in a quantitative manner. An accurate conversion must provide the possibility to draw quantitative conclusions from the FD characteristic of the IP phenomenon with regard to the petrophysical parameters of interest. Therefore, taking extra effort to ensure an accurate and stable conversion of the data set is sensible. Analytical representations of TD transients can be converted to the FD via the Fourier and Laplace transforms. However, specifically for the conversion of TD IP measurements using standard instrumentation, one faces the problem of sparsely sampled signals, which are typically discretized at 20 time steps or less. To ensure a stable conversion, even of noisy transients, adequate assumptions on their expected shape must be made and included in the conversion. Care must be taken in formulating these assumptions since the use of unsuitable or under-parameterized models can lead to a misrepresentation of the transients and subsequent errors in the conversion. During tomographic inversions of electrical data in the TD and FD, data points are often weighted with their respective errors (e.g., LaBrecque et al. 1996; Kemna et al. 2000). Given individual error estimates for the transients, an adequate error propagation through the conversion scheme into corresponding FD error estimates is therefore essential.

For the conversion of TD IP data sets to the FD, previous studies (e.g., Van Voorhis et al. 1973; Kemna et al. 1997; Binley et al. 2016) have used the assumption of a frequency-independent, constant phase angle (CPA), finding it to be a valid approximation for many laboratory and field applications. As quantitative applications of TD IP measurements call for increasingly high precision, and measurement systems continue to improve, the limitations of the CPA approximation become relevant and must be overcome to fully utilize the quantitative diagnostic potential of the TD IP method. Using a parameterization of the FD complex resistivity in terms of the empirical Cole-Cole model, other studies (Hönig and Tezkan 2007; Fiandaca et al. 2012; 2013; Tezkan 2014) have been able to invert TD IP data for the spatially distributed spectral behavior of electrical properties in the subsurface. Given scenarios for which the assumption of a Cole-Cole-like behavior is valid, this inversion approach yields easy-to-interpret tomographic results and provides the possibility of relating imaged Cole-Cole parameters to petrophysical properties using relations established in laboratory experiments (e.g., Revil et al. 2012). A drawback of the approach is the Cole-Cole model's limitation with respect to the possible complexity of the FD characteristics it can represent, such as the superposition of multiple polarization processes or spectral characteristics that appear asymmetric in log-log plots in general.

In this work, we describe a general-purpose approach for converting tomographic TD IP data sets to the FD. Importantly, the approach also provides the possibility to accurately propagate a TD data error estimate to a corresponding FD error estimate. The TD to FD conversion scheme presented in this paper is based on the concept of Debye decomposition (DD) (e.g., Morgan and Lesmes 1994; Tong et al. 2006b; Nordsiek and Weller 2008). The DD can fit various types of TD transients while including very few prior assumptions on their shape. A measured TD transient is decomposed into a superposition of exponential decays. The decomposition is performed on a grid of predefined relaxation times. Using an inversion approach, the appropriate contribution of each exponential decay to the superposition can be determined, yielding a relaxation-time distribution (RTD). Related by the Laplace transform, equivalent formulations of the DD exist in the TD and FD. Martin et al. (2021) demonstrated this equivalence practically by performing the DD on TD and FD IP data sets obtained during laboratory measurements of the same samples. They found that the estimated RTDs were mostly in agreement with each other, attributing deviations to limitations in TD IP data quality. Therefore, the FD response equivalent to a measured TD transient can be calculated from the estimated RTD. After converting each transient to the FD, we use a tomographic FD inversion code to compute subsurface images of the complex electrical resistivity at single frequencies.

This work is structured as follows: After a short recap of the theoretical background underlying the DD, we formulate the inverse problem the TD to FD conversion is based on. The inverse problem is solved using parameter optimization. We describe the optimization algorithm and explain our choices for the hyperparameters. In a synthetic validation study, we investigate the accuracy and limitations of the TD to FD conversion scheme, complemented by a validation of the error propagation scheme. We conclude with a demonstration of the overall approach on a tomographic TD IP field data set.

## 3.2 Time-domain to frequency-domain conversion of induced polarization data

### 3.2.1 Induced polarization in the time domain

During a TD IP measurement, the transient voltage decay $V(t)$ between the potential electrodes is measured as a function of time $t$ after the termination of the current injection. After an abrupt decrease of the voltage from its primary value $V_0$, associated with the DC resistivity measurement, to a secondary value $V_1$, the voltage decreases continuously:

$$\lim_{t \longrightarrow \infty} V(t) = 0. \tag{3.1}$$

Normalization with respect to the primary voltage gives the normalized IP transient $\eta(t) = \frac{V(t)}{V_0}$. The ratio of the initial voltage drop at the end of the current injection $t = 0$ is known as the chargeability (Seigel 1959). The occurrence of this electrical relaxation phenomenon is an expression of the subsurface's ability to develop electrical polarization under an applied electric field.

### 3.2.2 Debye decomposition

The Debye decomposition (DD) is a semi-phenomenological model with the ability to represent various types of electrical relaxation responses based on the superposition of individual Debye responses. We adopt and modify the FD forward operator of the DD after Nordsiek and Weller (2008):

$$\tilde{Z}(\omega) = R_0 - \sum_{k=1}^{M} \gamma_k \left(1 - \frac{1}{1 + i\omega\tau_k}\right), \tag{3.2}$$

where $M$ is the number of Debye terms, $\omega$ is the angular frequency, and $i^2 = -1$ is the imaginary unit. Equation (3.2) is used to calculate the spectrum of the complex electrical impedance $\tilde{Z}(\omega)$, which is equivalent to the measured TD transient. The relaxation time $\tau_k$ is the characteristic time constant of the $k$-th Debye term. The DC resistance $R_0$ is the magnitude of the electrical impedance at the low-frequency limit of the spectrum:

$$R_0 = \lim_{\omega \longrightarrow 0} |\tilde{Z}(\omega)|. \tag{3.3}$$

The parameters $\gamma_k$ have the unit of resistance and scale the contributions of the different Debye terms to the superposition. By choosing $\gamma_k$ as scaling parameters and thus deviating from the formulation of Nordsiek and Weller (2008), we avoid correlated errors between the different Debye terms in the superposition. Plotting the values of $\gamma_k$ against the corresponding relaxation times $\tau_k$ yields the RTD.

We estimate the values of $\gamma_k$ by inverting the measured TD transient on a grid of predefined relaxation times $\tau_k$, using the TD forward operator which is equivalent to Equation (3.2) (e.g., Tong et al. 2006a;b; Tarasov and Titov 2007):

$$\eta(t) = \frac{1}{R_0} \sum_{k=1}^{M} \gamma_k \exp\left(-\frac{t}{\tau_k}\right). \tag{3.4}$$

A closer investigation of Equation (3.2) shows that it is reasonable to restrict the interpretation of the derived spectrum to the angular frequencies $\frac{1}{\tau_{max}} < \omega < \frac{1}{\tau_{min}}$, which assumes that there is a smallest relaxation time $\tau_{min}$ and a largest relaxation time $\tau_{max}$ that can be resolved with a given measurement. In this work, we choose $\tau_{min}$ and $\tau_{max}$ to be equal to the first and last time values used for the discretization of the transient.

### 3.2.3 Formulation of the inverse problem

The goal of the DD is to decompose a measured TD transient into a RTD. We do not use the discrete values of the normalized TD transient as data, since their errors are correlated due to division by the measured quantity $V_0$. Instead, we choose

$$\mathbf{d} = R_0 \left(\eta_1, \ldots, \eta_i, \ldots, \eta_N\right)^T, \tag{3.5}$$

at discrete time steps

$$\mathbf{t} = \left(t_1, \ldots, t_i, \ldots, t_N\right)^T, \tag{3.6}$$

which provides us with uncorrelated measurements to invert. In the model domain, the inverse problem is discretized on a grid of $M$ predefined, $\log_{10}$-spaced, relaxation times $\tau_k$. It is critical that the model domain discretization covers a wide enough parameter range and provides enough degrees of freedom. With the first and last time steps of the discretized transient being $t_1$ and $t_N$, we choose $\tau_k \in [10^{\log_{10}(t_1)-1.5}, 10^{\log_{10}(t_N)+1.5}]$, extending the discretization of the model domain by 1.5 decades to the left and right of the sampled time frame. The number of relaxation times $M$ is based on the number of decades covered by the model-domain discretization, so that the density of the model-domain discretization is consistent for differently sampled transients. For each decade in $\tau_k$, we use 25 relaxation times for the discretization of the model domain, which is 5 relaxation times more than the 20 per decade recommended by Weigand and Kemna (2016), ensuring enough degrees of freedom. To account for the wide range of values within $\gamma_k$ and to restrict the inversion from yielding results associated with $\gamma_k < 0$, the natural logarithms of $\gamma_k$ are used as the model parameters:

$$\mathbf{m} = \left(\ln\left(\frac{\gamma_1}{\gamma_0}\right), \ldots, \ln\left(\frac{\gamma_k}{\gamma_0}\right), \ldots, \ln\left(\frac{\gamma_M}{\gamma_0}\right)\right)^T. \tag{3.7}$$

Note that the division by $\gamma_0 = 1\,\Omega$ is necessary to ensure that the argument of $\ln(\cdot)$ is dimensionless. For simplicity, this is implied in the notation $\ln\left(\frac{\gamma_k}{\gamma_0}\right) = \ln\left(\gamma_k\right)$ from here on.

The TD forward operator of the DD is modified as

$$\tilde{Z}(t) = \sum_{k=1}^{M} \exp\left(\ln\left(\gamma_k\right) - \frac{t}{\tau_k}\right), \tag{3.8}$$

leading to the discrete TD forward operator (e.g., Kumar et al. 2019)

$$f_i(\mathbf{m}, t_i) = \sum_{k=1}^{M} \mathcal{G}_{ik} \exp(m_k), \tag{3.9}$$

with

$$\mathcal{G}_{ik} = \exp\left(-\frac{t_i}{\tau_k}\right). \tag{3.10}$$

Setting up the forward operator as a matrix-vector multiplication is favorable in terms of computational performance due to the possibility of parallel computing. Note that we formulate $\mathbf{f}(\cdot)$ as a function of $\mathbf{m}$ and $\mathbf{t}$. In most cases, $\mathbf{t} = \text{const}$. The only exception is in Section 3.2.4, where we discuss the stacking of subsequent injection pulses for a given model realization, hence $\mathbf{m} = \text{const}$. From here on we only explicitly pass the argument to the forward operator that is not constant.

The inverse problem that results from Equation (3.9) is non-linear. The corresponding cost function

$$\Psi(\mathbf{m}) = \frac{1}{2}\left(\mathbf{d} - \mathbf{f}(\mathbf{m})\right)^T \mathbf{C}_{\mathbf{d}}^{-1}\left(\mathbf{d} - \mathbf{f}(\mathbf{m})\right) + \frac{1}{2}\lambda \mathbf{m}^T \mathbf{R} \mathbf{m}, \tag{3.11}$$

is minimized iteratively using a pseudo-Newton model update, as described in Tarantola (2005):

$$\mathbf{m}_{q+1} = \mathbf{m}_q + \varepsilon \Delta \mathbf{m} = \mathbf{m}_q - \varepsilon \left(\mathbf{G}_{TD}^T \mathbf{C}_{\mathbf{d}}^{-1} \mathbf{G}_{TD} + \lambda \mathbf{R}\right)^{-1} \left(\mathbf{G}_{TD}^T \mathbf{C}_{\mathbf{d}}^{-1} \left(\mathbf{f}(\mathbf{m}_q) - \mathbf{d}\right) + \lambda \mathbf{R} \mathbf{m}_q\right). \tag{3.12}$$

The Jacobian for the TD formulation and the step length are represented by $\mathbf{G}_{TD}$ and $\varepsilon$ respectively. The entries of the Jacobian are give by the partial derivatives of the forward operator with respect to the model parameters:

$$G_{TD,ik} = \frac{\partial f_i}{\partial m_k}. \tag{3.13}$$

Since the inverse problem is underdetermined, regularization $\lambda > 0$ has to be applied to ensure that $\left(\mathbf{G}_{TD}^T \mathbf{C}_{\mathbf{d}}^{-1} \mathbf{G}_{TD} + \lambda \mathbf{R}\right)$ can be inverted. We use a roughness operator $\mathbf{R}$ that minimizes the squared difference between the model parameters of the neighboring Debye terms. The strength of the applied regularization is controlled by the parameter $\lambda$. Measurement uncertainties are accounted for in the data-precision matrix $\mathbf{C}_{\mathbf{d}}^{-1}$. The root-mean-square error

(RMSE)

$$\text{RMSE} = \sqrt{\frac{(\mathbf{d} - \mathbf{f}(\mathbf{m}))^T \, \mathbf{C}_{\mathbf{d}}^{-1} (\mathbf{d} - \mathbf{f}(\mathbf{m}))}{N}} \tag{3.14}$$

is used to estimate the goodness of the data fit achieved by a given model realization in the context of the measurement uncertainties. For each iteration, the step length $\varepsilon$ is optimized automatically using a line-search approach described in Kemna (2000). During the line search, three trial-model updates are calculated for $\varepsilon_{\text{trial}} \in \{0, \, \varepsilon/2, \, \varepsilon\}$ and their corresponding data fits RMSE are evaluated. The updated step length is then chosen as the minimum of a parabola fitted through $\text{RMSE}(\varepsilon_{\text{trial}})$. The inversion is terminated if the norm of the model update $|\Delta\mathbf{m}|$ vanishes, indicating that the maximum a posteriori (MAP) solution has been found.

### 3.2.4 Adaptation to common data-acquisition strategies

Most TD IP measurement systems use gate integration during the measurement in order to reduce high-frequency noise. This means that the transient returned by the instrument is actually a sequence of mean values, each of which is calculated for a corresponding time gate. Different choices can be made for the widths of the time gates. Given the case where the widths of the time gates increase in a $\log_{10}$-manner, Fiandaca et al. (2012) suggest using the center of the time gates, calculated using the geometric mean, as the time points to represent the averaged values in the transient. Since this resolves the problem of adjusting the forward operator to the gate integration, we use transients sampled at $\log_{10}$-spaced time steps.

During a TD IP measurement, a sequence of opposing current pulses is injected into the subsurface. The measured TD transient is calculated as the mean of the transients induced by these pulses to increase the signal-to-noise ratio. For a given model realization $\mathbf{m} = \text{const}$, the forward operator has to be extended as (e.g., Tarasov and Titov 2007; Fiandaca et al. 2012):

$$\mathbf{f}_{\text{Stack}_j}(\mathbf{t}) = \sum_{m=1}^{j} \sum_{k=1}^{2} (-1)^{m+k} \, \mathbf{f}\left(\mathbf{t} + \mathbf{1}(k-1)T_{\text{On}} + \mathbf{1}(j-m)(T_{\text{On}} + T_{\text{Off}})\right) \tag{3.15}$$

and

$$\mathbf{f}_A(\mathbf{t}) = \frac{1}{N_{\text{Stacks}}} \sum_{j=1}^{N_{\text{Stacks}}} (-1)^{j+1} \, \mathbf{f}_{\text{Stack}_j}(\mathbf{t}), \tag{3.16}$$

where $\mathbf{f}(\cdot)$ represents the forward calculation given in Equation (3.9), $\mathbf{f}_{\text{Stack}_j}$ represents the $j$-th transient with the superposition of the transients from prior injection pulses taken into account, and $\mathbf{f}_A$ is the averaged transient after $N_{\text{Stacks}}$ stacks. We use the formulation in Equation (3.16) to adjust the forward calculation $\mathbf{f}(\cdot) \leftarrow \mathbf{f}_A(\cdot)$ appropriately when dealing with stacked transient data.

## 3.3 Uncertainty approximation and propagation

Choosing a suitable regularization strength is essential for the conversion, as well as the error propagation from the TD to the FD. In our work, we base the choice of an appropriate regularization strength on the RMSE, assuming that we have a good estimate of the data uncertainty. We choose the regularization strength in such a way that the MAP solution achieves a RMSE $= 1$, fitting the measurements appropriately in the context of their respective uncertainties (e.g., deGroot Hedlin and Constable 1990; LaBrecque et al. 1996; Kemna 2000). Details of our approach for finding the optimal regularization strength $\lambda_{\text{final}}$ can be found in Appendix 3.A.

The analytical propagation of measurement errors from the TD to the FD is based on an adequate uncertainty characterization in the model domain. Here, $\lambda\mathbf{R}$ can be identified as the precision matrix of the prior term. Assuming normally distributed model-parameter uncertainties near the MAP solution, the posterior covariance matrix (Tarantola 2005)

$$\mathbf{C_m} = \left(\mathbf{G}_{TD}^T \mathbf{C_d}^{-1} \mathbf{G}_{TD} + \lambda\mathbf{R}\right)^{-1} \tag{3.17}$$

is approximated from the result of the inversion. It can be used as an uncertainty measure for the estimated model parameters, considering both the measurement uncertainty and prior uncertainty. Using error propagation, the following formulation can be used for the mapping of the data errors to the model domain (Gubbins 2004):

$$\mathbf{C_e} = \mathbf{C_m}\, \mathbf{G}_{TD}^T\, \mathbf{C_d}^{-1}\, \mathbf{G}_{TD}\, \mathbf{C_m}. \tag{3.18}$$

Equation (3.18) isolates the propagated uncertainty of the inverted measurements and is, therefore, the approximation used for the error propagation from the TD to the FD. The Jacobian of the FD response can be calculated from the partial derivatives with respect to the model parameters $\ln(\gamma_k)$. For the $k$-th model parameter, we find

$$\mathbf{G}_{FD,k} = \begin{pmatrix} \frac{\partial Z'(\omega)}{\partial \ln(\gamma_k)} & \frac{\partial Z''(\omega)}{\partial \ln(\gamma_k)} \end{pmatrix}_k^T = \begin{pmatrix} -\gamma_k \frac{(\omega\tau_k)^2}{1+(\omega\tau_k)^2} & -\gamma_k \frac{\omega\tau_k}{1+(\omega\tau_k)^2} \end{pmatrix}_k^T, \tag{3.19}$$

for the formulation in terms of the real and imaginary parts. The covariance matrix for the real and imaginary parts is calculated from $\mathbf{G}_{FD}$ and $\mathbf{C_e}$, while also accounting for the uncertainty of $R_0$:

$$\mathbf{cov}(Z', Z'') = \operatorname{var}(R_0) \begin{pmatrix} 1 & 0 \\ 0 & 0 \end{pmatrix} + \left(\mathbf{G}_{FD}\mathbf{C_e}\mathbf{G}_{FD}^T\right). \tag{3.20}$$

From the covariance matrix of the real and imaginary parts, the covariance matrix of the logarithmic impedance magnitude and phase can be obtained according to:

$$\mathbf{cov}(\ln|Z|, \varphi) = \begin{pmatrix} \frac{\partial \ln|Z|}{\partial Z'} & \frac{\partial \ln|Z|}{\partial Z''} \\ \frac{\partial \varphi}{\partial Z'} & \frac{\partial \varphi}{\partial Z''} \end{pmatrix} \mathbf{cov}(Z', Z'') \begin{pmatrix} \frac{\partial \ln|Z|}{\partial Z'} & \frac{\partial \ln|Z|}{\partial Z''} \\ \frac{\partial \varphi}{\partial Z'} & \frac{\partial \varphi}{\partial Z''} \end{pmatrix}^T. \tag{3.21}$$

## 3.4 Synthetic validation study

### 3.4.1 Accuracy of the time-domain to frequency-domain conversion

To investigate the accuracy of the approach described above when extracting information at a frequency of 1 Hz, we tested it on 30 synthetic transients of varying relaxation time:

$$d(t_i) = \frac{R_0 V_1}{V_0} \exp\left(-\frac{t_i}{\tau_s}\right), \tag{3.22}$$

with $R_0 = 1\,\Omega$, $\frac{V_1}{V_0} = 0.1$, and $\tau_s \in [10^{-2}, 10]\,\mathrm{s}$. The synthetic transients were discretized over 20 time gates, with geometric means $t_i$ that were $\log_{10}$-spaced between 0.1 s and 1 s. Noise with a relative error of 1% and an absolute error of $10^{-6}\,\Omega$ was added to the synthetic measurements. The pseudo-random number generator was initialized with the same seed for all synthetic transients, so that the added noise realization was always the same. During the DD, the standard deviation of the synthetic noise was accounted for by modification of the data-precision matrix $\mathbf{C}_\mathbf{d}^{-1}$. During the inversion of all synthetic transients, the regularization strength was adapted to the data uncertainty to achieve a data fit of RMSE = 1. We evaluated the accuracy of the conversion by investigating its ability to estimate the phase of the complex electrical impedance, the results of which are shown in Figure 3.1. The expected phase value for a given synthetic transient was calculated analytically. Although the misfit between the expected phase and estimated phase is high for the conversion of very fast relaxation processes, the estimation is exact if the relaxation time $\tau_s$ of the synthetic transient lies within the sampled time frame from 0.1 s to 1 s. For slower relaxation processes, the accuracy of the conversion does not drop as drastically as it does for faster relaxation processes. Up to a relaxation time of $\tau_s = 10\,\mathrm{s}$, a good estimation of the phase seems possible through the extrapolation of the information contained in the synthetic measurements. The achieved data fits were all close to the target value of RMSE = 1, as shown in Figure 3.1. The optimized regularization strength $\lambda_{\text{final}}$ was minimal for synthetic transients with relaxation times within the sampled time frame. Here, the inversion was dominated by the measurements. For values of $\tau_s$ outside the sampled time frame, the inversion was dominated by the prior information, which corresponds to higher estimates of $\lambda_{\text{final}}$.

### 3.4.2 Validation of error propagation

The error propagation from the TD to the FD is based on the existence of a suitable covariance matrix for describing the estimated RTD's uncertainty. Equation (3.18) provides such an estimate for the mapping of the data errors to the model domain, assuming normal data error and model-parameter distributions. To validate the error propagation from the TD to the model domain, we created $10^4$ noise realizations of Equation (3.22) with $\frac{V_1}{V_0} = 0.1$, $\tau_s = 0.5\,\mathrm{s}$, and $R_0 = 1\,\Omega$, as exemplarily shown in Figure 3.2. The error on $R_0$ was simulated by adding a synthetic noise realization with a 10% relative error and a $5 \times 10^{-3}\,\Omega$ absolute error to $R_0$. The synthetic transient was discretized over 20 $\log_{10}$-spaced time gates with geometric means $t_i$ between 0.1 s and 1 s to create the synthetic measurements. The noise added to the synthetic transient had a relative error of 1% and an absolute error of $10^{-6}\,\Omega$. Inversions were performed with a fixed regularization strength, meaning that variations in the cost function

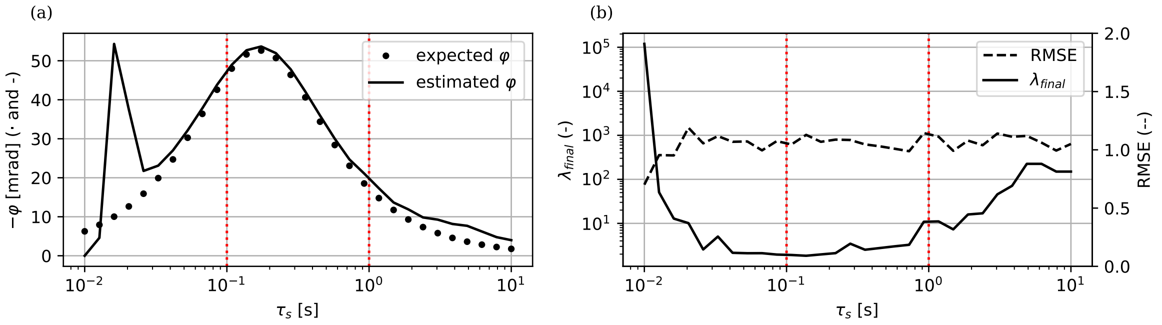

**Figure 3.1:** Results of the synthetic validation study to investigate the accuracy of the conversion scheme. The conversion was performed on input signals of varying relaxation times. **(a)** Phase estimates obtained from the conversion in comparison to their expected, analytically calculated counterparts. The dotted red vertical lines mark the lower and upper bounds of the sampled time frame. For signals resolved by the measurement, the conversion scheme achieved a good fit between the expected phase and the estimated phase. **(b)** Achieved data fit RMSE and optimized estimate for the regularization strength $\lambda_{\text{final}}$ plotted against the relaxation time of the respective input signal.

(3.11) only occurred in the data misfit term and not in the prior term, isolating the scatter in the estimated model parameters that was caused by the noise on the synthetic measurements. Because the discretization at 20 time steps only provided a limited sample of the noise, and the regularization strength was not adapted to the specific noise realization, the achieved values for RMSE showed a scatter. The regularization strength was chosen to be $\lambda = 1$, yielding scattering RMSE values with a mean $\approx 1$.

The synthetic validation study shows that although the distributions of the model parameters deviate from the normal distribution, they are otherwise well-behaved (see Figure 3.2 for an example of a model parameter). The distributions of the model parameters obtained during the synthetic study were used to calculate the reference covariance matrix and to validate the choice of the uncertainty estimate in the model domain, which was used for the error propagation and calculated according to Equation (3.18). Figure 3.3 shows a comparison of the reference matrix calculated from the scatter of the model-parameter estimates and the approximations of $\mathbf{C_m}$ and $\mathbf{C_e}$ using Equations (3.17) and (3.18), which were calculated from the inversion result of the noise-free decay. As expected, $\mathbf{C_m}$ shows strong deviations from the reference matrix, since it includes the uncertainty of the prior information and does not isolate the mapping of the data errors to the model domain. The matrix $\mathbf{C_e}$ is a much better approximation of the reference matrix. However, although it captures the overall shape, $\mathbf{C_e}$ also shows deviations from the reference matrix. These can be traced back to the assumption of normally distributed model-parameter estimates underlying Equation (3.18), which is violated in some cases, as shown in Figure 3.2. We therefore assume $\mathbf{C_e}$ to be a valid but not completely exact approximation of the uncertainty in the model domain. To investigate the distributions of the FD impedance estimates, the FD responses of all $10^4$ RTDs were calculated at 1 Hz, and are shown in Figure 3.2. The distributions of $\ln |Z|$ and $\varphi$ are not normal but are otherwise well-behaved.

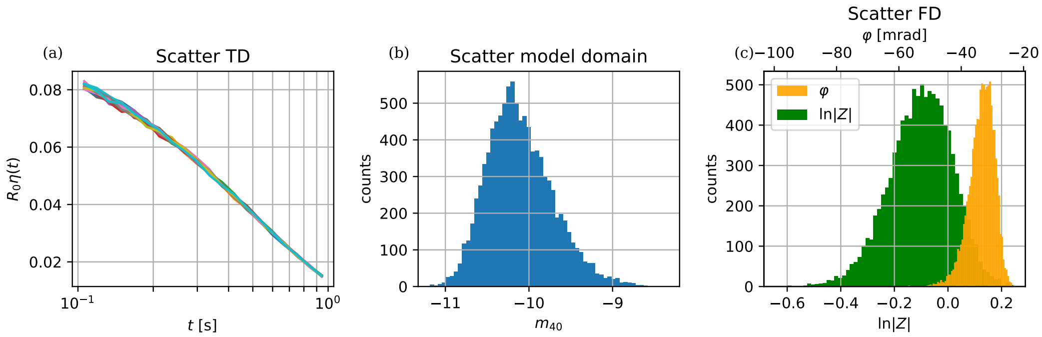

**Figure 3.2:** **(a)** Noise realizations of the input transient. **(b)** Scatter of model parameter $m_{40}$. **(c)** Scatter of the obtained FD impedance estimates.

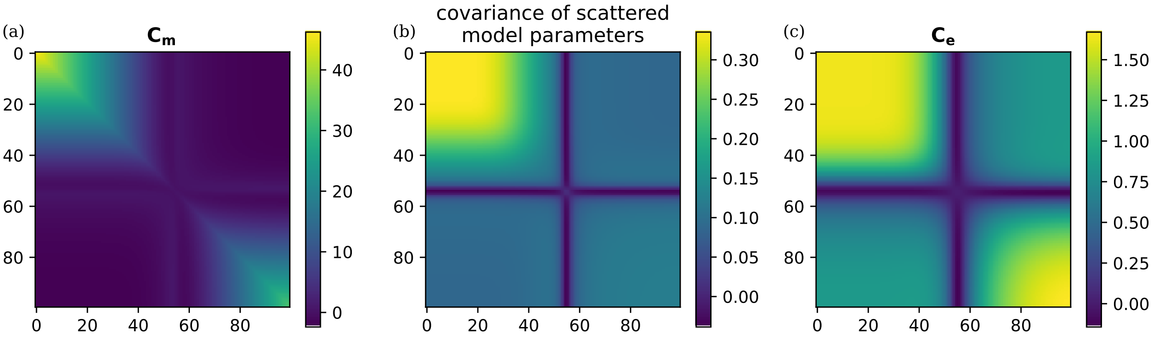

**Figure 3.3:** Comparison of the different approximations for the covariance matrix of the estimated RTD. **(a)** Covariance matrix calculated according to Equation (3.17). **(b)** Reference covariance matrix obtained from the Monte Carlo analysis. **(c)** Covariance matrix calculated according to Equation (3.18). It can be seen that the covariance matrix calculated using Equation (3.18) represents the superior approximation in this comparison.

The scatter of the FD impedance estimates calculated using the inversion results with $\lambda = 1$ was used to estimate the reference standard deviation for the individual components of the FD impedance estimates. To validate the accuracy achieved by the error propagation scheme, we performed the conversion for $10^3$ noise realizations, for which we adapted $\lambda$, calculated the FD error estimate for each FD impedance estimate, and compared the mean of the error estimates to the reference. Figure 3.4 shows the distributions of the estimated standard deviations for the different components of the FD impedance estimates. The standard deviations of $\ln|Z|$ and $\varphi$ are well estimated by the proposed error propagation scheme.

## 3.5 Demonstration of the application to tomographic field measurements

We demonstrate the application of the new conversion approach to tomographic field measurements on a TD IP data set that was measured in the Maletoyvaemskoie ore field (MOF), located in the central part of the Maketoyvaemskoie ore cluster in the North Kamchatka region (Russia, compare Figure 3.5). Geologically, the field site is located in the central part of a volcanic-tectonic structure that represents a stratovolcano. The stratovolcano is

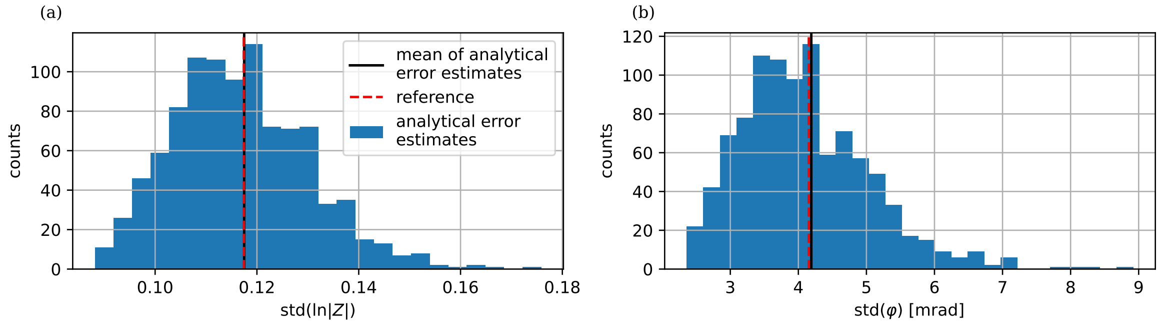

**Figure 3.4:** Results of the synthetic validation study to test the error propagation scheme for **(a)** the impedance magnitude, and **(b)** the impedance phase. The dashed red vertical lines indicate the values of the reference standard deviations obtained from the distributions of the FD impedance estimates displayed in Figure 3.2. Shown in blue are the distributions of the error estimates propagated analytically using the proposed scheme for multiple noise realizations of the same TD transient. It can be seen that the mean values of the analytically propagated error estimates, indicated by the black vertical lines, approximate the reference values very well, indicating the validity of the proposed error propagation scheme.

located within the Koryak-Central Kamchatsky belt of the Neogen-Quaternary age and is composed of Early Miocene stratified volcanic and sedimentary rocks (effusive, pyroclastic, and tuff-sedimentary rocks predominantly of Andesitic composition) with different degrees of hydrothermal and metasomatic alteration. The MOF includes three gold objects considered small HS (high sulfidation)-type gold deposits (Yugo-Zapadnoye, Gaching, and Yubileinoye), several gold anomalies superimposed with copper-arsenic sulfosalt mineralization, and copper anomalies (Volchkov and Zvezdov 1997; Tolstykh et al. 2018). Most of the discovered ore bodies are of high chargeability (e.g., Gurin 2021). The MOF features massifs of secondary quartzites with pronounced horizontal zonality, which are typical for HS-type deposits. Epithermal gold deposits of HS type are the new types of deposits found in the far east of Russia. To date, only a few economically important HS deposits have been discovered within the region. They are settled within young volcano-sedimentary belts, where hydrothermally altered (advanced argillic) rocks have formed due to the aside alteration of initial rocks by hydrothermal processes within active hydrothermal systems, surrounding the gold HS deposits. Numerous fields of altered rocks have been discovered within the Kamchatka peninsula, being potential sources of high-grade and large-tonnage epithermal gold-silver and copper-porphyry deposits. Starting in the year 2000, gold prospecting was carried out in the MOF. There have been significant efforts to characterize the field site using geophysical and petrophysical surveys. Geoelectric measurements have been complemented by information from other geophysical methods, such as geomagnetic measurements, and geological surveys. Gurin (2021) presented the results and interpretations of multiple geophysical and petrophysical surveys carried out between 2016 and 2017 in the central part of the MOF. The IP characteristics of the field site have been previously analyzed (e.g., Gurin et al. 2023). The extensive studies that have been conducted in the area provide the basis on which the validity of our results, obtained from the conversion and subsequent tomographic inversion of the TD IP data, can be assessed. The TD IP data set was obtained using pole-dipole measurements, which were carried out along a 2400 m long profile, utilizing an injection and off-time of 1 s and a total of 15 stacks. A potential dipole with an electrode separation of 20 m was used while the current electrode was moved on a 100 m grid. The second current electrode, assumed to be located at an infinite distance during the tomographic inversion, was placed 3500 m away from the nearest point on the profile. For data acquisition, an AIE-2 instrument was used, featuring a VP-1000 (1 kW power) transmitter and a VP-MPP receiver. No low-pass filter was used during the data acquisition, eliminating the need to correct the early times of the transients for the corresponding effects.

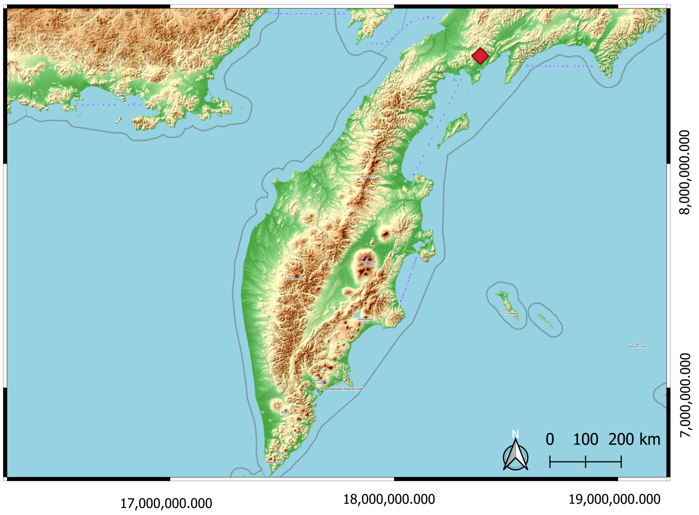

**Figure 3.5:** Kamchatka, with the location of the Maletoyvaemskoie ore field indicated in red. Map by OpenStreetMap (OSM) OpenStreetMap contributors (2017). Coordinate System: WGS 84. A detailed geological map of the field site is provided in Gurin (2021).

The workflow we followed during the processing of the tomographic TD IP field data set is presented in Figure 3.6. To assess the general data quality, filter transients that showed highly erratic behavior, and later quantify errors, we followed Flores Orozco et al. (2018b) and started the data processing by fitting a power-law model to the measured TD transients. Note that the power-law model

$$d(t_i) = a{t_i}^b \tag{3.23}$$

approximates the TD equivalent of the CPA spectrum of the electrical impedance (Van Voorhis et al. 1973) given by:

$$\tilde{Z}(\omega) = R_n(i\omega)^{-b}. \tag{3.24}$$

By basing the filtering on the Pearson correlation coefficient between the measured decay and the response of the fitted power-law model, we define erratic behavior as a strong deviation from the CPA behavior. We excluded transients with $r < 0.9$ from the data processing, interpreting them as non-physical. This filter reduced the total size of our data set by 9%. Examples of transients and their corresponding Pearson correlation coefficients are shown in Figure 3.7.

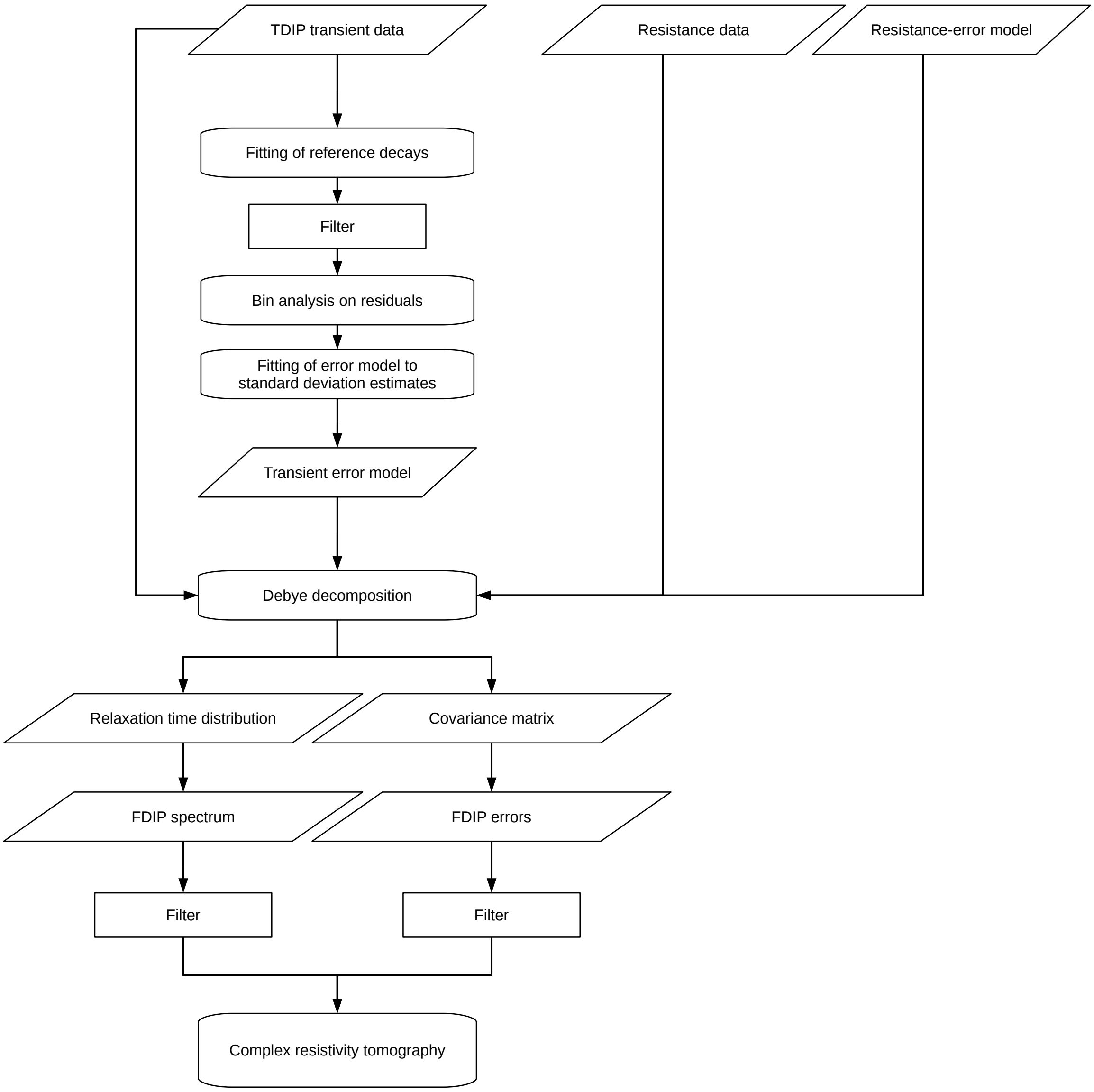

**Figure 3.6:** Illustration of the workflow followed during the TD IP field-data processing.

Since the error quantification aims to characterize the statistical uncertainty of the data, performing it after filtering non-physical transients from the data set is reasonable. Based on the scatter of the measurements around the responses of the fitted power-law models, we estimated the standard deviations of $d_i$ by performing a bin analysis (Koestel et al. 2008). We calculated the residuals of all $d_i$ readings to the power-law model response and plotted them against the $d_i$ readings themselves. After subdividing the data set into $\log_{10}$-spaced bins, we estimated the standard deviations corresponding to the different bins from the scatter of the residuals within them. Finally, we fitted a linear error model through the estimated standard deviations, as shown in Figure 3.8. To account for the varying number of residuals within the different bins, we weighted the estimated standard deviations by $\frac{1}{\sqrt{N_{\mathrm{Bin}}}}$ during the fit. The fitted error model was used to estimate the standard deviations of all $d_i$ readings during the TD to FD conversion. To account for the simplicity of the fitted power-law model and allow for more complex RTDs, we slightly adjusted the fitted error model by reducing the absolute

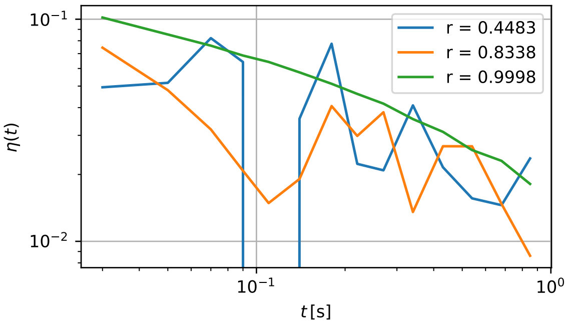

**Figure 3.7:** Examples of transients from the TDIP field data set, for which the fitted power-law model achieved specific Pearson correlation coefficients. Transients with $r < 0.9$, representing 9% of the data set, were rejected by our filter and excluded from further processing and inversion.

error (see Figure 3.8). For the DC resistances, we used a linear error model with relative and absolute errors of 9% and $5 \cdot 10^{-3}\,\Omega$, respectively. Lacking reciprocal measurements, these parameters were chosen conservatively and in such a way that the results of the TD to FD conversion, as well as those of the tomographic inversion, were robust with regard to small changes in the values chosen for the transient error model.

The inversions of all the measured TD transients into RTDs were performed with the

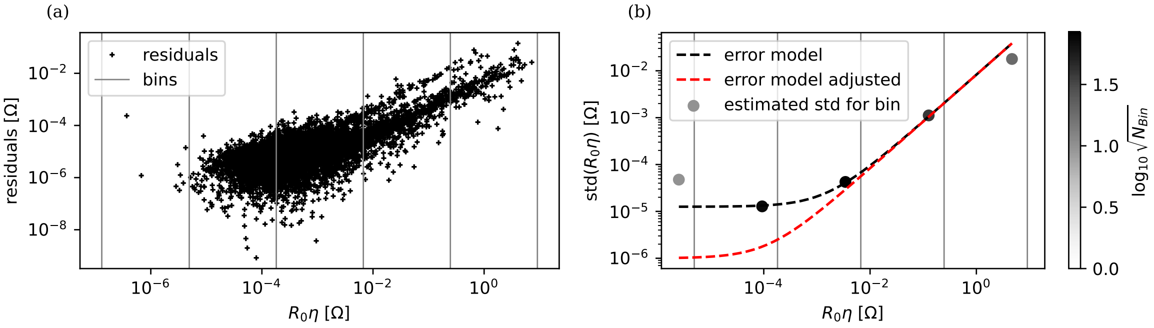

**Figure 3.8:** Results of the error analysis performed on the TD IP data set to obtain an error model for the TD transients. **(a)** Bin analysis. The scatter of the residuals within each bin was used to calculate a corresponding standard deviation. **(b)** Linear error model fitted to the estimated standard deviations. The error model used for the inversion of the TD transients was adjusted manually and is indicated in red. The estimated standard deviations for the bins are indicated in shades of gray, representing the number of data points in the corresponding bin.

adaptation of the regularization strength to the data uncertainty. Figure 3.9 shows the development of the RMSE and $\lambda$ during the inversion process for the example transients. All inversions started with a high RMSE of the starting model, which decreased significantly during the first 10 iterations. Note that the development of the RMSE shows discontinuities at the iterations during which the regularization strength $\lambda$ was updated.

The estimated RTDs are of varying complexity, as displayed in Figure 3.9. Although some show no or only one peak, others feature multiple peaks and structures that indicate the

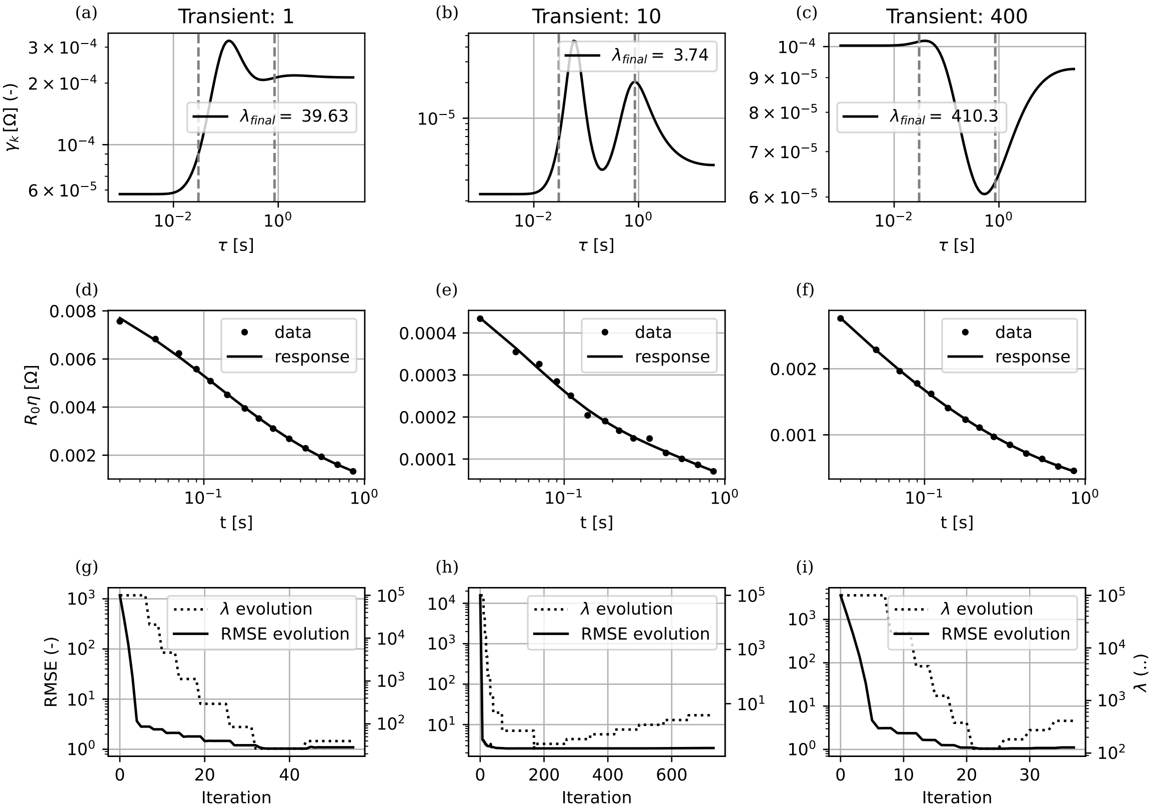

**Figure 3.9:** Results obtained from the DD of transients 1, 10, and 400. **(a-c)** Estimated RTDs, which were of varying complexity. **(d-f)** Achieved data fits. **(g-i)** Evolution of the regularization strength $\lambda$ and data fit RMSE over the course of the optimization.

presence of relaxation phenomena, which can not be quantitatively described by the CPA assumption or single Debye or Cole-Cole terms. Generally, the estimated RTDs achieve good data fits, as shown in Figure 3.9. For every converted transient, we extracted electrical impedance data from the FD responses at 1 Hz and 20 Hz, and used the magnitude and phase values as input for the tomographic inversions. Prior to the tomographic inversions, we filtered the data set based on the histograms of the apparent resistivity magnitude and phase, as shown in Figure 3.10, and excluded all measurements associated with geometric factors larger than 50,000. Figure 3.11 shows the FD error estimates at 1 Hz. We fitted established error models through the data set to demonstrate the systematic behavior of the error estimates. For the phase-error model, we used the inverse power-law relation proposed by Flores Orozco et al. (2012b):

$$\mathrm{std}(\varphi) = a|Z|^{-b} + c, \tag{3.25}$$

whereas for the magnitude-error model, we followed the standard linear assumption, featuring relative and absolute errors. For the tomographic inversion, we used the individual error estimates rather than the ones associated with the fitted-error models. We were unable to obtain stable tomographic inversion results when including data points with phase errors $\mathrm{std}(\varphi) < 1$ mrad, so we excluded them. As can be seen from the scatter plot of the phase errors in Figure 3.11, this mainly corresponded to data points with a high impedance magnitude

$|Z|$, which mainly occur in our data set for the very shallow region between meters 2000 and 2500 of the profile. Due to the resulting local sparsity of the data points, the tomographic inversion result is less data-driven in that region.

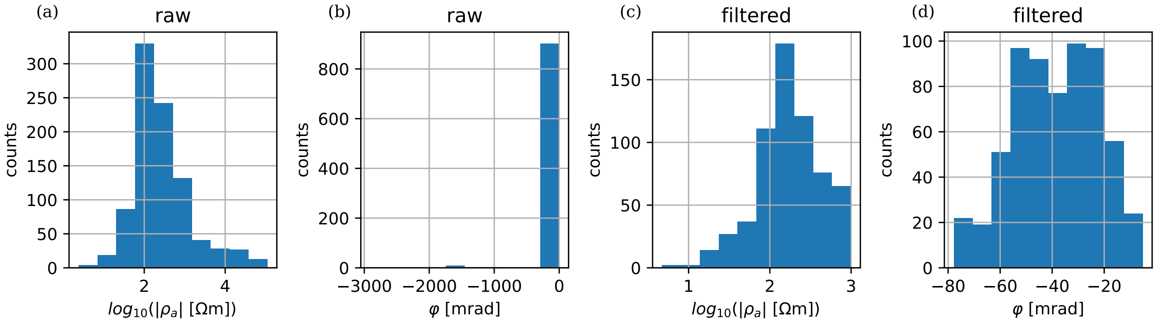

**Figure 3.10:** Distributions of the FD impedance estimates obtained from the conversion, before and after the filtering of outliers. **(a, b)** Estimates of the apparent resistivity and phase before the application of the filter. **(c, d)** Estimates of the apparent resistivity and phase after the application of the filter.

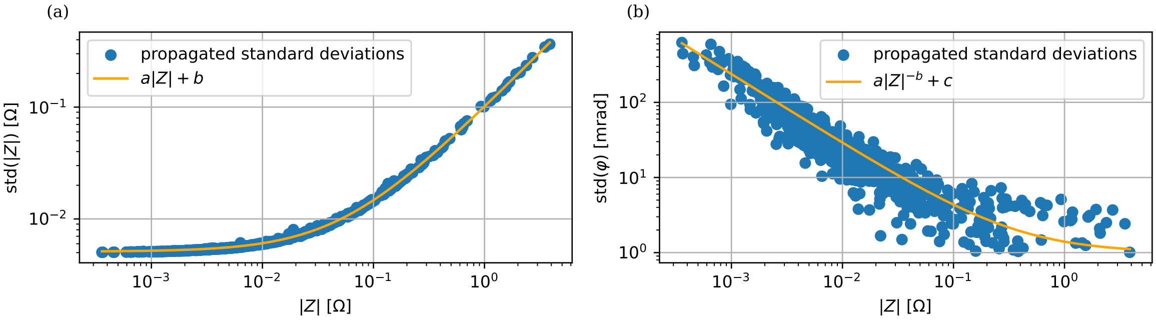

**Figure 3.11:** Error estimates for the individual data points at a frequency of 1 Hz obtained from the error propagation scheme. Commonly used error models, plotted in orange, were able to successfully capture the systematic behavior of the estimated standard deviations. The error models were fitted only for demonstration purposes. During the tomographic inversion, the individual error estimates were used. **(a)** Standard deviations of the estimated magnitudes, which followed a linear trend. **(b)** Standard deviations of the estimated phases, which followed a trend that could be fitted using a power law.

The tomographic inversions were performed using a finite element-based and smoothness constrained complex resistivity inversion code developed by Kemna (2000). Figure 3.12 displays the results of the tomographic inversion at 1 Hz, alongside a plot of the estimated coverage, which shows the regions of the model that are less constrained by the measurements. The obtained images of the complex resistivity are realistic, given the expected geological context. The estimated phases take values from 0 mrad to −60 mrad. Large absolute phase values between −40 mrad and −60 mrad are primarily located at the start (left) of the profile and extend up to 1700 m. These large absolute phase values also coincide with larger values of $\sigma''$, as shown in Figure 3.13, which is approximately proportional to the metal factor (e.g., Marshall and Madden 1959; Hallof 1964) for the phase angles we considered. In contrast to the phase, large absolute values of $\sigma''$ can be seen in the region between 2500 m and 3000 m. In the shallow region around 1500 m, a reduction in $\sigma''$ occurs. We can attribute this reduction in $\sigma''$ near the surface to the presence of quartzites and interpret the large $\sigma''$ values at depths from 600 to 1800 m to be caused by copper-porphyry deposits, located within moderately to strongly sulfidized rocks. With respect to the possible exploration of deposits in the MOF, the described region can be classified as a promising area for potential copper mining. For further information on prospective areas in the MOF deduced from geophysical measurements at the study site, we refer the reader to Gurin (2021). Although the frequency dependence of the magnitude was negligible, the frequency dependence of the phase can be clearly seen from the comparison of the inversion results at 1 Hz and 20 Hz, as displayed in Figure 3.14. This spectral behavior can be interpreted further, for example, in terms of the associated relaxation times. Assuming a single dominant relaxation process $\tau_{peak}$, the difference plot at the bottom in Figure 3.14 indicates $\tau_{peak} < \frac{1}{2\pi}$ s in the red regions and $\tau_{peak} > \frac{1}{40\pi}$ s in the blue regions. As the radius of ore grains relates to the relaxation time $\tau_{peak}$ (e.g., Pelton et al. 1978; Wong 1979; Gurin et al. 2013; Revil et al. 2022), the spectral characteristics captured by our conversion approach could be interpreted in terms of the expected ore grain size. Furthermore, the spectral behavior displayed in Figure 3.14 is consistent with our interpretation of the $\sigma''$ image (see Figure 3.13). Note that parts of the blue region in the difference plot coincide with areas of lower coverage (see Figure 3.12).

## 3.6 Discussion

The presented work shows that a quantitative TD to FD conversion of IP transients using Debye decomposition (DD) is possible and can be applied to tomographic TD IP data sets. The major precondition for the application of the described approach is the suitability of the DD to describe the polarization process at hand. Other limitations of the approach can be traced back to the limited information content in the TD IP measurements themselves. A symptom of this is the high phase error, caused primarily by the relatively small number of time gates used to discretize the transients, which is often $N = 20$ or less for TD IP field instruments. The phase error can be drastically reduced by a more accurate sampling of the transients, with the noise level on the TD transient remaining unchanged. Furthermore, the presented approach is unable to yield accurate FD impedance estimates for relaxation processes that are not resolved by the measurement, as shown in Figure 3.1. For relaxation processes far beyond the measured time interval, or in the case of highly erratic behavior, our approach can fail to invert a given transient into an appropriate RTD. A prior assessment of a given data set is therefore necessary, forcing the user to make a judgment on whether a quantitative analysis and interpretation of the data set is appropriate or not.

During the error propagation from the TD to the FD, we exclusively focus on statistical errors. As the TD to FD conversion is non-linear, the analytical error propagation is not mathematically exact, and the estimate of the FD uncertainty will always be an approximation of the real error. Numerical approaches could be more suited for exact error propagation, but may potentially increase the computational effort to a level exceeding what is reasonable

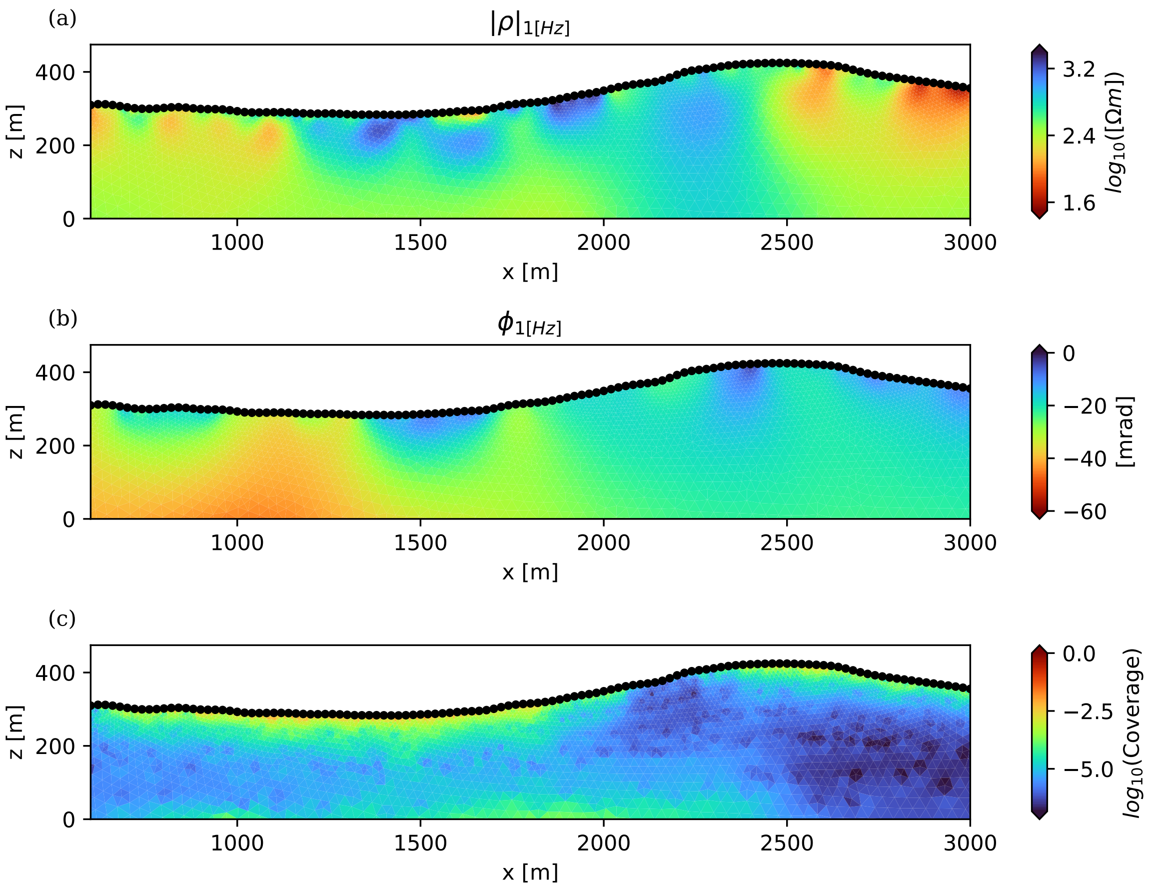

**Figure 3.12:** Tomographic inversion results for spectral data extracted at a frequency of 1 Hz. **(a)** Estimated magnitude of the complex resistivity $|\rho|$. **(b)** Phase of the complex resistivity $\phi$. **(c)** Coverage achieved by the measurement.

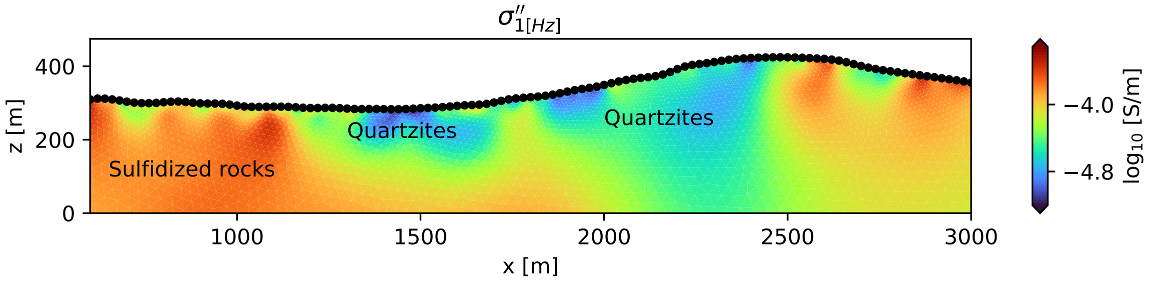

**Figure 3.13:** Image of $\sigma''$ obtained from the tomographic inversion at 1 Hz.

when applying the conversion to larger-scale tomographic TD IP data sets. For the inversion of a TD transient into a RTD, we set up our algorithm to estimate the natural logarithms of $\gamma_k$. This worked well for all the cases we encountered during our work since we avoided negative estimates for $\gamma_k$ and achieved a higher consistency in the estimated RTDs. However, the following theoretical inconsistencies were introduced with regard to the assumptions underlying the error propagation: We inverted the discrete and linear transients of $d_i$ by minimizing a cost function that assumes them to be subject to normal noise. In the model space, we used $\mathbf{C_e}$ as a covariance matrix to describe the uncertainty of the estimated model parameters

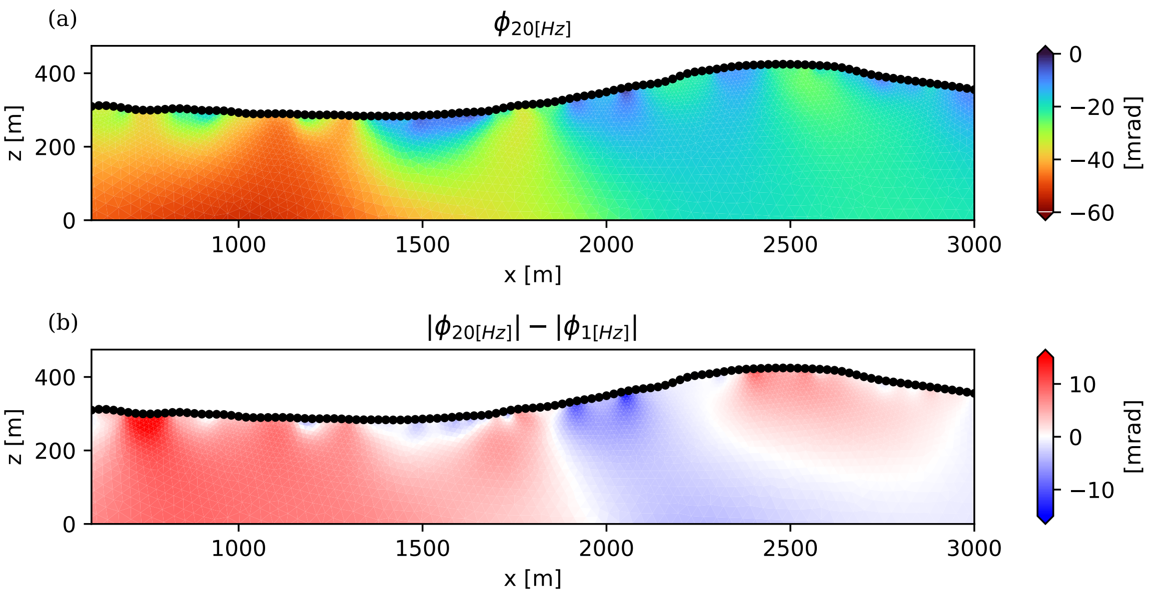

**Figure 3.14:** Comparison of the tomographic inversion results at 20 Hz and 1 Hz. Due to the negligible frequency dependence of the magnitude, only the phase is compared here. **(a)** Phase distribution obtained from the tomographic inversion of spectral data extracted at a frequency of 20 Hz. **(b)** Differences between the phase estimates at 1 Hz and 20 Hz.

$\ln(\gamma_k)$, with $\gamma_k$ and $d_i$ both having the unit of resistance. This is mathematically inexact since $\ln(\gamma_k)$ and $d_i$ cannot both be normally distributed. The same inconsistency arises in the conversion from the model domain to the FD. Still, the presented synthetic validation study suggests that the propagated FD uncertainty is a reasonable estimate that can be used during further processing and tomographic inversions. To account for the uncertainty of the FD error estimate during a tomographic inversion, it is advised to run multiple tomographic inversions with slightly changed error settings to ensure the stability of the features that are being interpreted. Correlations between the errors of $\ln|Z|$ and $\varphi$ can appear as off-diagonal elements in Equation (3.21). These are typically several orders of magnitude smaller than the variances of the parameters. Since the tomographic inversion algorithm we use is unable to account for correlations between $\ln|Z|$ and $\varphi$, we neglected them during the tomographic inversion of the field data set. However, including these correlations in the tomographic inversion improves the consistency of the overall analysis and therefore should be done if possible.

The data set used for the demonstration of the conversion's applicability to tomographic field measurements was obtained using a pole-dipole electrode configuration. For practical reasons, it was unfeasible to perform reciprocal measurements due to the way the measurements were realized in the field. Although electrode configurations like the dipole-dipole make it easier to collect reciprocal measurements in the field, using the pole-dipole configuration provided us with superior IP data quality. Since the conversion approach relies on high-quality transients, we value IP data quality more than the ability to perform reciprocal measurements in this study.

The TD to FD conversion presented in this work is generally independent of the approach that is used for the estimation of the TD error. One can use any method to estimate the TD error that is suitable for the application at hand, for example normal-reciprocal measurements or standard deviations provided by the measurement instrument. We adapted the method described by Flores Orozco et al. (2018b), which came with some benefits that fit well into an adequate pre-processing of the data set prior to the TD to FD conversion. First of all, it does not require a reciprocal data set, which is favorable since a reciprocal data set might not always be available, as in our case for the reasons explained above. Furthermore, the fitted power-law models provided a valuable initial characterization of the data set, on the basis of which a detailed assessment of the data and filtering was possible. Using power-law models as a reference potentially introduces a bias against more complex relaxation behaviors. The first critical point is filtering on the basis of the Pearson correlation coefficient between the measured TD transient and the fitted power-law response. Choosing a threshold value that is too high can result in the exclusion of transients that represent a more complex relaxation behavior. Therefore, a visual inspection of the excluded transients is advisable. Regarding the estimation of the TD error, transient readings with larger deviations from the power-law model result in larger residuals and contribute to larger standard deviation estimates during the bin analysis. This introduces a potential bias, since data sets with many decays that are more complex than what can be described by the power-law model will be assigned larger TD error estimates. The bias is reduced with the use of an error model, since the standard deviation of a specific transient reading $d_i$ is not directly tied to the corresponding residual. Furthermore, we adjusted the fitted error model slightly in order to correct for an overestimation of the error due to the simplicity of the reference transients.

For specific measurement geometries and subsurface scenarios, a negative IP effect can be measured (e.g., Nabighian and Elliot 1976; Dahlin and Loke 2015). The transients associated with this phenomenon take the form of negative decays. Since we used a logarithmic parameterization during the DD, a direct application to negative transients is not possible, as they have to be fitted with values $\gamma_k < 0$. To solve this problem, negative transients must be identified prior to the TD to FD conversion, multiplied by $-1$, and then inverted into an RTD. The FD response can now be calculated according to Equation (3.2), using the estimated values of $\gamma_k$ with a changed sign: $\gamma_k \leftarrow -\gamma_k$. This results in values $Z' > R_0$, $Z'' > 0$ and $\varphi > 0$. The identification of negative transients can be achieved through the information provided by the fit of the reference transients.

We classify our approach as a general-purpose compromise between neglecting the frequency dependence of the phase and using a strong FD parameterization of the subsurface. Both of these extremes can lead to a misrepresentation of the spectral behavior of an unknown target, causing inaccurate tomographic inversion results.

## 3.7 Conclusion

We have introduced a general-purpose approach that can quantitatively convert TD IP data to the FD using Debye decomposition. The conversion approach provides a basis for the analysis of TD IP measurements in the FD. Quantitative relations between geoelectric and petrophysical parameters established for the FD can be used to deduce quantitative information on properties of interest that shape the IP characteristics of the subsurface. Gaussian error propagation was used to propagate a TD error estimate to the FD, thereby providing the uncertainty quantification needed for the inversion of tomographic TD IP measurements in the FD. The implemented algorithm automatically chooses the regularization strength to achieve the appropriate data fit, assuming the existence of a reasonable TD error estimate. We demonstrated the conversion of transients to accurate FD impedance estimates in a synthetic validation study, during which we transformed input signals of varying relaxation time. To validate the assumptions made during the error propagation, we inverted a set of noise realizations and investigated the resulting distributions of all parameters involved during the TD to FD conversion. Based on the scatter of the FD impedance estimates, we calculated reference standard deviations, which we used to investigate the accuracy of the propagated FD error estimates. To demonstrate the practical application of the conversion to field data, we applied it to a tomographic TD IP data set measured in Kamchatka (Russia). The propagated standard deviations of the field data showed systematic behavior expected from previous studies. Inverting the FD data into subsurface models of complex resistivity at frequencies of 1 Hz and 20 Hz showed the ability of the conversion scheme to recover spectral information from tomographic TD IP data sets.

## 3.A Appendix

In this work, we follow the underlying idea of an Occam-type choice of the regularization strength, meaning that we aim to find the simplest model that can fit the measurements within the context of their uncertainties. This choice of regularization strength has been employed for the solution of different types of geophysical inverse problems in the past (e.g., deGroot Hedlin and Constable (1990); LaBrecque et al. (1996); Kemna (2000)). Our algorithm for finding a suitable regularization strength is initialized with a high $\lambda_0$. Performing a pseudo-Newton inversion yields the MAP solution and the optimized step length for $\lambda_0$. Given that $\lambda_0$ is large, the MAP solution should yield RMSE $> 1$, meaning that the measurements should be underfitted. If this is not the case, we abort the algorithm and start with a larger initial regularization strength. In the pseudo-Newton inversions that follow, we reduce the value of $\lambda$ step by step, which leads to a better data fit and smaller RMSE calculated from the responses of the estimated MAP solutions. We update the regularization strength according to

$$\lambda \leftarrow \frac{\lambda}{\mathrm{RMSE} + \xi},$$

where $\xi$ is some non-negative constant. A main exit criterion is implemented, causing a termination of the optimization if the desired data fit is achieved. The closer the optimization gets to the target RMSE $= 1$, the smaller the updates of $\lambda$ become. To increase the stability of the algorithm, we implement a secondary exit criterion that terminates the optimization if an update of $\lambda$ does not lead to a significant update of RMSE. Implementing the secondary exit criterion has been shown to be essential in practice for increasing the stability of the algorithm. Setting $\xi > 0$ avoids interference between excessively small updates of $\lambda$ and the secondary exit criterion. If an update of $\lambda$ causes the inversion to significantly overfit the measurements, we increase $\lambda$ by 10% during the next pseudo-Newton inversion. To ensure consistency in the obtained inversion results, we perform a final improvement of the regularization optimization, during which $\lambda$ is increased by 50% until RMSE starts to increase significantly. In practice, it has been shown that from a found MAP solution with RMSE $\approx 1$, the regularization strength can sometimes be drastically increased while still fitting the measurements well in the context of their respective errors.

# CHAPTER 4

# A probabilistic solution to geophysical inverse problems in complex variables and its application to complex resistivity imaging

## Abstract

We introduce a novel probabilistic framework for the solution of non-linear geophysical inverse problems in complex variables. By using complex probability distributions, this approach can simultaneously account for individual errors of real and imaginary data parts, independently regularize real and imaginary parts of the complex model, and still take into account cross-sensitivities resulting from a complex forward calculation. The inverse problem is solved by means of optimization. An application of the framework to complex resistivity (CR) imaging demonstrates its advantages over the established inversion approach for CR measurements. We show that CR data, with real and imaginary parts being subject to different errors, can be fitted adequately, accounting for the individual errors and applying independent regularization to the real and imaginary part of the subsurface conductivity. The probabilistic framework itself serves as a basis for the future application of global sampling approaches, such as Markov chain Monte Carlo methods.

This chapter was published as:

Hase, J., Weigand, M., & Kemna, A. (2024). A probabilistic solution to geophysical inverse problems in complex variables and its application to complex resistivity imaging. *Geophysical Journal International, 237*(1), 456-464. https://doi.org/10.1093/gji/ggae045

## 4.1 Introduction

We introduce a probabilistic framework for the solution of geophysical inverse problems in complex variables. Within the framework, data and model parameters are treated explicitly as complex random variables and we use Bayes' theorem to combine the complex probability distributions associated with likelihood and model prior into a posterior distribution for the complex model. The probabilistic formulation of the inverse problem using Bayes' theorem inherently accounts for data errors and uncertainties in the prior assumptions, both of which are propagated naturally into the solution (e.g., Bayes 1763; Sen and Stoffa 1996; Tarantola 2005). Sampling strategies, such as Markov chain Monte Carlo (McMC) methods, can be employed to numerically approximate statistical estimators of interest over the posterior distribution and to explore ambiguities in the solution (e.g., Sambridge and Mosegaard 2002). Applications of this concept to geophysical inverse problems in real variables can be found in many different fields of geophysics (e.g., Sen and Stoffa 1996; De Pasquale et al. 2019; Fichtner et al. 2019; Deng et al. 2022). However, to our knowledge, the concept has not yet been extended to geophysical inverse problems in complex variables. The application of McMC strategies to the general geoelectric imaging problem is still challenging, mainly due to the computational cost of evaluating the forward response. Because of this, we exclusively focus on the estimation of the maximum a posteriori (MAP) solution by means of Gauss-Newton optimization and leave the adaptation of sampling strategies to the introduced probabilistic framework open to future research. The considerations with regard to complex differentiability, necessary for the application of Gauss-Newton optimization, provide a basis for the application of gradient-guided McMC methods, such as Hamiltonian Monte Carlo (e.g., Neal et al. 2011; Fichtner et al. 2019).

The complex resistivity (CR) method targets the distribution of the complex electrical conductivity within the subsurface, capturing the conduction and polarization properties under the application of an alternating current at a given frequency. In CR surveys, the induced polarization response of the subsurface is measured and analyzed in terms of the frequency-dependent complex electrical impedance (e.g., Van Voorhis et al. 1973; Pelton et al. 1978). Previous studies have inverted tomographic data sets of induced polarization measurements into subsurface models, using various approaches and parameterizations (e.g., Weller et al. 1996a; Martin and Günther 2013; Johnson and Thomle 2018). Kemna (2000) introduced the first fully complex framework for the inversion of complex impedance measurements into subsurface images of conductivity magnitude and phase, which has been used in various applications (e.g., Kemna et al. 2004; Williams et al. 2009; Flores Orozco et al. 2011; 2012b; Weigand and Kemna 2017; Maierhofer et al. 2022). The inversion is based on a weighted-least squares (WLSQ) framework, using the Hermitian norm, in which data and model are both explicitly treated as complex variables. However, the WLSQ framework is not able to ensure that the model found by means of optimization appropriately fits the real and imaginary parts of the data in the context of their individual error estimates, which are often available from the data acquisition process. The reason for this is the inability of the WLSQ scheme to account for the error estimates of the complex data's real and imaginary parts individually. Another disadvantage of the scheme can be that the model regularization cannot be independently adjusted for real and imaginary parts, which may be detrimental if subsurface conductivity and polarizability are known to exhibit different spatial characteristics. By individually accounting for the error estimates of the real and imaginary part of the complex data, as well as by controlling the prior assumptions applied to the real and imaginary part of the complex model independently, an adequate fit of the complex data can be reached in a complex inversion, using the probabilistic framework introduced in this work. For the application to CR imaging, we discuss explicitly how the probabilistic framework relates to the established WLSQ framework, as well as to the approach recently presented by Wang et al. (2023). Our implementation of the probabilistic framework for the inversion of CR measurements uses the forward modeling and inversion capabilities provided by the open-source software package pyGIMLi (Rücker et al. 2017).

The remainder of this follows: We introduce the probability distributions underlying the probabilistic framework and discuss simplifications, followed by a description of the Gauss-Newton approach that is used to solve the inverse problem by means of optimization. After that, we provide a short introduction into CR measurements and the established WLSQ inversion approach to invert them, which is used as a reference. Different aspects of the probabilistic framework are then demonstrated on synthetic examples. Finally, we discuss and conclude our results.

## 4.2 A probabilistic solution to geophysical inverse problems in complex variables

The goal of geophysical inversion in complex variables is to recover a subsurface model $\tilde{\mathbf{m}} \in \mathbb{C}^M$ from a set of data $\tilde{\mathbf{d}} \in \mathbb{C}^N$, given the forward operator $\tilde{\mathbf{f}}(\tilde{\mathbf{m}})$, as well as uncertainty estimates for the data and prior assumptions on the spatial characteristics of the subsurface. The appropriate formulation of the underlying probability distributions in terms of complex random variables demands usage of the conjugate coordinate representation of complex vectors (e.g., Kreutz-Delgado 2009). For the complex vector $\tilde{\mathbf{x}} \in \mathbb{C}^M$ we define $\overset{c}{\mathbf{x}} \triangleq (\tilde{\mathbf{x}}, \tilde{\mathbf{x}}^*)^T \in \mathbb{C}^{2M}$ to be its representation in conjugate coordinates, with $^*$ denoting the complex conjugation and $^T$ denoting the transpose. The representation in conjugate coordinates is related to the representation of $\tilde{\mathbf{x}}$ in terms of its real and imaginary part $\overset{r}{\mathbf{x}} \triangleq (\mathbf{x}', \mathbf{x}'')^T \in \mathbb{R}^{2M}$ by the linear transformations[1]

$$\overset{c}{\mathbf{x}} = \underbrace{\begin{bmatrix} \mathbf{I} & i\mathbf{I} \\ \mathbf{I} & -i\mathbf{I} \end{bmatrix}}_{\tilde{\mathbf{S}}} \overset{r}{\mathbf{x}} \tag{4.1}$$

and

$$\overset{r}{\mathbf{x}} = \tilde{\mathbf{S}}^{-1} \overset{c}{\mathbf{x}} = \frac{1}{2} \tilde{\mathbf{S}}^H \overset{c}{\mathbf{x}}, \tag{4.2}$$

---

[1] Please note that the definition of $\tilde{\mathbf{S}}$ as it is given here is the same as in the publication of this chapter. In Chapter 5, the definition of $\tilde{\mathbf{S}}$ is changed slightly, in order to achieve $\tilde{\mathbf{S}}^H = \tilde{\mathbf{S}}^{-1}$. All equations in Chapters 4 and 5 are consistent with the definition of $\tilde{\mathbf{S}}$ given in the respective chapter.

with $^H$ denoting the conjugate transpose, $\mathbf{I}$ denoting the identity matrix and $i^2 = -1$. The probabilistic inversion framework described in this work is built upon Bayes' theorem (Bayes 1763):

$$p(\overset{c}{\mathbf{m}} \mid \overset{c}{\mathbf{d}}) \propto p(\overset{c}{\mathbf{d}} \mid \overset{c}{\mathbf{m}}) \, p(\overset{c}{\mathbf{m}}). \tag{4.3}$$

The likelihood term $p(\overset{c}{\mathbf{d}} \mid \overset{c}{\mathbf{m}})$ is combined with the prior term $p(\overset{c}{\mathbf{m}})$ into the posterior distribution $p(\overset{c}{\mathbf{m}} \mid \overset{c}{\mathbf{d}})$, which assigns a conditional probability to a model realization $\overset{c}{\mathbf{m}}$, given the data $\overset{c}{\mathbf{d}}$. In order to correctly describe data and model as complex random variables, Equation (4.3) features their representation in terms of conjugate coordinates.

Using the linear operator $\tilde{\mathbf{S}}$, it is theoretically possible to find an equivalent framework to the one described in this work using a real-valued parameterization of model and data, as described by Wang et al. (2023) for the inversion of CR measurements. However, formulating the inverse problem in terms of complex random variables is sensible if the mathematical description of the physical phenomenon underlying the measurements involves complex-valued parameters. Furthermore, in case of CR measurements, using a complex formulation illustrates how the probabilistic framework introduced in this work relates to the established complex inversion framework by Kemna (2000). We realize that a complex-valued model parameterization can have implications with regard to the use of generalized optimization packages. Although Wang et al. (2023) use a real-valued parameterization for the inversion, the forward calculation is nonetheless carried out using complex variables and the real and imaginary parts of the complex model response and complex sensitivity are extracted from the complex-valued results. While there might be benefits for specific applications, we do not see general advantages or disadvantages for either of the two approaches in terms of implementation.

### 4.2.1 Likelihood term

The model and data spaces are linked by the likelihood term. It describes the conditional probability of the data, given a certain model realization. If the errors of the complex data are assumed to be normal, we can formulate the likelihood as the following complex normal distribution (Picinbono 1996):

$$p(\overset{c}{\mathbf{d}} \mid \overset{c}{\mathbf{m}}) \propto \exp \left[ -\frac{1}{2} \left[ (\tilde{\mathbf{d}} - \tilde{\mathbf{f}}(\tilde{\mathbf{m}}))^H, (\tilde{\mathbf{d}} - \tilde{\mathbf{f}}(\tilde{\mathbf{m}}))^T \right] \underbrace{\begin{pmatrix} \tilde{\mathbf{C}}_{\mathbf{d}} & \tilde{\mathbf{\Gamma}}_{\mathbf{d}} \\ \tilde{\mathbf{\Gamma}}_{\mathbf{d}}^H & \tilde{\mathbf{C}}_{\mathbf{d}}^* \end{pmatrix}^{-1}}_{=\overset{c}{\mathbf{R}}_{\mathbf{d}}} \begin{pmatrix} \tilde{\mathbf{d}} - \tilde{\mathbf{f}}(\tilde{\mathbf{m}}) \\ (\tilde{\mathbf{d}} - \tilde{\mathbf{f}}(\tilde{\mathbf{m}}))^* \end{pmatrix} \right]. \tag{4.4}$$

Equation (4.4) maps $N$ complex data points and their complex conjugates to a real-valued probability. The matrices $\tilde{\mathbf{C}}_{\mathbf{d}}$ and $\tilde{\mathbf{\Gamma}}_{\mathbf{d}}$ capture the second-order properties of the complex normal distribution (4.4). Assuming error estimates for $\mathbf{d}'$ and $\mathbf{d}''$, we find the complex covariance matrix (Picinbono 1996):

$$\begin{pmatrix} \tilde{\mathbf{C}}_{\mathbf{d}} & \tilde{\mathbf{\Gamma}}_{\mathbf{d}} \\ \tilde{\mathbf{\Gamma}}_{\mathbf{d}}^{H} & \tilde{\mathbf{C}}_{\mathbf{d}}^{*} \end{pmatrix} = 2\,\tilde{\mathbf{S}} \begin{pmatrix} \mathrm{Cov}(\mathbf{d}',\mathbf{d}') & \mathrm{Cov}(\mathbf{d}',\mathbf{d}'') \\ \mathrm{Cov}(\mathbf{d}'',\mathbf{d}') & \mathrm{Cov}(\mathbf{d}'',\mathbf{d}'') \end{pmatrix} \tilde{\mathbf{S}}^{-1}. \tag{4.5}$$

Explicitly, $\tilde{\mathbf{C}}_{\mathbf{d}}$ and $\tilde{\mathbf{\Gamma}}_{\mathbf{d}}$ can be calculated according to:

$$\tilde{\mathbf{C}}_{\mathbf{d}} = \mathrm{Cov}(\mathbf{d}',\mathbf{d}') + \mathrm{Cov}(\mathbf{d}'',\mathbf{d}'') + i\left(\mathrm{Cov}(\mathbf{d}'',\mathbf{d}') - \mathrm{Cov}(\mathbf{d}',\mathbf{d}'')\right), \tag{4.6}$$

$$\tilde{\mathbf{\Gamma}}_{\mathbf{d}} = \mathrm{Cov}(\mathbf{d}',\mathbf{d}') - \mathrm{Cov}(\mathbf{d}'',\mathbf{d}'') + i\left(\mathrm{Cov}(\mathbf{d}'',\mathbf{d}') + \mathrm{Cov}(\mathbf{d}',\mathbf{d}'')\right). \tag{4.7}$$

A first simplification can be derived if the error estimates of $\mathbf{d}'$ and $\mathbf{d}''$ are uncorrelated:

$$\mathrm{Cov}(\mathbf{d}'',\mathbf{d}') = \mathrm{Cov}(\mathbf{d}',\mathbf{d}'') = \mathbf{0}, \tag{4.8}$$

leading to $\tilde{\mathbf{C}}_{\mathbf{d}} = \mathbf{C}'_{\mathbf{d}}$ and $\tilde{\mathbf{\Gamma}}_{\mathbf{d}} = \mathbf{\Gamma}'_{\mathbf{d}}$. Furthermore, if the error estimates of $\mathbf{d}'$ and $\mathbf{d}''$ are equal, we find:

$$\tilde{\mathbf{\Gamma}}_{\mathbf{d}} = \mathrm{Cov}(\mathbf{d}',\mathbf{d}') - \mathrm{Cov}(\mathbf{d}'',\mathbf{d}'') = \mathbf{0}. \tag{4.9}$$

Given these two simplifications, Equation (4.4) reduces to

$$p(\tilde{\mathbf{d}}|\tilde{\mathbf{m}}) \propto \exp\left[-(\tilde{\mathbf{d}} - \tilde{\mathbf{f}}(\tilde{\mathbf{m}}))^{H}\tilde{\mathbf{C}}_{\mathbf{d}}^{-1}(\tilde{\mathbf{d}} - \tilde{\mathbf{f}}(\tilde{\mathbf{m}}))\right]. \tag{4.10}$$

### 4.2.2 Prior term

We adapt the above concept to formulate the prior term, apply independent regularization to $\mathbf{m}'$ and $\mathbf{m}''$, using the symmetric real operators $\mathbf{R}_{\Re,\Im} = \lambda_{\Re,\Im}\left(\mathbf{W}_{\mathbf{m}}^{T}\mathbf{W}_{\mathbf{m}}\right)_{\Re,\Im}$, with regularization strengths $\lambda_{\Re}$ and $\lambda_{\Im}$, and find the following expression:

$$p(\overset{c}{\mathbf{m}}) \propto \exp\left[-\frac{1}{2}\left[(\tilde{\mathbf{m}}-\tilde{\mathbf{m}}_p)^{H},(\tilde{\mathbf{m}}-\tilde{\mathbf{m}}_p)^{T}\right] \underbrace{\begin{pmatrix} \mathbf{R}_{\Re}+\mathbf{R}_{\Im} & \mathbf{R}_{\Re}-\mathbf{R}_{\Im} \\ \mathbf{R}_{\Re}-\mathbf{R}_{\Im} & \mathbf{R}_{\Re}+\mathbf{R}_{\Im} \end{pmatrix}}_{=\overset{c}{\mathbf{R}}_{\mathbf{m}}} \begin{pmatrix} \tilde{\mathbf{m}}-\tilde{\mathbf{m}}_p \\ (\tilde{\mathbf{m}}-\tilde{\mathbf{m}}_p)^{*} \end{pmatrix}\right], \tag{4.11}$$

with the prior model $\tilde{\mathbf{m}}_p \in \mathbb{C}^{M}$. Here, the inverse prior covariance matrix can be calculated according to

$$\overset{c}{\mathbf{R}}_{\mathbf{m}} = 2\,\tilde{\mathbf{S}} \begin{pmatrix} \mathbf{R}_{\Re} & \mathbf{0} \\ \mathbf{0} & \mathbf{R}_{\Im} \end{pmatrix} \tilde{\mathbf{S}}^{-1}. \tag{4.12}$$

The matrices $\mathbf{R}_{\Re}$ and $\mathbf{R}_{\Im}$ can exhibit different regularization characteristics. Setting $\mathbf{R}_{\Re} = \mathbf{R}_{\Im} = \mathbf{R}$ leads to

$$p(\tilde{\mathbf{m}}) \propto \exp\left[-(\tilde{\mathbf{m}}-\tilde{\mathbf{m}}_p)^{H}\mathbf{R}(\tilde{\mathbf{m}}-\tilde{\mathbf{m}}_p)\right], \tag{4.13}$$

applying equal regularization to $\mathbf{m}'$ and $\mathbf{m}''$.

### 4.2.3 Optimization of the posterior distribution

We find the MAP model by maximizing Equation (4.3), which can be achieved by minimizing the corresponding cost function

$$\Psi(\overset{c}{\mathbf{m}}) = -\ln\left(p(\overset{c}{\mathbf{m}} \mid \overset{c}{\mathbf{d}})\right). \tag{4.14}$$

Minimizing a cost function that maps a complex variable to a real-valued output is non-trivial, because such a cost function does not fulfill the Cauchy-Riemann equations and is therefore not complex differentiable. However, formulating the complex model vector in terms of conjugate coordinates allows us to exploit the differentiability of the cost function with respect to input from $\mathbb{R}^{2M}$. Due to the non-linear character of the forward operator $\tilde{\mathbf{f}}(\tilde{\mathbf{m}})$, Equation (4.14) has to be minimized iteratively. Sorber et al. (2012) formulate a generalized Gauss-Newton scheme for the solution of the minimization problem

$$\min_{\tilde{\mathbf{x}}} || \tilde{\mathbf{F}}(\tilde{\mathbf{x}}, \tilde{\mathbf{x}}^*) ||^2. \tag{4.15}$$

Around a given model state $\overset{c}{\mathbf{x}}_q$, they approximate the non-linear function $\tilde{\mathbf{F}}(\tilde{\mathbf{x}}, \tilde{\mathbf{x}}^*)$ using the first-order Taylor polynomial

$$\mathbf{t}_q^F\left(\Delta \overset{c}{\mathbf{x}}_q\right) = \tilde{\mathbf{F}}\left(\overset{c}{\mathbf{x}}_q\right) + \frac{\partial \tilde{\mathbf{F}}\left(\overset{c}{\mathbf{x}}_q\right)}{\partial \overset{c}{\mathbf{x}}^T} \Delta \overset{c}{\mathbf{x}}_q, \tag{4.16}$$

yielding the approximation $\mathbf{t}_q^f$ of the objective function (4.15):

$$\mathbf{t}_q^f\left(\Delta \overset{c}{\mathbf{x}}_q\right) = \frac{1}{2} \left|\left| \mathbf{t}_q^F\left(\Delta \overset{c}{\mathbf{x}}_q\right) \right|\right|^2. \tag{4.17}$$

Here, the derivative operator with respect to the complex model in conjugate coordinates is given by

$$\frac{\partial}{\partial \overset{c}{\mathbf{x}}} = \left(\frac{\partial}{\partial \tilde{\mathbf{x}}}, \frac{\partial}{\partial \tilde{\mathbf{x}}^*}\right). \tag{4.18}$$

Explicitly, they find

$$\mathbf{t}_q^f\left(\Delta \overset{c}{\mathbf{x}}_q\right) = \frac{1}{2} || \tilde{\mathbf{F}}_q ||^2 + \frac{1}{2} \Delta \overset{c}{\mathbf{x}}^T \begin{bmatrix} \tilde{\mathbf{J}}_q \mathbf{Q} \\ \tilde{\mathbf{J}}_q^* \end{bmatrix}^H \begin{bmatrix} \tilde{\mathbf{F}}_q \\ \tilde{\mathbf{F}}_q^* \end{bmatrix} + \frac{1}{2} \Delta \overset{c}{\mathbf{x}}^H \tilde{\mathbf{J}}_q^H \tilde{\mathbf{J}}_q \Delta \overset{c}{\mathbf{x}}, \tag{4.19}$$

for the quadratic approximation of the objective function around $\overset{c}{\mathbf{x}}_q$, with $\tilde{\mathbf{J}}_q = \frac{\partial \tilde{\mathbf{F}}\left(\overset{c}{\mathbf{x}}_q\right)}{\partial \overset{c}{\mathbf{x}}^T}$, $\tilde{\mathbf{F}}_q = \tilde{\mathbf{F}}\left(\overset{c}{\mathbf{x}}_q\right)$ and

$$\mathbf{Q} = \begin{bmatrix} 0 & \mathbf{I} \\ \mathbf{I} & 0 \end{bmatrix}, \tag{4.20}$$

so that $(\tilde{\mathbf{x}}, \tilde{\mathbf{x}}^*)^T = \mathbf{Q}\,(\tilde{\mathbf{x}}^*, \tilde{\mathbf{x}})^T$. Setting the derivative with respect to $\Delta \overset{c^*}{\mathbf{x}}$ equal to $\mathbf{0}$ yields the condition for the local minimum:

$$\frac{\partial \mathbf{t}_q^f\left(\Delta \overset{c}{\mathbf{x}}_q\right)}{\partial \Delta \overset{c^*}{\mathbf{x}}} = \frac{1}{2}\begin{bmatrix} \tilde{\mathbf{J}}_q \\ \tilde{\mathbf{J}}_q^*\mathbf{Q} \end{bmatrix}^H \begin{bmatrix} \tilde{\mathbf{F}}_q \\ \tilde{\mathbf{F}}_q^* \end{bmatrix} + \frac{1}{2}\begin{bmatrix} \tilde{\mathbf{J}}_q \\ \tilde{\mathbf{J}}_q^*\mathbf{Q} \end{bmatrix}^H \begin{bmatrix} \tilde{\mathbf{J}}_q \\ \tilde{\mathbf{J}}_q^*\mathbf{Q} \end{bmatrix} \Delta \overset{c}{\mathbf{x}}_q \overset{!}{=} \mathbf{0}. \tag{4.21}$$

In the condition for the local minimum (4.21), we can identify the terms corresponding to the normal equations associated with the iterative minimization of Equation (4.14):

$$\overset{c}{\mathbf{B}}_q \,\Delta\, \overset{c}{\mathbf{m}}_q = \overset{c}{\mathbf{b}}_q \tag{4.22}$$

$$\overset{c}{\mathbf{B}}_q = \left( \begin{bmatrix} \tilde{\mathbf{G}}_q & \tilde{\mathbf{\Xi}}_q \\ \tilde{\mathbf{\Xi}}_q^* & \tilde{\mathbf{G}}_q^* \end{bmatrix}^H \overset{c}{\mathbf{R}}_{\mathbf{d}} \begin{bmatrix} \tilde{\mathbf{G}}_q & \tilde{\mathbf{\Xi}}_q \\ \tilde{\mathbf{\Xi}}_q^* & \tilde{\mathbf{G}}_q^* \end{bmatrix} + \overset{c}{\mathbf{R}}_{\mathbf{m}} \right) \tag{4.23}$$

$$\overset{c}{\mathbf{b}}_q = \left( \underbrace{\begin{bmatrix} \tilde{\mathbf{G}}_q & \tilde{\mathbf{\Xi}}_q \\ \tilde{\mathbf{\Xi}}_q^* & \tilde{\mathbf{G}}_q^* \end{bmatrix}^H}_{=\overset{c}{\mathbf{G}}_q} \overset{c}{\mathbf{R}}_{\mathbf{d}} \begin{pmatrix} \tilde{\mathbf{d}} - \tilde{\mathbf{f}}(\tilde{\mathbf{m}}_q) \\ \left(\tilde{\mathbf{d}} - \tilde{\mathbf{f}}(\tilde{\mathbf{m}}_q)\right)^* \end{pmatrix} - \overset{c}{\mathbf{R}}_{\mathbf{m}} \begin{pmatrix} \tilde{\mathbf{m}}_q - \tilde{\mathbf{m}}_p \\ (\tilde{\mathbf{m}}_q - \tilde{\mathbf{m}}_p)^* \end{pmatrix} \right), \tag{4.24}$$

with

$$\tilde{G}_{ik} = \frac{\partial \tilde{f}_i}{\partial \tilde{m}_k}, \tag{4.25}$$

holding the partial derivatives of the forward operator with respect to the complex model, and

$$\tilde{\Xi}_{ik} = \frac{\partial \tilde{f}_i}{\partial \tilde{m}_k^*}, \tag{4.26}$$

holding the partial derivatives of the forward operator with respect to the complex conjugate of the complex model. If the forward operator is complex differentiable, as it is in case of the CR problem (Kemna 2000), the Cauchy-Riemann equations demand $\tilde{\mathbf{\Xi}} = \mathbf{0}$. In that case, the imaginary part of $\tilde{G}_{ik}$ holds the cross-sensitivities:

$$\frac{\partial f_i'}{\partial m_k''} = -\frac{\partial f_i''}{\partial m_k'}. \tag{4.27}$$

## 4.3 Application to complex resistivity imaging

In CR imaging, forward modeling of the complex electric potential $\tilde{\psi}$, resulting for a given model realization and current source, is conducted by solving the Poisson equation at a given angular frequency $\omega$:

$$\nabla \cdot \left(\tilde{\sigma}(\omega)\nabla\tilde{\psi}(\omega)\right) - \nabla \cdot \tilde{\mathbf{J}}_s(\omega) = 0, \tag{4.28}$$

with the source current density $\tilde{\mathbf{J}}_s$ and the complex electrical conductivity $\tilde{\sigma}$. This can be achieved, for example, by using the finite-difference method (e.g., Weller et al. 1996a), or the finite-element method (e.g., Kemna 2000). The complex electrical impedance $\tilde{Z}$ is obtained as the ratio of the measured potential difference to the injected current. Kemna (2000) introduced the complex inversion of CR measurements into subsurface images of complex conductivity, explicitly treating data and model as complex variables. In this work, we adopt his transformation of the data and parameterization of the model. A set of $N$ complex data

$$\tilde{d}_i = -\ln|\tilde{Z}_i| + i\varphi_i, \tag{4.29}$$

with the complex electrical impedance $\tilde{Z}_i$ and negative phase of the complex electrical impedance $\varphi_i$, is inverted into a subsurface model that features $M$ parameters. The geometric factor $k_i$ relates the complex electrical impedance to the apparent complex conductivity

$$\tilde{\sigma}_{a_i} = \frac{1}{k_i\tilde{Z}_i}, \tag{4.30}$$

which we use for the visual display of CR data in pseudosections. The model is formulated as the complex logarithm of the complex electrical conductivity:

$$\tilde{m}_k = \ln(\tilde{\sigma}_k) = \ln|\tilde{\sigma}_k| + i\phi_k, \tag{4.31}$$

with the phase of the complex electrical conductivity $\phi_k$. For reasons of readability, we refer to the real and imaginary parts of the complex data $\tilde{d}_i$ as the *impedance magnitude* and *impedance phase*, since these are the parts of the measured complex electrical impedance $\tilde{Z}$ they represent. Consistently, we refer to the real and imaginary part of the complex model $\tilde{m}_k$ as *conductivity magnitude* and *conductivity phase*, since they represent the magnitude and phase of the imaged complex electrical conductivity $\tilde{\sigma}$.

Kemna (2000) solves the CR inverse problem by minimizing the cost function

$$\Psi(\tilde{\mathbf{m}}) = (\tilde{\mathbf{d}} - \tilde{\mathbf{f}}(\tilde{\mathbf{m}}))^H \tilde{\mathbf{W}}_{\mathbf{d}}^H \tilde{\mathbf{W}}_{\mathbf{d}} (\tilde{\mathbf{d}} - \tilde{\mathbf{f}}(\tilde{\mathbf{m}})) + \lambda(\tilde{\mathbf{m}} - \tilde{\mathbf{m}}_p)^H \mathbf{W}_{\mathbf{m}}^T \mathbf{W}_{\mathbf{m}} (\tilde{\mathbf{m}} - \tilde{\mathbf{m}}_p), \tag{4.32}$$

with $\tilde{\mathbf{C}}_{\mathbf{d}}^{-1} = \tilde{\mathbf{W}}_{\mathbf{d}}^H \tilde{\mathbf{W}}_{\mathbf{d}}$ and $\mathbf{R} = \lambda \mathbf{W}_{\mathbf{m}}^T \mathbf{W}_{\mathbf{m}}$. The data weighting matrix $\tilde{\mathbf{W}}_{\mathbf{d}}$ holds the inverses of the complex data errors

$$\tilde{e}_i = \mathrm{std}(\ln|\tilde{Z}_i|) + i\,\mathrm{std}(\varphi_i) \tag{4.33}$$

as diagonal elements. Since equal weight is applied to the real and imaginary part of the complex residual $(\tilde{\mathbf{d}} - \tilde{\mathbf{f}}(\tilde{\mathbf{m}}))$, this WLSQ framework implicitly assumes equal error estimates for impedance magnitude and phase. Furthermore, the same regularization strength is applied to the conductivity magnitude and phase. If we interpret Equation (4.32) from a probabilistic point of view, the data misfit term corresponds to the simplified likelihood term in Equation (4.10) and the regularization term corresponds to the simplified prior term in Equation (4.13). It is not guaranteed that a model minimizing Equation (4.32) achieves appropriate individual data fits for impedance magnitude and phase. Kemna (2000) overcomes this problem by refining the conductivity phase independently, after a solution for the conductivity magnitude has been found. During this final phase improvement, the conductivity magnitude is kept fixed and changes in the data fit of the impedance magnitude caused by cross-sensitivities are effectively disregarded, introducing inconsistencies with regard to the estimation of the MAP solution. Wang et al. (2023) provide a detailed comparison of the WLSQ inversion with final phase improvement to other CR inversion approaches. In the synthetic studies that follow, we use inversion results obtained from the minimization of Equation (4.32) as a reference, without a subsequent refinement of the conductivity phase, since we want to stay consistent during our comparison of the WLSQ framework and the probabilistic framework.

The two measured quantities $\ln|\tilde{Z}_i|$ and $\varphi_i$ are assumed to be subject to normally distributed noise. For the impedance magnitude, the typically used error model is linear in $|\tilde{Z}_i|$ (e.g., LaBrecque et al. 1996):

$$\mathrm{std}(|\tilde{Z}_i|) = a|\tilde{Z}_i| + b. \tag{4.34}$$

The standard deviation of the impedance phase is assumed to be constant in some studies (e.g., Kemna 2000), or is assumed to follow an inverse power law (e.g., Flores Orozco et al. 2012b)

$$\mathrm{std}(\varphi_i) = a|\tilde{Z}_i|^{-b} + c, \tag{4.35}$$

extended by an absolute error $c$. There is no inherent condition that suggests for the error estimates of impedance magnitude and phase to be of similar size. To quantify how well a model response fits the complex data, we use two different formulations of the root-mean square error (RMSE):

$$\mathrm{RMSE}_{real} = \sqrt{\frac{1}{N}\left(\mathbf{d}' - \mathbf{f}(\tilde{\mathbf{m}})'\right)^T \mathrm{Cov}(\mathbf{d}',\mathbf{d}')^{-1} \left(\mathbf{d}' - \mathbf{f}(\tilde{\mathbf{m}})'\right)}, \tag{4.36}$$

$$\mathrm{RMSE}_{imag} = \sqrt{\frac{1}{N}\left(\mathbf{d}'' - \mathbf{f}(\tilde{\mathbf{m}})''\right)^T \mathrm{Cov}(\mathbf{d}'',\mathbf{d}'')^{-1} \left(\mathbf{d}'' - \mathbf{f}(\tilde{\mathbf{m}})''\right)}, \tag{4.37}$$

to isolate the data fits with regard to the impedance magnitude and phase.

### 4.3.1 Example I.: Independent impedance magnitude and phase error estimates

First, we investigate the probabilistic framework's ability to account for differences in the error estimates of impedance magnitude and phase. Figure 4.1 shows the true model over which a dipole-dipole survey was simulated to generate synthetic data. Using the error models given in Equations (4.34) and (4.35), synthetic noise was generated and added to the data set. For the error model of the impedance magnitude (4.34) we used $a = 0.1$ and $b = 10^{-6}\,\Omega$, while for the error model of the impedance phase (4.35) we used $a = 10^{-7}$, $b = 0.9$ and $c = 10^{-4}\,\mathrm{rad}$. Figure 4.1 shows the pseudosections of the impedance magnitude and phase, as well as the distributions of the standard deviations associated with the synthetic data. No correlations were assumed between the impedance magnitude and phase errors, as well as between errors of different data points. The impedance magnitude error estimates are significantly larger than the impedance phase error estimates. As this situation strongly violates the implicit assumption underlying Equation (4.32), we expect that an inversion using the WLSQ framework is not able to reach an adequate data fit for both impedance magnitude and phase. For demonstration purposes we here compare the results of two inversions. First, we inverted the synthetic data using the WLSQ framework. For this we set

$$\tilde{C}_{\mathbf{d},ii} = \mathrm{std}(\ln(|\tilde{Z}_i|))^2 + \mathrm{std}(\varphi_i)^2, \tag{4.38}$$

and

$$\tilde{\mathbf{\Gamma}}_{\mathbf{d}} = \mathbf{0}, \tag{4.39}$$

which implies equal error estimates for impedance magnitude and phase. The regularization strength $\lambda$, applied equally to the conductivity magnitude and phase, was fixed. Second, we inverted the synthetic data using the probabilistic framework. During this inversion, we included the error estimates of the impedance magnitude and phase appropriately in the complex data covariance matrix (4.5). For regularization, we fixed the individual values of $\lambda_{\Re}$ and $\lambda_{\Im}$ so that the obtained inversion result achieves a good data fit. Both inversions were performed on the same mesh using second-order smoothing between neighboring cells, with a prior model $\tilde{\mathbf{m}}_p = \mathbf{0}$.

Figure 4.2 shows the inversion results obtained from the WLSQ framework and the probabilistic framework, respectively. Both inversion frameworks are able to fit the impedance magnitudes well, with RMSE$_{real}$ values of 1.02 for the probabilistic framework and 1.01 for the WLSQ framework. Differences between the two inversion results occur for the data fit of the impedance phases. As indicated by the values of RMSE$_{imag}$, the probabilistic framework reaches the target data fit of 1.0, while the WLSQ framework under-fits the impedance phases significantly, only reaching a RMSE$_{imag}$ of 7.45. For the WLSQ framework, choosing a smaller value for $\lambda$ would improve the data fit of the impedance phase. However, this would cause an over-fitting of the impedance magnitude. Both approaches recover the synthetic model's magnitude equally well. For the conductivity phase, the probabilistic framework achieves a superior result.

For both inversion results, we approximated the posterior covariance matrix under the assumption of normally distributed model parameters near the MAP solution. We isolated the variances of the conductivity magnitude and phase according to (Picinbono 1996; Tarantola 2005):

$$\begin{pmatrix} \mathrm{Cov}\left(\mathbf{m}', \mathbf{m}'\right) & \mathrm{Cov}\left(\mathbf{m}', \mathbf{m}''\right) \\ \mathrm{Cov}\left(\mathbf{m}'', \mathbf{m}'\right) & \mathrm{Cov}\left(\mathbf{m}'', \mathbf{m}''\right) \end{pmatrix} = \frac{1}{2}\tilde{\mathbf{S}}^{-1}\left(\overset{c}{\mathbf{G}}{}^{H}_{MAP}\overset{c}{\mathbf{R}}_{\mathbf{d}}\overset{c}{\mathbf{G}}_{MAP} + \overset{c}{\mathbf{R}}_{\mathbf{m}}\right)^{-1}\tilde{\mathbf{S}}. \tag{4.40}$$

The estimated variances are displayed in Figure 4.3. The conductivity magnitude and phase images obtained from the inversion with the probabilistic framework are subject to different variances, with the conductivity phase showing a significantly smaller uncertainty than the conductivity magnitude (compare Figure 4.3c and d). In contrast to this, the WLSQ framework implies equal error estimates for the impedance magnitude and phase in the likelihood term and equal regularization acting on the conductivity magnitude and phase in the prior

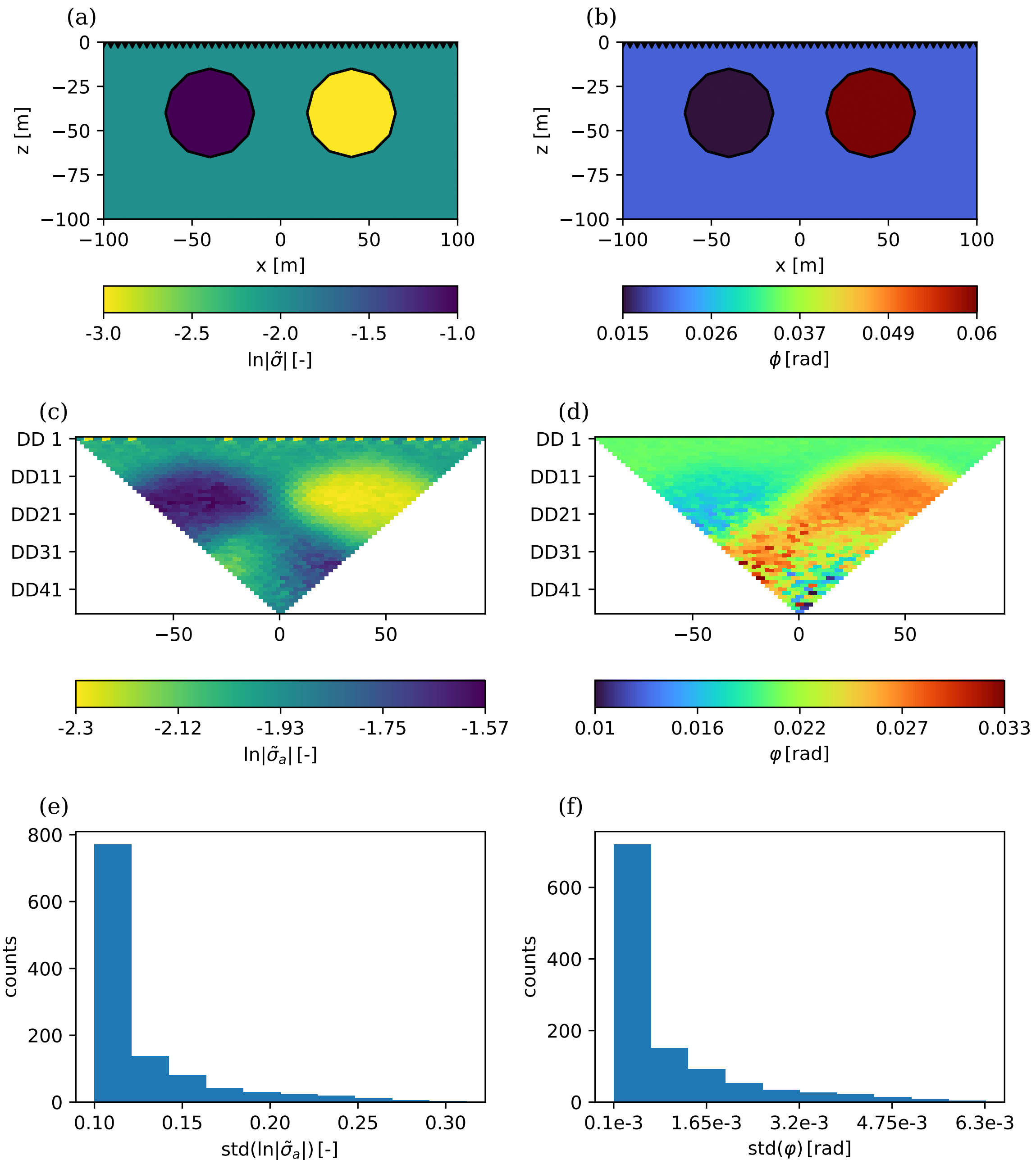

**Figure 4.1:** Conductivity magnitude **(a)** and phase **(b)** of the synthetic model and resultant impedance magnitude **(c)** and phase **(d)** pseudosections for a dipole-dipole measurement scheme (with pseudo-depth levels on vertical axis), subject to the noise shown in **(e, f)**.

term. This propagates into the posterior covariance matrix of the inversion result, causing equal variance estimates for the conductivity magnitude and phase (compare Figure 4.3a,b and e). The sum of the variances $\mathrm{Var}(\ln|\tilde{\sigma}|)$ and $\mathrm{Var}(\phi)$ is equal for both inversion frameworks (compare Figure 4.3f). While $\mathrm{Var}(\phi)$ is smaller for the probabilistic framework, implying that interpretations on the basis of the conductivity phase obtained by the WLSQ framework might be too conservative, $\mathrm{Var}(\ln|\tilde{\sigma}|)$ is in fact larger for the probabilistic framework. This under-estimation of the conductivity magnitude's uncertainty by the WLSQ framework might

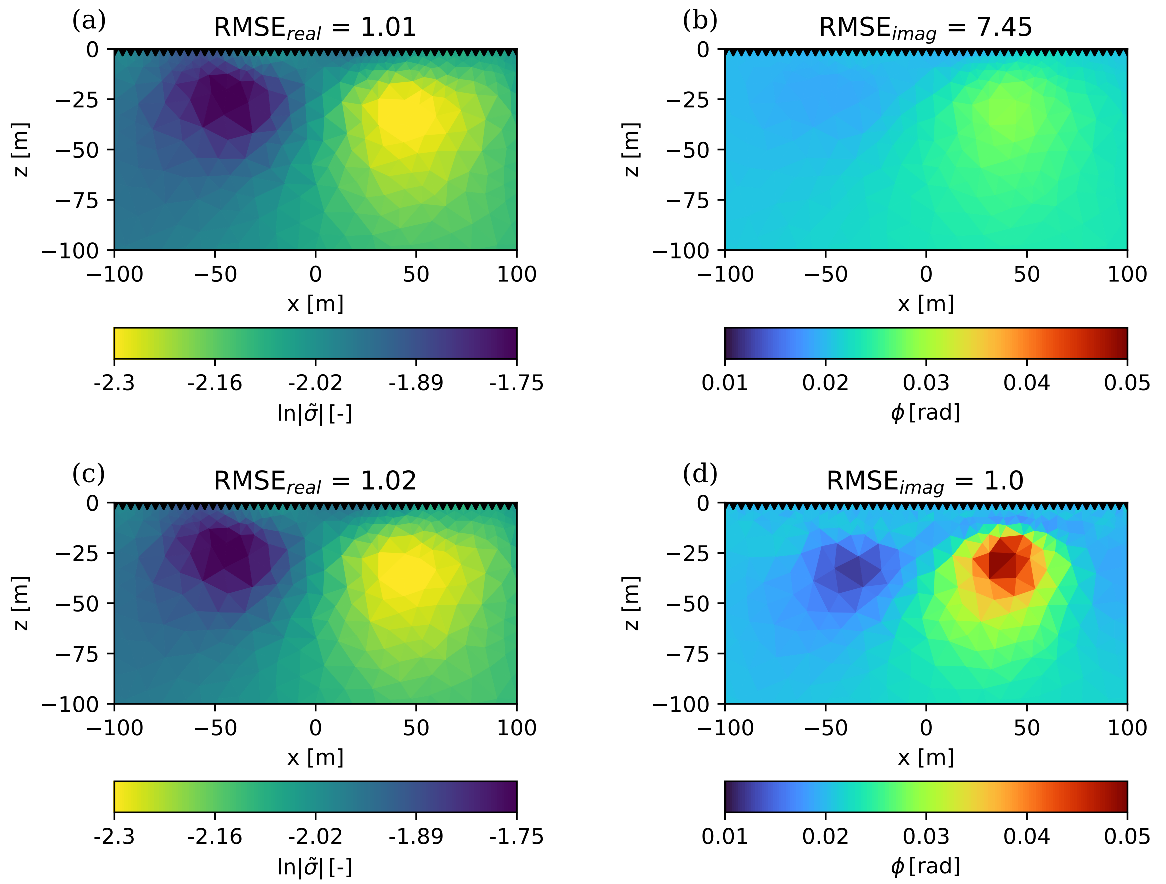

**Figure 4.2:** Conductivity magnitude **(a, c)** and phase **(b, d)** images resulting from the inversion of the synthetic data (compare Figure 4.1) using the WLSQ framework **(a, b)** and the probabilistic framework **(c, d)**.

lead to false interpretations of the inversion result.

### 4.3.2 Example II.: Independent conductivity magnitude and phase regularization

To demonstrate the probabilistic framework's ability to apply independent regularization to the conductivity magnitude and phase, we inverted data from a dipole-dipole survey that was simulated over the subsurface model shown in Figure 4.4a and b. The synthetic model exhibits different structural characteristics in the magnitude and the phase of the subsurface conductivity. While the magnitude is horizontally layered, the layers of the phase show a dip of $-45°$. During the inversion, we used non-isotropic geostatistical regularization operators provided by pyGIMLi (Rücker et al. 2017; Jordi et al. 2018), to account for the different dipping in conductivity magnitude and phase, and compared the results to the images obtained from an inversion with isotropic geostatistical regularization acting on the conductivity magnitude and phase. For both inversions, the regularization strengths were adjusted such that the data were appropriately fitted and the prior model was chosen to be $\tilde{\mathbf{m}}_p = \mathbf{0}$. The data error estimates of impedance magnitude and phase were accounted for accurately, according to Equation (4.5).

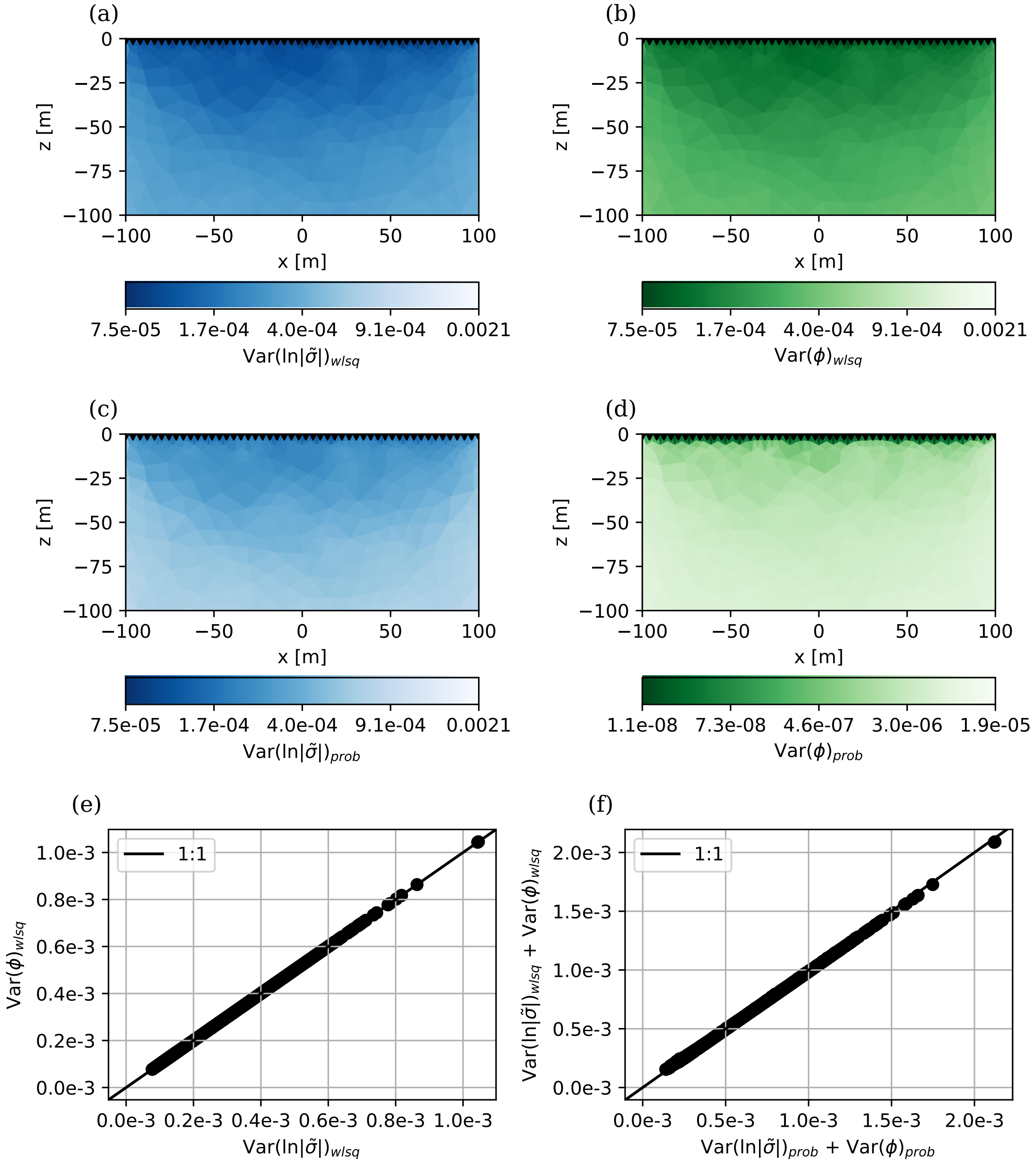

**Figure 4.3:** Estimated variances of the conductivity magnitude **(a, c)** and phase **(b, d)** according to Equation (4.40) for the WLSQ framework **(a, b)** and the probabilistic framework **(c, d)**. Note the different color scale in **(d)**. Scatter of the conductivity phase variances against the conductivity magnitude variances, obtained for the WLSQ framework **(e)**. Scatter of the added conductivity magnitude and phase variances for the WLSQ and probabilistic framework **(f)**.

The results obtained from the two inversions (compare Figure 4.4) demonstrate the advantage of using appropriate non-isotropic geostatistical regularization over isotropic regularization, in the present case. As the probabilistic framework introduced in this work is able to apply independent regularization on the conductivity magnitude and phase, setting it apart from the WLSQ framework, it is possible to account for the different structural characteristics and recover both parameters distributions well (compare Figure 4.4e and f). This is contrasted by the poor recovery of the parameters, especially of the conductivity phase, if the same structural characteristics are favored by isotropic regularization acting on conductivity magnitude and phase (compare Figure 4.4c and d), as it is the case for the WLSQ framework (compare Equations (4.10) and (4.32)).

## 4.4 Conclusion

We introduced a probabilistic framework for the solution of geophysical inverse problems in complex variables. With regard to the inversion of CR measurements, the framework combines three key features whose importance has been demonstrated by Wang et al. (2023). First, it provides the possibility to account for independent error estimates of impedance magnitude and phase. This is essential to formulate the inverse problem in a consistent probabilistic sense, given that the error estimates of impedance magnitude and phase are not equal. While we demonstrated the application of the probabilistic framework for uncorrelated errors, correlations between errors of different data points, as well as between impedance magnitude and phase errors of the same data point, can be included according to Equation (4.5). Second, in order to impose independent regularization on the conductivity magnitude and phase, the respective model priors must be controlled individually. We achieve this by allowing for independent regularization operators to act on conductivity magnitude and phase. Third, the probabilistic framework incorporates cross-sensitivities accurately via the imaginary part of $\tilde{G}_{ik}$, defined in Equation (4.25).

The probabilistic framework introduced in this work is built upon Bayes' theorem, combining a likelihood term and a model prior term into a posterior distribution for the complex model. The correct formulation of the underlying probability distributions, as well as the solution of the inverse problem by means of optimization, both demand usage of the conjugate coordinate representation of complex vectors. We solved the inverse problem resulting from the probabilistic formulation by means of Gauss-Newton optimization, estimating the MAP model under the posterior distribution. Between the probabilistic and WLSQ framework, the difference in computational cost comes down to the necessity to operate in a $2N$-dimensional complex data space and $2M$-dimensional complex model space in case of the probabilistic framework, while for the WLSQ framework this can be reduced to operation in a $N-$dimensional complex data space and $M-$dimensional complex model space. However, this is directly reflected in the inability of the WLSQ framework to account for independent error estimates on the real and imaginary part of the data, and to control the model priors acting on the real and imaginary part of the model individually. For the sake of simplicity, we estimated the variances of the recovered subsurface images under the assumption of normally distributed model-parameter uncertainties near the MAP model. We emphasize that value lies in the application of sampling approaches to the probabilistic CR inverse problem, such as McMC methods, which enable to perform an accurate error propagation and capture ambiguities associated with the solution of non-linear inverse problems. The probabilistic framework for the solution of geophysical inverse problems in complex variables introduced in this work, provides a basis for such developments.

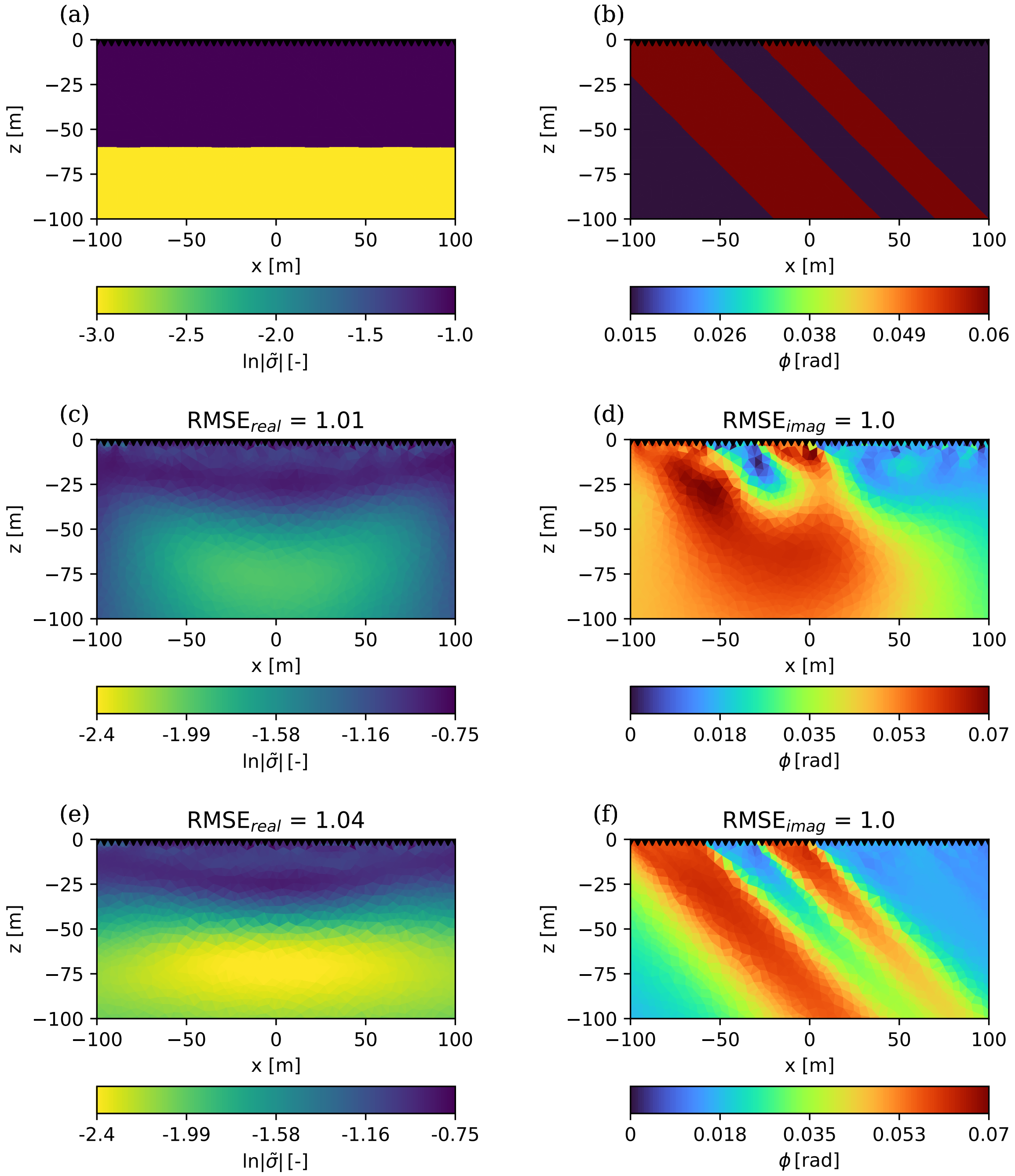

**Figure 4.4:** Model used to create the synthetic data and recovered complex conductivity images. Conductivity magnitude **(a)** and phase **(b)** show strong macroscopic anisotropy. The conductivity magnitude and phase images displayed in **(c)** and **(d)** were recovered using isotropic geostatistical regularization. The conductivity magnitude and phase images displayed in **(e)** and **(f)** were recovered from an inversion, during which non-isotropic geostatistical regularization was applied independently to the conductivity magnitude and phase.

# CHAPTER 5

## Probabilistic geophysical inversion of complex resistivity measurements using the Hamiltonian Monte Carlo method

## Abstract

In this work, we introduce the probabilistic inversion of tomographic complex resistivity (CR) measurements using the Hamiltonian Monte Carlo (HMC) method. The posterior distribution on which our approach operates accounts for the underlying complex-valued nature of the CR imaging problem accurately by including the individual errors of the measured impedance magnitude and phase, allowing for the application of independent regularization on the inferred subsurface conductivity magnitude and phase, and incorporating the effects of cross-sensitivities. As the tomographic CR inverse problem is non-linear, of high dimension and features strong correlations between model parameters, efficiently sampling from the posterior distribution is challenging. To meet this challenge we use HMC, a Markov chain Monte Carlo method that incorporates gradient information to achieve efficient model updates. To maximize the benefit of a given number of forward calculations, we use the No-U-Turn sampler (NUTS) as a variant of HMC. We demonstrate the probabilistic inversion approach on a synthetic CR tomography measurement. The NUTS succeeds in creating a sample of the posterior distribution that provides us with the ability to analyze correlations between model parameters and to calculate statistical estimators of interest, such as the mean model and the covariance matrix. Our results provide a strong basis for the characterization of the posterior distribution and for uncertainty quantification in the context of the tomographic CR inverse problem.

This chapter was published as:

Hase, J., Wagner, F.M., Weigand, M., & Kemna, A. (2025). Probabilistic geophysical inversion of complex resistivity measurements using the Hamiltonian Monte Carlo method. *Geophysical Journal International, 240*(1), 349-361. https://doi.org/10.1093/gji/ggae389

## 5.1 Introduction

We introduce the probabilistic inversion of complex resistivity (CR) tomography measurements using the Hamiltonian Monte Carlo (HMC) method. HMC utilizes the gradient information available for CR tomography measurements to efficiently sample from the posterior distribution. The results provide a strong basis for the analysis of the posterior distribution and uncertainty quantification in the context of CR imaging. During CR surveys, the conduction and polarization properties of the subsurface are inferred from tomographic measurements of the frequency-dependent complex electrical impedance (e.g., Van Voorhis et al. 1973; Pelton et al. 1978). Tomographic CR surveys have proven to be a valuable tool in various areas of application, such as hydrogeophysics (e.g., Kemna et al. 2004; Attwa and Günther 2013), permafrost research (e.g., Mudler et al. 2022; Maierhofer et al. 2022) and agrogeophysics/biogeophysics (e.g., Martin and Günther 2013; Weigand et al. 2022). The tomographic inversion of CR measurements is based on the numerical solution of the Poisson equation, for example using the finite-element (FE) method (e.g., Kemna 2000), leading to a non-linear inverse problem that is typically of high dimension. Previous studies have inverted complex electrical impedance measurements into images of complex electrical conductivity (Weller et al. 1996b; Kemna 2000; Martin and Günther 2013; Johnson and Thomle 2018; Tso et al. 2024) using various approaches and frameworks. In several of these frameworks, drawbacks exist with regard to the consistent handling of data errors and incorporation of cross-sensitivities, arising from the solution of the Poisson equation, as analyzed recently by Wang et al. (2023). In CR imaging, cross-sensitivities describe the sensitivity of the measured impedance magnitude to the imaged conductivity phase, as well as the sensitivity of the measured impedance phase to the imaged conductivity magnitude. As researchers continue to improve the quantitative diagnostic potential of the CR method by relating conduction and polarization characteristics of rocks and soils to petrophysical parameters of interest (e.g., Vinegar and Waxman 1984; Kemna et al. 2004; Binley et al. 2005; Weller et al. 2010; 2013; 2015), the utilization of sophisticated tomographic inversion approaches, that provide a valid uncertainty quantification, becomes essential.

In the past decades, the probabilistic formulation of the geophysical inverse problem as a problem of Bayesian inference has been established for various geophysical disciplines (e.g., Sen and Stoffa 1996; Mosegaard et al. 2002; Tarantola 2005). Combining a likelihood and prior term into a posterior distribution, the probabilistic approach inherently accounts for data errors and uncertainties in the prior assumptions, both of which are propagated naturally into the solution. As the posterior distribution represents the basis on which the probabilistic inversion approach operates, it must be chosen carefully to capture all essential characteristics of the tomographic CR problem. Explicitly, it has to account for the individual uncertainties of impedance magnitude and phase, enable the application of independent regularization on conductivity magnitude and phase, and account for cross-sensitivities originating from the complex forward calculation. Hase et al. (2024) introduced such a posterior distribution, which represents a probabilistic generalization of the established formulation described by Kemna (2000), along with a deterministic solution by means of Gauss-Newton optimization, providing an efficient way to estimate the maximum a posteriori (MAP) solution. For non-linear inverse problems like CR imaging, the deterministic solution lags the ability to estimate integral properties of the posterior distribution, to perform an accurate uncertainty quantification and to capture ambiguities in the solution of the inverse problem. Based on the limited information provided by the deterministic inversion result, uncertainties can only be approximated locally using the simplifying assumption of normally distributed model parameters in the vicinity of the MAP solution, the validity of which remains to be investigated for the probabilistic formulation introduced by Hase et al. (2024).

To utilize the full potential of the probabilistic formulation and ensure an accurate global uncertainty quantification, researchers have started to apply Markov chain Monte Carlo (McMC) methods to various kinds of geophysical inverse problems (e.g., Sambridge and Mosegaard 2002), including geoelectric imaging (e.g., De Pasquale et al. 2019). In an effort to overcome the curse of dimensionality (e.g., Betancourt 2017), McMC methods sample from the posterior distribution by performing a random walk through the model space, with the model updates being controlled by transition rules that are designed to ensure convergence as the sample size grows to infinity. While the model proposals within the random walk can be purely random (e.g., Metropolis et al. 1953; Hastings 1970), additional information on the posterior distribution can be taken into account, potentially favoring a quicker convergence of the generated sample. In CR imaging specifically, gradient information on the negative logarithm of the posterior distribution (negative log-posterior) can be derived with little additional computational effort, using a sensitivity calculation that is based on the potential distributions resulting from a previous evaluation of the tomographic forward response (Kemna 2000). HMC is a McMC method with the ability to use this gradient information to generate efficient model updates (e.g., Neal et al. 2011) and quickly guide the random walk to regions of the model space associated with the typical set (Betancourt 2017). It relies on the physical analogy of a particle moving through the model space, with its trajectory being described by Hamilton's equations of motion. The No-U-turn sampler (NUTS) (Hoffman et al. 2014) is an extension to HMC which optimizes the length of the simulated trajectory dynamically, maximizing the benefit of a given number of forward calculations. Muir and Tkalčić (2015; 2020) and Sen and Biswas (2017) represent some of the earliest applications of HMC to geophysical inverse problems. Fichtner et al. (2019) used HMC to solve multiple tomographic geophysical inverse problems, including linear and non-linear traveltime tomography, as well as reflection seismology. Since then, HMC has been applied to a number of geophysical inverse problems (e.g., Aleardi and Salusti 2020; Gebraad et al. 2020; Zunino et al. 2022; Peng et al. 2024).

This study is structured as follows: We briefly explain the physical concepts underlying the CR method, followed by an introduction of the posterior distribution formulated by Hase et al. (2024), which will serve as the basis for the probabilistic inversion of CR measurements in this work. After that, we provide a short recap of the theory concerning HMC and the NUTS, complemented by the explicit adaptation of Hamilton's equations to inverse problems in complex variables. Using a synthetic study, we demonstrate the inversion of CR measurements by means of HMC sampling. Convergence is assessed by evaluation of the potential-scale reduction factor (PSRF), which is calculated on the basis of multiple random walks run in parallel. We quantify correlations between model parameters and investigate their spatial characteristics. On the basis of the generated sample, we estimate the mean model and the posterior covariance matrix, demonstrating how the results of the inversion approach can be used for uncertainty quantification. We discuss how the result of the HMC inversion relates to the result of the deterministic inversion and how both approaches complement each other. Finally, we conclude our results.

## 5.2 Probabilistic inversion of complex resistivity measurements

### 5.2.1 Complex resistivity imaging

In CR imaging, forward modeling is conducted by calculating the complex electrical potential $\tilde{\psi}(\omega)$ at angular frequency $\omega$. Given a distribution of complex electrical conductivity $\tilde{\sigma} = \sigma' + i\sigma''$, with $i^2 = -1$ and the prime notation denoting the real and imaginary part of the complex number, the complex electrical potential is obtained as the solution of the Poisson equation:

$$\nabla \cdot \left(\tilde{\sigma}(\omega)\nabla\tilde{\psi}(\omega)\right) - \nabla \cdot \tilde{\mathbf{J}}_s(\omega) = 0, \tag{5.1}$$

with the source current density $\tilde{\mathbf{J}}_s$. The complex electrical impedance $\tilde{Z} = Z' + iZ''$ is given by the ratio of the measured potential difference to the injected current. We adopt the logarithmic transformation of the data and the logarithmic parameterization of the model from Kemna (2000) and Hase et al. (2024). Given $N$ impedance measurements $\tilde{Z}_i$, the complex data $\tilde{\mathbf{d}} = \mathbf{d}' + i\mathbf{d}'' \in \mathbb{C}^N$ are given by:

$$\tilde{d}_i = -\ln(\tilde{Z}_i) = -\ln|\tilde{Z}_i| + i\varphi_i, \tag{5.2}$$

with the negative phase of the complex electrical impedance $\varphi_i$. The complex electrical impedance is related to the apparent complex conductivity

$$\tilde{\sigma}_{a_i} = \frac{1}{k_i\tilde{Z}_i}, \tag{5.3}$$

which we use for the visual display of the data in pseudo-sections, via the geometric factor $k_i$ (e.g., Knödel et al. 2013; Everett 2013). The model $\tilde{\mathbf{m}} = \mathbf{m}' + i\mathbf{m}'' \in \mathbb{C}^M$ is formulated as the complex logarithm of the complex electrical conductivity:

$$\tilde{m}_k = \ln(\tilde{\sigma}_k) = \ln|\tilde{\sigma}_k| + i\phi_k. \tag{5.4}$$

Here, $\phi_k$ represents the phase of the complex electrical conductivity. In the interest of readability, we refer to the real and imaginary parts of the complex data $\tilde{d}_i$ as the *impedance magnitude* and *impedance phase*, while referring to the real and imaginary parts of the complex model $\tilde{m}_k$ as the *conductivity magnitude* and *conductivity phase.*

The complex forward calculation is denoted by $\tilde{\mathbf{f}}(\tilde{\mathbf{m}})$. For our purposes, solving Equation (5.1) is achieved by means of finite-element modeling (FEM) (Kemna 2000), using the capabilities of the open-source software package pyGIMLi (Rücker et al. 2017). In the 2.5D case, the solution is obtained for the cosine-transformed complex electrical potential in the wavenumber domain, evaluated at different wavenumbers. For a given impedance measurement, sensitivities

$$\tilde{\mathrm{G}}_{ik} = \frac{\partial \tilde{f}_i}{\partial \tilde{m}_k} \tag{5.5}$$

can be calculated based on the principle of reciprocity (e.g., Rodi 1976; Oristaglio and Worthington 1980; Kemna 2000), under the consideration of a fictitious transformed potential distribution originating in a fictitious current source at the location of the potential electrode, yielding the complex Jacobian matrix $\tilde{\mathbf{G}}$. In practice, most electrodes used for potential measurements are used for current injections as well at another point in time. If this is the case, the fictitious transformed potential distributions are effectively evaluated as part of the forward calculation and can be used to derive the sensitivities. Gradient information on the negative log-posterior can therefore be evaluated with little additional computational effort, suggesting that it is sensible to utilize it within the probabilistic inversion scheme. Note that the complex electric potential is analytic (Kemna 2000), meaning that the forward calculation is complex differentiable and that the sensitivities fulfill the Cauchy-Riemann equations:

$$\frac{\partial f_i'}{\partial m_k'} = \frac{\partial f_i''}{\partial m_k''}, \tag{5.6}$$

$$\frac{\partial f_i'}{\partial m_k''} = -\frac{\partial f_i''}{\partial m_k'}. \tag{5.7}$$

### 5.2.2 Construction of the posterior distribution

The goal of our work is to invert a data set of complex impedance measurements into a subsurface image of complex conductivity, under consideration of data errors and prior information. We adopt the probabilistic framework for the solution of geophysical inverse problems in complex variables introduced by Hase et al. (2024), which is built on Bayes' theorem (Bayes 1763):

$$p(\overset{c}{\mathbf{m}} \mid \overset{c}{\mathbf{d}}) \propto p(\overset{c}{\mathbf{d}} \mid \overset{c}{\mathbf{m}})\; p(\overset{c}{\mathbf{m}}), \tag{5.8}$$

combining the likelihood term $p(\overset{c}{\mathbf{d}} \mid \overset{c}{\mathbf{m}})$ and the prior term $p(\overset{c}{\mathbf{m}})$ into the posterior distribution $p(\overset{c}{\mathbf{m}} \mid \overset{c}{\mathbf{d}})$. The posterior distribution assigns a conditional probability to a model realization $\overset{c}{\mathbf{m}}$, given the data $\overset{c}{\mathbf{d}}$. For the formulation of the probability distributions associated with the likelihood and prior term, the framework follows Picinbono (1996) and uses the conjugate coordinate representation of complex vectors (e.g., Kreutz-Delgado 2009). For the complex vector $\tilde{\mathbf{x}} = \mathbf{x}' + i\mathbf{x}'' \in \mathbb{C}^M$ we define $\overset{c}{\mathbf{x}} \overset{\Delta}{=} \frac{1}{\sqrt{2}} (\tilde{\mathbf{x}}, \tilde{\mathbf{x}}^*)^T \in \mathbb{C}^{2M}$ to be its representation in conjugate coordinates, with $^*$ denoting the complex conjugation and $^T$ denoting the transpose. The representation in conjugate coordinates is related to the representation of $\tilde{\mathbf{x}}$ in terms of its real and imaginary part $\overset{r}{\mathbf{x}} \overset{\Delta}{=} (\mathbf{x}', \mathbf{x}'')^T \in \mathbb{R}^{2M}$ by the linear transformation

$$\overset{c}{\mathbf{x}} = \underbrace{\frac{1}{\sqrt{2}} \begin{bmatrix} \mathbf{I} & i\mathbf{I} \\ \mathbf{I} & -i\mathbf{I} \end{bmatrix}}_{\tilde{\mathbf{S}}} \overset{r}{\mathbf{x}}, \tag{5.9}$$

with $\mathbf{I} \in \mathbb{R}^{M \times M}$ denoting the identity matrix. Here, $\tilde{\mathbf{S}}$ is an orthonormal basis $\tilde{\mathbf{S}}^H \tilde{\mathbf{S}} = \mathbf{I}$, using $^H$ to denote the conjugate transpose. Operation in conjugate coordinates ensures the differentiability of the negative log-posterior with respect to the complex valued model by exploiting its differentiability with respect to input from $\mathbb{R}^{2M}$ (Sorber et al. 2012), which is essential for the minimization of the negative log-posterior during the deterministic inversion, as well as for the application of HMC.

The likelihood term is given by:

$$p(\overset{c}{\mathbf{d}} \mid \overset{c}{\mathbf{m}}) \propto \exp \left[ -\frac{1}{2} \left[ (\tilde{\mathbf{d}} - \tilde{\mathbf{f}}(\tilde{\mathbf{m}}))^H, (\tilde{\mathbf{d}} - \tilde{\mathbf{f}}(\tilde{\mathbf{m}}))^T \right] \underbrace{\begin{pmatrix} \tilde{\mathbf{C}}_{\mathbf{d}} & \tilde{\mathbf{\Gamma}}_{\mathbf{d}} \\ \tilde{\mathbf{\Gamma}}_{\mathbf{d}}^H & \tilde{\mathbf{C}}_{\mathbf{d}}^* \end{pmatrix}^{-1}}_{=\overset{c}{\mathbf{R}}_{\mathbf{d}}} \begin{pmatrix} \tilde{\mathbf{d}} - \tilde{\mathbf{f}}(\tilde{\mathbf{m}}) \\ (\tilde{\mathbf{d}} - \tilde{\mathbf{f}}(\tilde{\mathbf{m}}))^* \end{pmatrix} \right], \tag{5.10}$$

with the covariance matrix

$$\overset{c}{\mathbf{R}}{}_{\mathbf{d}}^{-1} = \begin{pmatrix} \tilde{\mathbf{C}}_{\mathbf{d}} & \tilde{\mathbf{\Gamma}}_{\mathbf{d}} \\ \tilde{\mathbf{\Gamma}}_{\mathbf{d}}^H & \tilde{\mathbf{C}}_{\mathbf{d}}^* \end{pmatrix} = \tilde{\mathbf{S}} \begin{pmatrix} \mathrm{Cov}(\ln|\tilde{\mathbf{Z}}|, \ln|\tilde{\mathbf{Z}}|) & \mathrm{Cov}(\ln|\tilde{\mathbf{Z}}|, \varphi) \\ \mathrm{Cov}(\varphi, \ln|\tilde{\mathbf{Z}}|) & \mathrm{Cov}(\varphi, \varphi) \end{pmatrix} \tilde{\mathbf{S}}^{-1}. \tag{5.11}$$

Equation (5.11) accounts for the individual variances of the impedance magnitudes and phases, while also capturing covariances between the two.

The prior term

$$p(\overset{c}{\mathbf{m}}) \propto \exp \left[ -\frac{1}{2} \left[ (\tilde{\mathbf{m}} - \tilde{\mathbf{m}}_p)^H, (\tilde{\mathbf{m}} - \tilde{\mathbf{m}}_p)^T \right] \underbrace{\begin{pmatrix} \mathbf{R}_{\Re} + \mathbf{R}_{\Im} & \mathbf{R}_{\Re} - \mathbf{R}_{\Im} \\ \mathbf{R}_{\Re} - \mathbf{R}_{\Im} & \mathbf{R}_{\Re} + \mathbf{R}_{\Im} \end{pmatrix}}_{=\overset{c}{\mathbf{R}}_{\mathbf{m}}} \begin{pmatrix} \tilde{\mathbf{m}} - \tilde{\mathbf{m}}_p \\ (\tilde{\mathbf{m}} - \tilde{\mathbf{m}}_p)^* \end{pmatrix} \right], \tag{5.12}$$

applies independent regularization to the conductivity magnitude and phase. The symmetric real operators

$$\mathbf{R}_{\Re} = \lambda_{\Re} \left( \mathbf{W}_{\mathbf{m}}^T \mathbf{W}_{\mathbf{m}} \right)_{\Re} \quad \text{and} \tag{5.13}$$

$$\mathbf{R}_{\Im} = \lambda_{\Im} \left( \mathbf{W}_{\mathbf{m}}^T \mathbf{W}_{\mathbf{m}} \right)_{\Im}, \tag{5.14}$$

with regularization strengths $\lambda_{\Re}$ and $\lambda_{\Im}$, favor similarity between neighboring model parameters. Note that larger choices for $\lambda_{\Re}$ and $\lambda_{\Im}$ imply a lower prior uncertainty. The regularization operators act separately on the images of conductivity magnitude and phase. By definition, a large amount of correlations between model parameters is introduced into the inverse problem by the use of these smoothing constraints.

### 5.2.3 Adaptation of Hamiltonian Monte Carlo to inverse problems in complex variables

Markov chain Monte Carlo (McMC) methods sample from a target distribution by performing a random walk through the model space (e.g., Sambridge and Mosegaard 2002), with the practical objective of accurately evaluating integral estimators using a limited amount of model realizations (e.g., Betancourt 2017). Carefully designed transition rules ensure that the relative frequency, with which a certain model realization is generated, converges against the probability of said model realization under the target distribution. One of the most basic McMC algorithms is the Random-walk Metropolis Hastings (MH) sampler (Metropolis et al. 1953; Hastings 1970), which relies on a purely random proposal step, drawing the update from a symmetric proposal distribution. HMC extends upon this concept by incorporating gradient information on the negative log-posterior into the proposal step to achieve more efficient model updates (e.g., Neal et al. 2011; Betancourt 2017). In HMC, the physical analogy of a particle moving trough the model space is used to generate a proposed state, where the state of the particle is given by its position in the model space $\overset{r}{\mathbf{m}}\in \mathbb{R}^{2M}$ and its momentum $\mathbf{p} \in \mathbb{R}^{2M}$. The conserved total energy of the system is called the Hamiltonian $H(\overset{r}{\mathbf{m}}, \mathbf{p})$. It equals the sum of the particle's potential energy $U(\overset{r}{\mathbf{m}})$ and kinetic energy $K(\mathbf{p})$:

$$\begin{aligned} H(\overset{r}{\mathbf{m}}, \mathbf{p}) &= U(\overset{r}{\mathbf{m}}) + K(\mathbf{p}), && (5.15)\\ &= -\ln\left(p(\overset{c}{\mathbf{m}} \mid \overset{c}{\mathbf{d}})\right) + \frac{1}{2}\mathbf{p}^T\mathbf{M}^{-1}\mathbf{p}, && (5.16) \end{aligned}$$

with $\mathbf{M} \in \mathbb{R}^{2M\times 2M}$ representing the fictitious mass. The potential energy, which can be thought of as the topography the particle moves on, is defined in terms of the negative log-posterior. HMC samples from the joint distribution of the particle's position and momentum, called the canonical distribution (Neal et al. 2011)

$$p_c(\overset{r}{\mathbf{m}}, \mathbf{p}) \propto \exp\left(-H(\overset{r}{\mathbf{m}}, \mathbf{p})\right), \tag{5.17}$$

from which a sample of the posterior distribution can be obtained by marginalizing over the values of $\mathbf{p}$. For a current model realization $\overset{r}{\mathbf{m}}$, the proposal is performed as follows: A value for the momentum is drawn from $p(\mathbf{p}) \propto \exp\left(-K(\mathbf{p})\right)$. The state of the particle is then propagated through fictitious time $t$ by solving Hamilton's equations of motion

$$\begin{aligned} \frac{\mathrm{d}\,\mathbf{p}}{\mathrm{d}\,t} &= -\frac{\partial H}{\partial \overset{r}{\mathbf{m}}} = \frac{\partial \ln\left(p(\overset{c}{\mathbf{d}} \mid \overset{c}{\mathbf{m}})\right)}{\partial \overset{r}{\mathbf{m}}} + \frac{\partial \ln\left(p(\overset{c}{\mathbf{m}})\right)}{\partial \overset{r}{\mathbf{m}}}, && (5.18a)\\ &= \left(\begin{bmatrix} \tilde{\mathbf{G}} & \mathbf{0} \\ \mathbf{0} & \tilde{\mathbf{G}}^* \end{bmatrix} \tilde{\mathbf{S}}\right)^H \overset{c}{\mathbf{R}}_{\mathbf{d}} \begin{pmatrix} \tilde{\mathbf{d}} - \tilde{\mathbf{f}}(\tilde{\mathbf{m}}) \\ (\tilde{\mathbf{d}} - \tilde{\mathbf{f}}(\tilde{\mathbf{m}}))^* \end{pmatrix} - \tilde{\mathbf{S}}^H \overset{c}{\mathbf{R}}_{\mathbf{m}} \tilde{\mathbf{S}} \begin{pmatrix} \mathbf{m}' \\ \mathbf{m}'' \end{pmatrix}, && (5.18b)\\ \frac{\mathrm{d}\,\overset{r}{\mathbf{m}}}{\mathrm{d}\,t} &= \frac{\partial H}{\partial \mathbf{p}} = \mathbf{M}^{-1}\mathbf{p}, && (5.18c) \end{aligned}$$

via Leapfrog integration for $L$ time steps. To fulfill detailed balance, the proposed state $(\overset{r}{\mathbf{m}}^+, \mathbf{p}^+)$ is accepted according to a MH criterion, with the acceptance probability (Neal et al. 2011)

$$\alpha = \min\left[1, \exp\left(-H(\overset{r}{\mathbf{m}}^{+}, \mathbf{p}^{+}) + H(\overset{r}{\mathbf{m}}, \mathbf{p})\right)\right], \tag{5.19}$$

ensuring that the generated sample converges against the posterior distribution. For more details on the HMC algorithm itself, we refer the reader to Neal et al. (2011) and Fichtner et al. (2019).

One important hyperparameter in HMC is the number of time steps $L$ for which the movement of the particle is simulated. Intuitively, an efficient choice for $L$ maximizes the effective distance of the model update. Depending on the topography of the potential energy in the vicinity of the current model realization, solving Equations (5.18) for an increasing amount of time steps can lead to a decrease of the model update's effective distance, as the simulated trajectory loops back on itself, wasting computational effort in the process. To solve this problem, Hoffman et al. (2014) introduced the NUTS, which adapts the trajectory length dynamically, maximizing the effective distance of the model update, while avoiding unnecessary evaluations of the forward response. For this work, we follow the implementation of algorithm 3 in the original paper.

The mass matrix $\mathbf{M}$ (compare Equation (5.15)) has no direct analogy in the physical context of CR imaging, but it can be modified to enhance the efficiency and stability of the algorithm. As the values of the conductivity magnitude and phase can differ by orders of magnitude, the mass matrix can be used to scale the individual components of the model update appropriately, which we found to be essential in practice. Fichtner et al. (2019) demonstrate that it is favorable to set $\mathbf{M}$ equal to an approximation of the inverse posterior covariance matrix, if such an approximation is available. Therefore, we use an approximation of the Hessian near the MAP solution $\hat{\mathbf{H}}$ (Tarantola 2005) as the mass matrix. The effect of choosing the mass matrix appropriately is demonstrated in Figure 5.1. Figure 5.1a shows a simulated trajectory for the conductivity magnitude and phase of the same model parameter when the mass matrix is chosen as $\mathbf{M} = \hat{\mathbf{H}}$ and used to scale the model proposal appropriately, while Figure 5.1b shows the trajectory for $\mathbf{M} = \mathbf{I}$. Both trajectories are simulated until the effective distance of the model proposal starts to decrease. The difference in efficiency can be clearly seen by comparing the effective distances of the two model proposals, especially in case of the conductivity magnitude. Recently, Fichtner et al. (2021) introduced a modification of HMC, which allows for automatic tuning of the mass matrix. Automatically tuning the mass matrix during the random walk leads to a loss of the Markov property, meaning that the generated sample is not guaranteed to converge against the posterior distribution. Although Fichtner et al. (2021) demonstrate the validity of their algorithm despite the loss of the Markov property, we nevertheless chose to stick to a constant mass matrix for this work.

The step length $\varepsilon$ used during the numerical integration of Hamilton's equations is tuned automatically using a vanishing adaption approach (Andrieu and Thoms 2008; Hoffman et al. 2014), targeting a desired average acceptance probability of $\delta = 0.65$, as derived by Neal et al. (2011). During each iteration $j$, the step length is updated according to:

$$\varepsilon_{j+1} \leftarrow \varepsilon_j - j^{-\kappa}\left(\delta - \bar{\alpha}_j\right), \tag{5.20}$$

with $\kappa = 0.75$ and $\bar{\alpha}_j$ being the average acceptance probability after $j$ iterations, calculated as the ratio of the number of accepted model proposals to the total number of iterations performed.

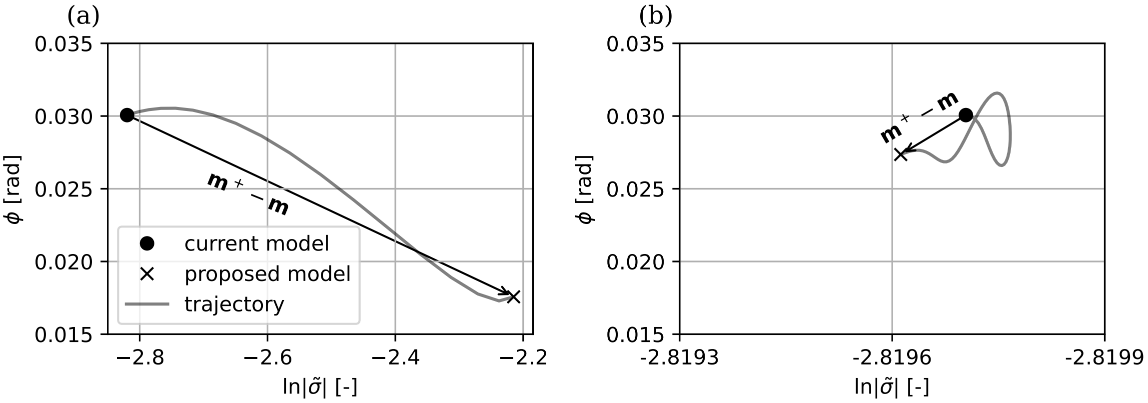

**Figure 5.1:** **(a)** Simulated trajectory for $\mathbf{M} = \hat{\mathbf{H}}$, leading to a large model proposal. **(b)** Simulated trajectory for $\mathbf{M} = \mathbf{I}$, leading to a small model proposal.

Different approaches exist to assess the convergence of the generated sample (e.g., Cowles and Carlin 1996). Besides manual inspection of the statistical estimators we are interested in, we use the potential-scale reduction factor (PSRF) (Gelman and Rubin 1992), as implemented in TensorFlow (Abadi et al. 2015), for a quantitative and non-subjective convergence assessment. The PSRF relates the variance observed within a single random walk to the variance observed between different random walks, with its value approaching 1 as the number of iterations approaches infinity and the sample converges. It is calculated for each model parameter separately. In practice, we follow Brooks and Gelman (1998) and consider a PSRF value of 1.2 to be the threshold for approximate convergence of the considered model parameter.

## 5.3 Application

In the following, we demonstrate the probabilistic inversion of tomographic CR measurements using the NUTS. A dipole-dipole survey, with multiple skips of separation between both current and voltage electrodes, was simulated over the subsurface model shown in Figures 5.2a,b to generate the data set shown in Figures 5.2c,d. Electrode configurations associated with a geometric factor larger than 8000 were excluded. The synthetic survey was simulated for a 200 m profile with 50 electrodes, resulting in 643 complex-valued data points. Noise following commonly used error models for impedance magnitude and phase was added to the synthetic measurements (LaBrecque et al. 1996; Flores Orozco et al. 2012b). The associated standard deviations are displayed in Figures 5.2e,f. For the inversion we used mesh-independent, isotropic geostatistical regularization, as implemented in pyGIMLi (Jordi et al. 2018), with a correlation length of 10 m. The geostatistical regularization operators acting on conductivity magnitude and phase were scaled using the regularization strengths $\lambda_{\Re}$ and $\lambda_{\Im}$ (compare Equation (5.13)) to fit the complex measurements appropriately in the context of their uncertainties. The prior model was chosen to be $\tilde{\mathbf{m}}_p = \mathbf{0}$.

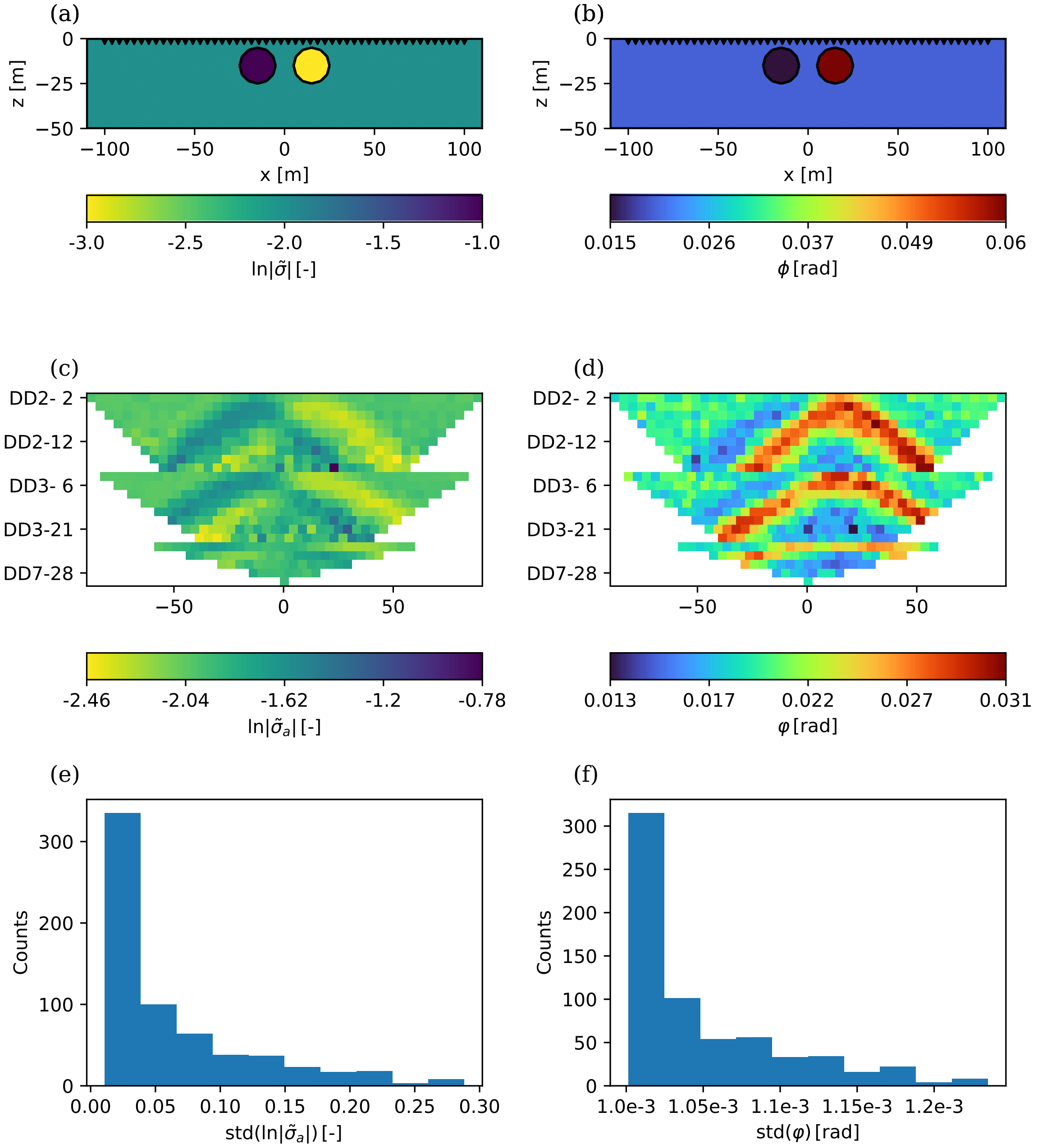

**Figure 5.2:** **(a, b)** Conductivity magnitude and phase of the true model. Electrode positions are indicated in black. **(c, d)** Synthetic dipole-dipole measurements generated for the subsurface in (a, b), with pseudo-depth levels on the vertical axis. **(e, f)** Standard deviation of the noise added to the synthetic measurements.

Five random walks were run in parallel. Each random walk was initialized at a starting model that was obtained by Gauss-Newton optimization of a perturbed posterior distribution, yielding model realizations close to the typical set. For the estimation of the starting models we loosely follow an approach called *Randomize then optimize* (Bardsley et al. 2014). A realization of the perturbed posterior distribution is obtained by replacing the data vector with a realization from $\mathcal{N}(\overset{c}{\mathbf{d}}, \overset{c}{\mathbf{R}}_{\mathbf{d}}^{-1})$ and the prior model with a realization from $\mathcal{N}(\overset{c}{\mathbf{m}}_p, \overset{c}{\mathbf{R}}_{\mathbf{m}}^{-1})$.

Optimizing multiple realizations of the perturbed posterior distribution yields a biased approximation of the true posterior distribution, as demonstrated recently for geophysical problems by Blatter et al. (2022). Note that the starting models do not coincide with the MAP solution of the true posterior distribution. To assess the convergence of the generated sample, we analyze the potential-scale reduction factor (PSRF) as a function of iteration. Figure 5.3a shows the evolution of the PSRF estimates for all model parameters. During the first iterations of the random walks, the PSRF takes values significantly larger than the approximate convergence threshold of 1.2. Within the first 10 000 iterations, the PSRF of most model parameters drops significantly and crosses the approximate convergence threshold of 1.2 (compare Figures 5.3a,b), indicating that the created sample represents a valid approximation of the posterior distribution.

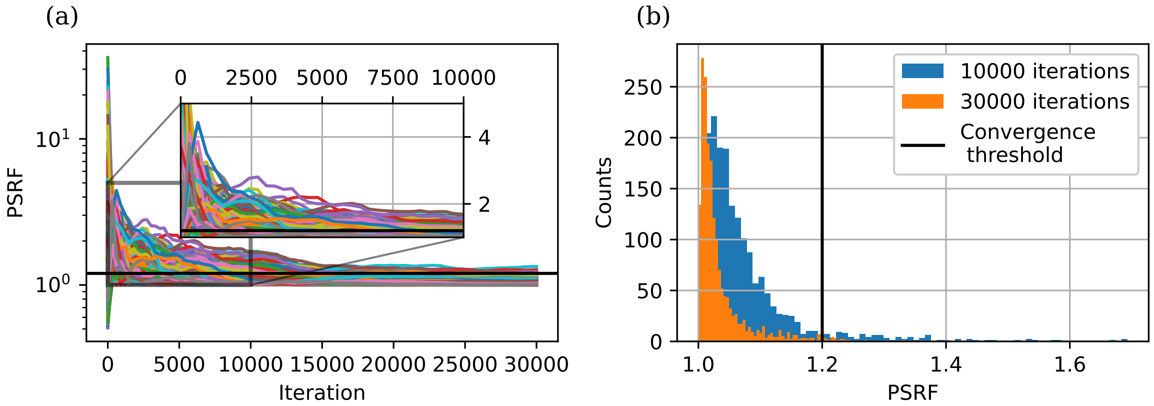

**Figure 5.3:** **(a)** Evolution of the PSRF. **(b)** PSRF obtained for iteration 10 000 and the final iteration.

Figure 5.4 shows the evolution of the random walks over 30 000 iterations. The potential energies (Figures 5.4a-e) stabilize within the first 10 000 iterations, indicating that the NUTS is sampling the typical set. For all random walks, the estimated step lengths $\varepsilon$ stabilize around a value of 0.1 within the first 10 000 iterations, as shown in Figures 5.4f-j. Based on the evolution of the potential energies, the step lengths and the PSRF, we exclude the first 10 000 iterations as burn-in from the further analysis of the sample. In the following, we consider two example model parameters $\tilde{m}_\mathrm{A}$ and $\tilde{m}_\mathrm{B}$, located in a region of high sensitivity and low sensitivity, respectively. Each model parameter has a conductivity magnitude and phase associated to it. Figures 5.4k-t show the generated realizations for $\ln|\tilde{\sigma}|_\mathrm{A}$ alongside the corresponding histograms approximating the marginal distributions. All histograms suggest unimodal marginal distributions of $\ln|\tilde{\sigma}|_\mathrm{A}$.

Figures 5.5c,d show the conductivity magnitude and phase images, obtained as the mean model of the generated sample, alongside a single model realization generated by the random walk (compare Figures 5.5a,b). The mean model resolves both anomalies featured in the synthetic subsurface displayed in Figures 5.2a,b, with their conductivity magnitude and phase being estimated accurately within the limitations caused by the smoothness constraint and the underlying nature of the CR imaging method. Figures 5.5e,f show the conductivity

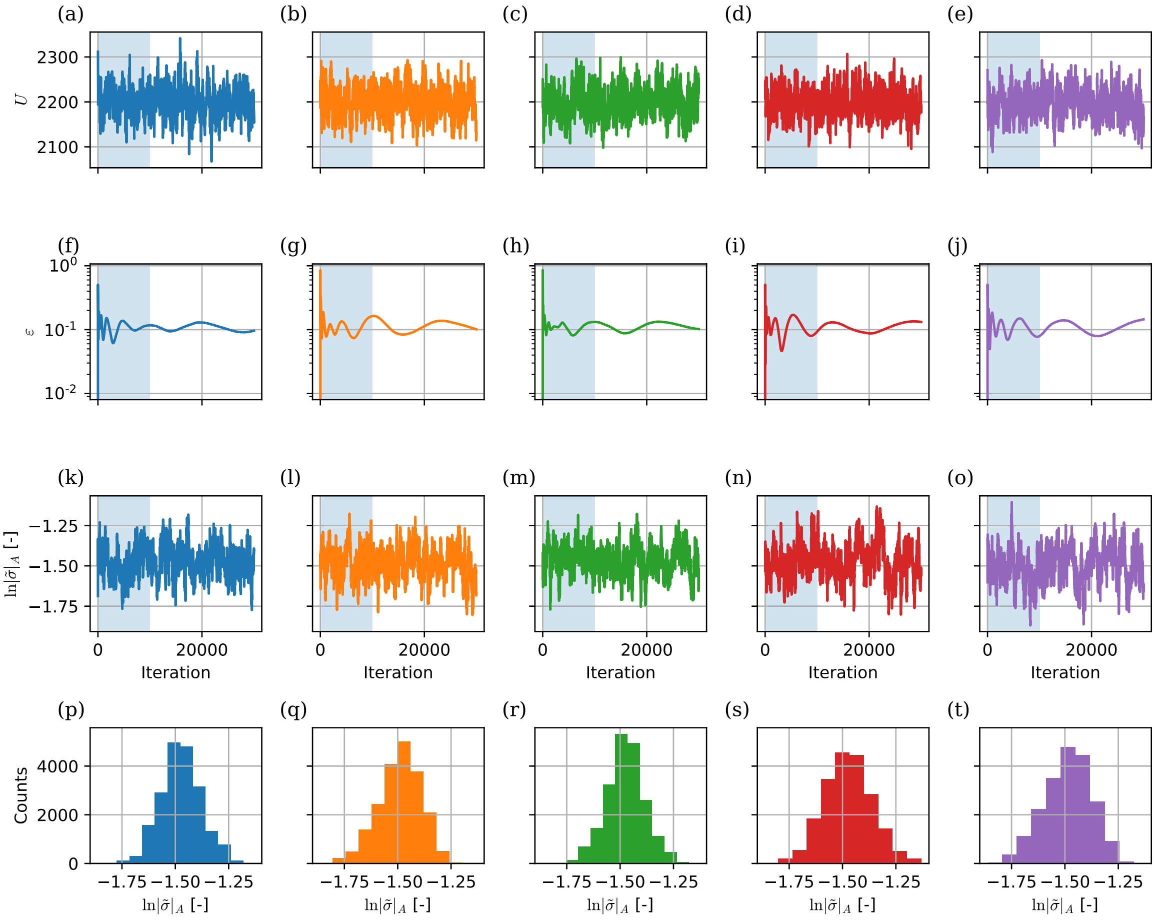

**Figure 5.4:** **(a-e)** Potential energies. **(f-j)** Adapted step length $\varepsilon$ for Leapfrog integration. **(k-o)** Generated random walk for $\ln|\tilde{\sigma}|_{\mathrm{A}}$. The burn-in phase, which is excluded from the sample, is marked in light blue. **(p-t)** Obtained marginal distributions of $\ln|\tilde{\sigma}|_{\mathrm{A}}$.

magnitude and phase images associated with the MAP solution, obtained by the deterministic inversion through Gauss-Newton optimization of the negative log-posterior. We find the conductivity phase images associated with the mean model and the MAP solution to be in good agreement with each other. At depth and in regions of lower sensitivity, the conductivity magnitude image of the mean model deviates from that of the MAP solution, featuring decreased conductivity magnitudes indicated by a shift to lighter colors. Compared to the MAP solution, which fits the data adequately in the context of their uncertainties and yields a root-mean square error (RMSE) of 1, the mean model displays a larger data misfit and a larger model roughness.

To assess correlations between different model parameters in the sample, we evaluate the Spearman correlation coefficient $r_{\mathrm{s}}$ (Spearman 1961). In the following, we visualize correlations within the conductivity magnitude and phase images. For a given reference model parameter, we calculate $r_{\mathrm{s}}$ with respect to all other model parameters and plot the results as a function of distance (compare Figures 5.6a-d). Correlations are high for model parameters close the reference parameter. With increasing distance, the correlations decay quickly. To assess the rate of the decay, we fit exponential terms to the data set. We define the mean

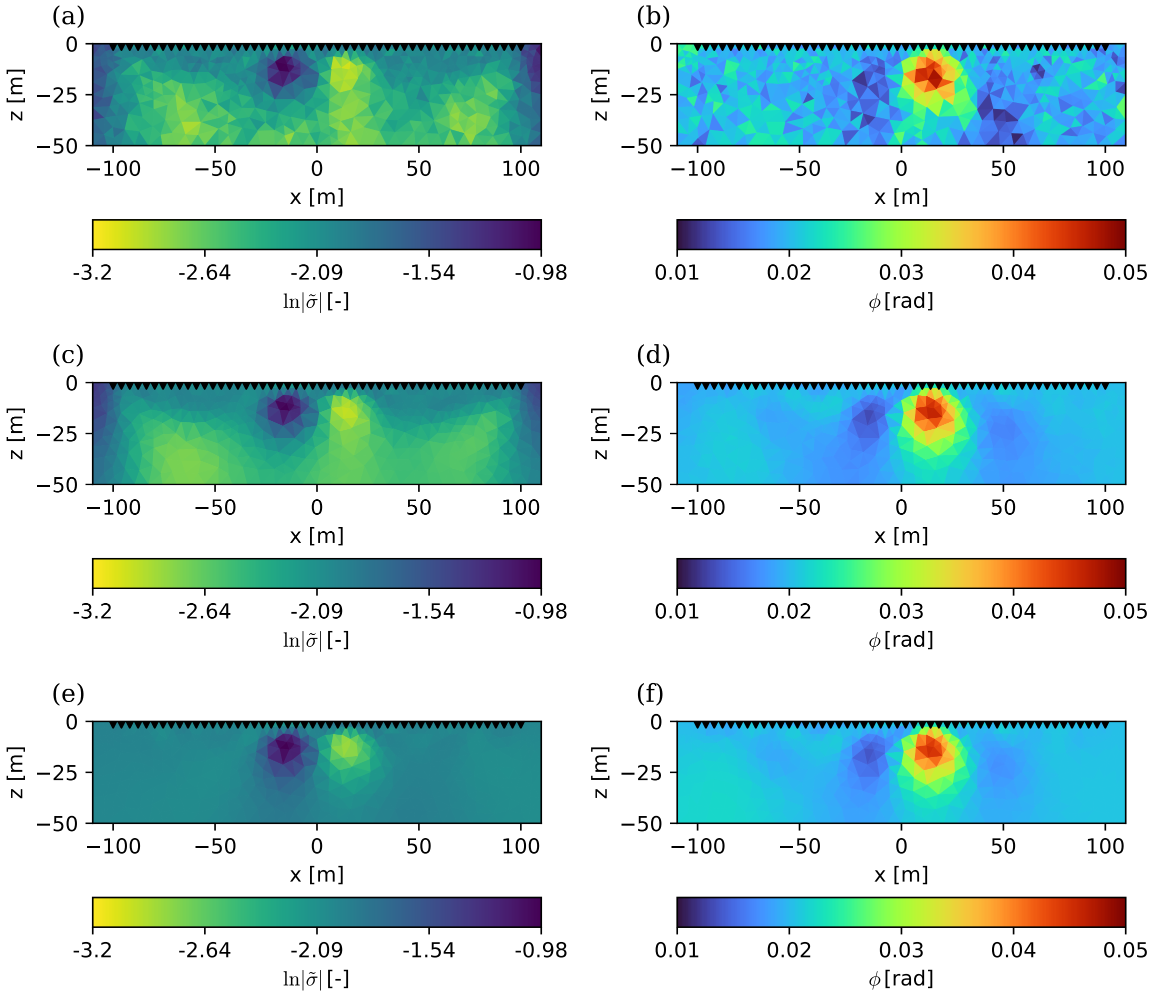

**Figure 5.5: (a, b)** Conductivity magnitude and phase, obtained as a model realization during the random walk. **(c, d)** Conductivity magnitude and phase, obtained as the mean model of the generated sample. **(e, f)** Conductivity magnitude and phase, obtained as the maximum a posteriori solution by means of optimization.

correlation distance $\bar{d}_{\mathrm{c}}$ as the average distance needed for the correlation with respect to a given reference model parameter to fall below a value of $e^{-1}$. The spatial distributions of $\bar{d}_{\mathrm{c}}$ are shown in Figures 5.6e,f for conductivity magnitude and phase. It can be clearly seen that they reflect the expected resolution pattern of the measurement. Since we used mesh-independent geostatistical regularization, the spatial patterns observed in $\bar{d}_{\mathrm{c}}$ are not caused by the varying cell sizes.

The uncertainty of the inferred subsurface model can be quantified by evaluation of the posterior covariance matrix, which is calculated directly from the obtained sample. Figures 5.7a,b,c show parts of the estimated posterior covariance matrix, including variance and covariance estimates for the conductivity magnitudes (compare Figure 5.7a), variance and covariance estimates for the conductivity phase (compare Figure 5.7c), as well as covariances between the two (compare Figure 5.7b). The spatial distributions of the estimated standard deviations for conductivity magnitude and phase are displayed in Figures 5.7d,e. In both

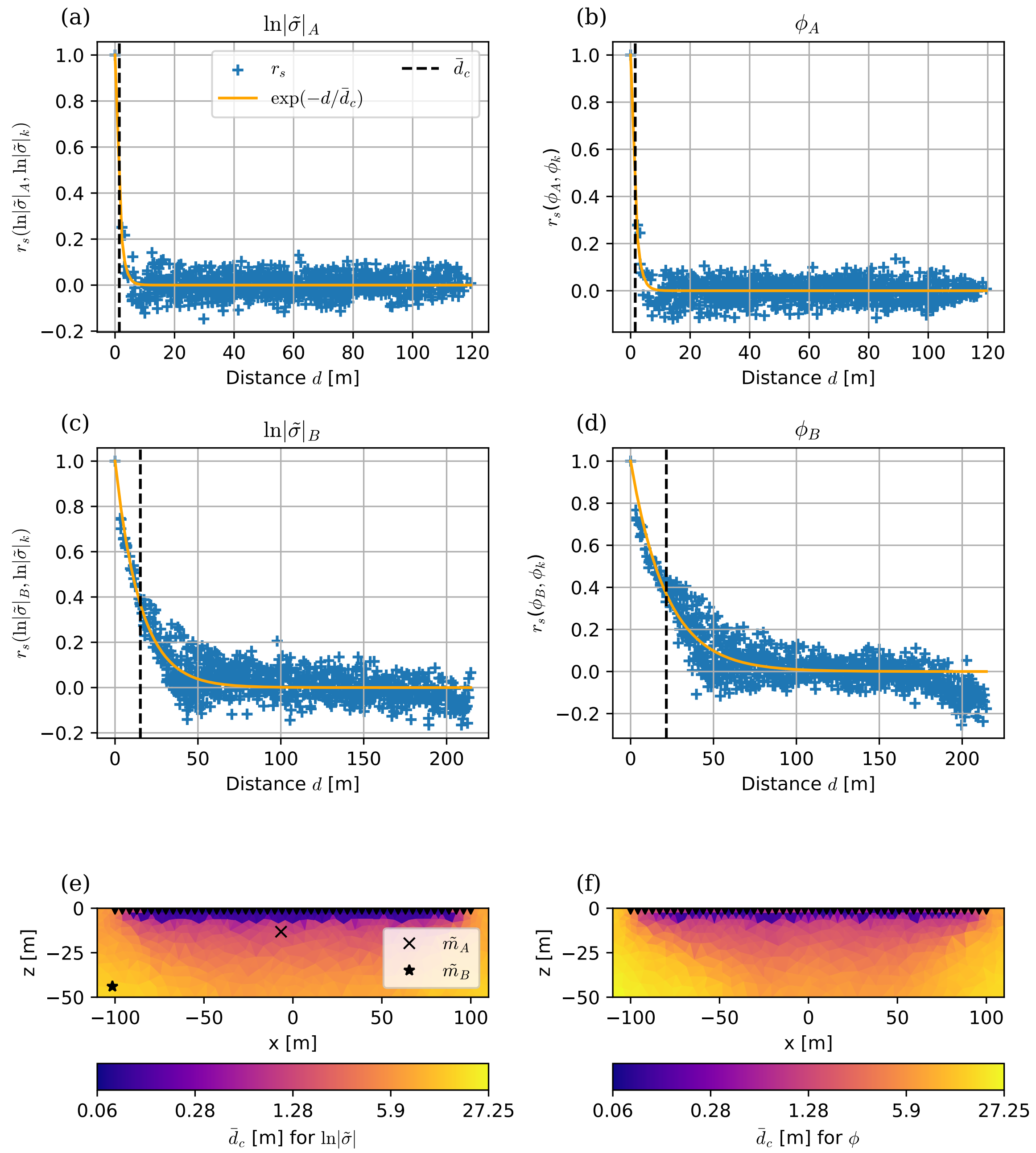

**Figure 5.6:** **(a, b, c, d)** Spearman correlation with respect to magnitude and phase of model parameters $\tilde{m}_\mathrm{A}$ and $\tilde{m}_\mathrm{B}$, plotted as a function of distance. Mean correlation distance for the conductivity magnitude **(e)** and phase **(f)**. The positions of the model parameters $\tilde{m}_\mathrm{A}$ and $\tilde{m}_\mathrm{B}$ are indicated in (e).

cases, the standard deviations are smaller in regions of high sensitivity and larger in regions of low sensitivity, which is consistent with expectations.

## 5.4 Discussion

In this work we use and analyze the posterior distribution introduced by Hase et al. (2024), which represents a probabilistic generalization of the established weighted-least squares for-

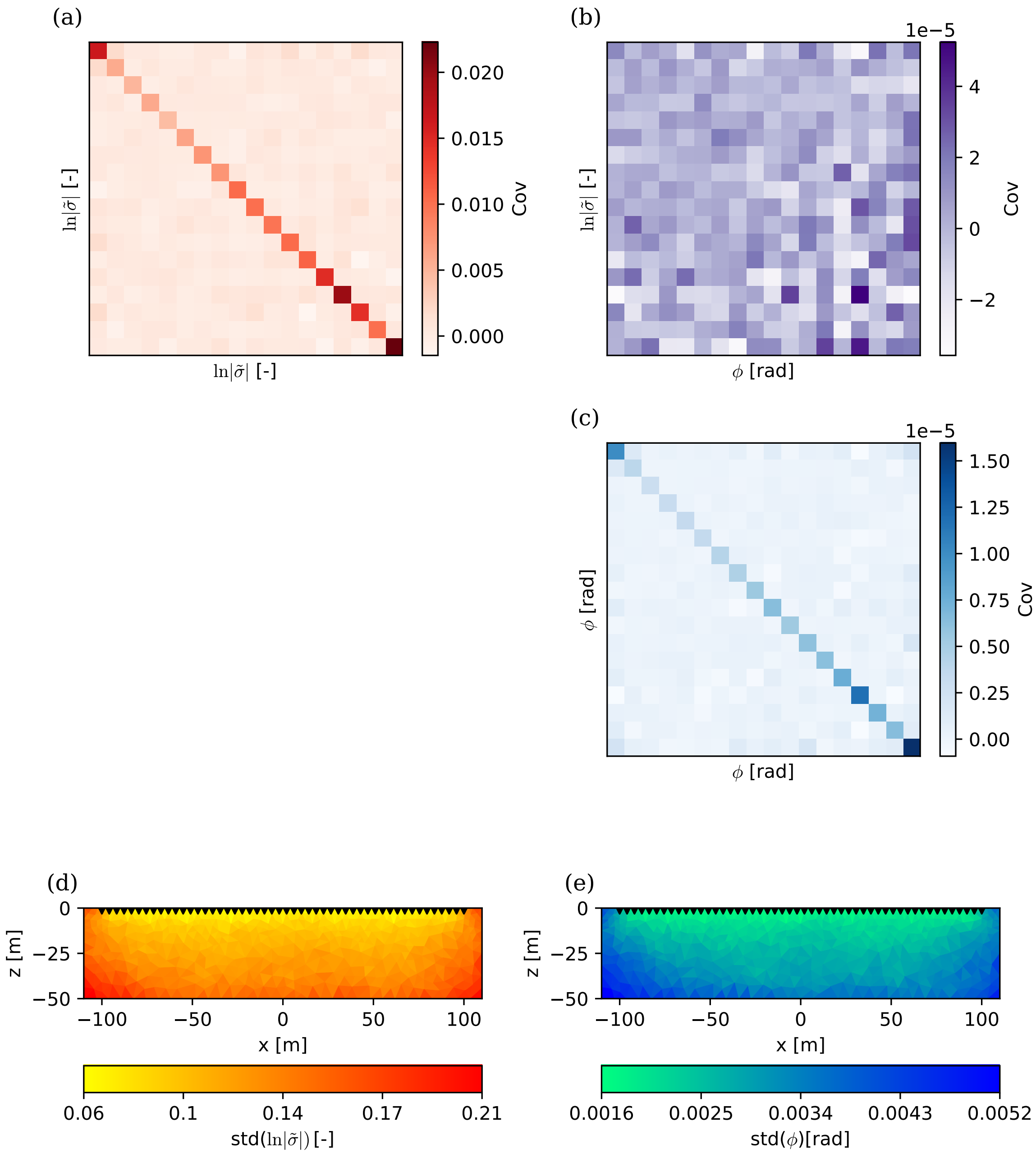

**Figure 5.7:** **(a)** Covariances of the conductivity magnitude. **(b)** Covariances between the conductivity magnitude and phase. **(c)** Covariances of the conductivity phase. In (a-c) only every 50th model parameter is shown, for reasons of readability. **(d, e)** Spatial distribution of standard deviations of the conductivity magnitude and phase.

mulation of the CR inverse problem described by Kemna (2000). It features a prior term that applies smoothing constraints to the inferred model, whose strengths are chosen for the MAP solution to achieve a reasonable data fit of RMSE $= 1$, as it is common practice in CR imaging. HMC is designed to accurately evaluate integral estimators of interest, such as the mean model, by generating a representative and unbiased sample of the posterior distribution, using a minimum number of model realizations. To accomplish this, HMC explores the typical set (Betancourt 2017) of the posterior distribution and generates model realizations associated with probabilities smaller than the probability of the MAP solution. For a random walk of limited length, the majority of the generated model realizations tend to under-fit the data and not minimize the overall model roughness. Furthermore, in case of a non-linear inverse problem, the mean model does not necessarily coincide with the MAP solution. Consequentially, it will also not necessarily fit the data adequately in the context of their uncertainties and not minimize the overall model roughness. As displayed in Figure 5.5, we found such deviations between the mean model and the MAP solution, indicating the influence of non-linearity resulting in a skewed posterior distribution. In practice we are often interested in the conductivity image that achieves a reasonable data fit in the context of measurement uncertainties, and defaults to the prior assumption where the information content in the measurement is not able to constrain the inverse problem. If this is the case, the MAP solution yields a more favorable conductivity image compared to the mean model, given the formulation of the posterior distribution and choice of regularization strengths used in this work. In light of the above, we want to emphasize the practical value of the deterministic inversion approach based on Gauss-Newton optimization used by Hase et al. (2024) in particular for CR imaging, and other deterministic and non-deterministic optimization approaches in general, as they are better suited to estimate the MAP solution compared to HMC and other McMC methods.

By generating an unbiased sample, HMC produces an inversion result that allows for an accurate evaluation of integral estimators like correlations, variances and covariances over the complete posterior distribution. In contrast to this, the information provided by the deterministic inversion is limited to the knowledge of the MAP solution. Given solely the deterministic inversion result, the posterior covariance matrix can therefore only be approximated locally under the simplifying assumption of normally distributed model parameters and a linearized forward calculation (e.g., Tarantola 2005):

$$\overset{c}{\mathbf{C}}_{\mathbf{m}} \approx \left( \overset{c}{\mathbf{G}}{}^{H}_{MAP} \overset{c}{\mathbf{R}}_{\mathbf{d}} \overset{c}{\mathbf{G}}_{MAP} + \overset{c}{\mathbf{R}}_{\mathbf{m}} \right)^{-1}, \tag{5.21}$$

where $\overset{c}{\mathbf{G}}_{MAP}$ is the Jacobian as estimated from the MAP solution. For linear inverse problems, where the posterior distribution is a normal distribution, Equation (5.21) gives the exact variances and covariances. Furthermore, the posterior distribution of a linear inverse problem is completely described by its mean and covariance matrix, which is not the case for non-linear inverse problems. In the following, we assess to which degree the local approximation of the posterior covariance matrix according to Equation (5.21) is representative of the true posterior covariance matrix, evaluated over the whole posterior distribution on the basis of the HMC inversion result. For the case investigated above, the results shown in Figure 5.8 suggest that the variances of the conductivity magnitude and phase estimated by HMC, and their approximations obtained according to Equation (5.21), are in good agreement with each other. In contrast to this, the covariances between the conductivity magnitude and the conductivity phase of the same model parameter are not approximated well, with Equation (5.21) significantly underestimating them by more than one order of magnitude. During our work, we observed the above to be a reoccurring result for varying subsurface geometries, data errors and measurement configurations. However, a dedicated parameter study, in which all underlying factors are identified and varied systematically, would be necessary to make clear statements with regard to the cause and systematic of the discrepancy between the two covariance estimates. Still, the results displayed in Figure 5.8 emphasize that Equation (5.21) does not provide a comprehensive uncertainty quantification to the degree that HMC does. If a given application requires an accurate estimation of the complete posterior covariance matrix, the results above encourage the use of HMC over a deterministic inversion approach.

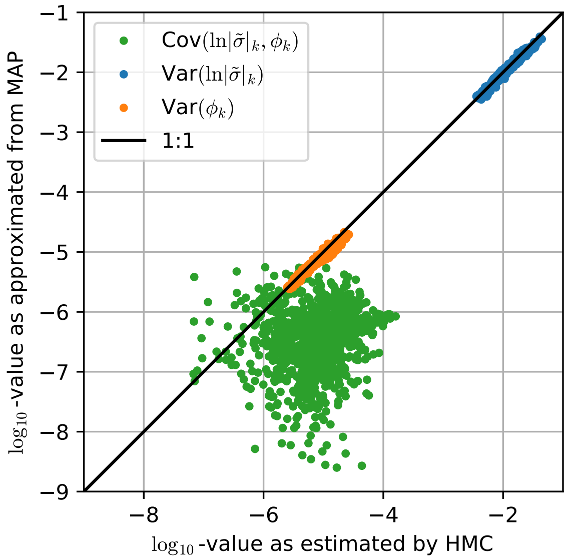

**Figure 5.8:** Scatter of the variances and covariances approximated according to Equation (5.21) against the variances and covariances estimated by HMC.

As with most McMC methods, the major limitation to the practical applicability of HMC is its computational demand. To generate the sample presented in this work, the NUTS performed 30 000 iterations. On average, 40 Leapfrog steps had to be carried out during each iteration. The majority of the total computation time can be attributed to the FEM-based forward calculation using pyGIMLi, the accumulation of which over the course of the complete random walk vastly outweighs the computation time required for the deterministic inversion. An acceleration of the forward calculation has the potential to drastically improve the applicability of HMC in practice. Besides optimization of the implementation, different methodological approaches could be pursued in future research. Aleardi et al. (2022) introduced a machine-learning accelerated McMC inversion approach for electrical resistivity tomography measurements, which avoids the necessity to evaluate the FEM solution of the Poisson equation for every forward calculation. This approach could possibly be extended to complex resistivity measurements. A different option might be the acceleration of the FE modeling by solving for the complex electrical potential distribution on a reduced parameter space (e.g., Cui et al. 2015).

A lot of attempts have been made to reduce the amount of hyperparameters that have to be specified explicitly before the application of HMC to a specific problem. Examples are the automatic tuning of the trajectory length using the NUTS (Hoffman et al. 2014), the automatic tuning of the mass matrix (Fichtner et al. 2021), and the dynamic choice of the time step used for the numerical integration of Hamilton's equations (Andrieu and Thoms 2008; Hoffman et al. 2014). Many of these automatic tuning schemes depend on certain hyperparameter choices themselves. The No-Free-Lunch theorem (e.g., Wolpert and Macready 1997) suggests that any involved hyperparameters must be tuned carefully to ensure the efficiency of HMC when applied to a specific problem, as the efficiency of any McMC method is not universal for all possible use cases. For CR imaging specifically, the degree to which hyperparameter choices are efficient across applications remains unknown at the moment. We are confident that with increased usage of HMC for CR imaging, best practices with regard to hyperparameter choices will evolve, thereby further increasing the applicability of the presented probabilistic inversion scheme. However, efficient hyperparameter choices might differ between different types of CR imaging problems, depending on the dimensionality of the setting (2D, 2.5D or 3D), the model parameterization, the survey setup and more.

## 5.5 Conclusion

We introduced the probabilistic inversion of complex resistivity measurements by means of HMC sampling, explicitly using the NUTS for the results presented above. The inversion operates on the posterior distribution introduced by Hase et al. (2024), which incorporates data errors and cross-sensitivities accurately, while also providing the ability to apply independent regularization to the conductivity magnitude and phase images. We adapted Hamilton's equations of motion, which underlie the model update in HMC, to the formulation of the probabilistic inverse problem in complex variables. In order to demonstrate the application, we performed a synthetic study. To scale the model proposal appropriately, considering the difference in orders of magnitude between the values associated with the conductivity magnitude and phase, we selected the mass matrix as an approximation of the Hessian near the MAP solution. Using the NUTS and automatic tuning of the step length, we achieved convergence of the generated sample, as suggested by evaluation of the PSRF. The resulting sample of the posterior distribution was analyzed with regard to the Spearman correlation between model parameters, yielding spatial patterns consistent with expectations. While the recovered mean model resolves all main features of the synthetic model used to generate the data set, it deviates from the synthetic model and the MAP solution obtained by the deterministic inversion in regions of low resolution, the implications of which we discussed. On the basis of the generated sample, we estimated the posterior covariance matrix over the complete posterior distribution to assess how the combined uncertainties of the measurements and prior information propagate into the uncertainties of the imaged conductivity magnitude and phase. The spatial distributions of the estimated standard deviations are consistent with expectations. Comparing the results provided by the HMC inversion to the uncertainties approximated on the basis of the limited information provided by the deterministic inversion, we found good agreement between the variance estimates for conductivity magnitude and phase. However, the covariances between the conductivity magnitude and phase of the same model parameter were underestimated significantly by the linearized approximation on the basis of the deterministic inversion. The accurate estimation of the complete posterior covariance matrix is essential, if the uncertainties of the imaged complex conductivity are propagated into uncertainty estimates for derived parameters of interest. An example would be the characterization of the hydraulic conductivity on the basis of single-frequency and multi-frequency CR measurements, using petrophysical relations between the complex conductivity and the geometry of the pore space. We conclude that HMC succeeds in performing the probabilistic inversion of CR measurements. It creates a converged sample, which provides a strong basis for the analysis of the posterior distribution and uncertainty quantification, thereby complementing and extending upon the established inversion approaches for CR imaging.

# CHAPTER 6

# Conclusions and future perspectives

## 6.1 Conclusions

Tomographic resistivity and induced polarization (IP) measurements continue to provide value in various emerging disciplines across earth sciences. To allow for a quantitative use of established relations between the macroscopic conduction and polarization characteristics of earth materials, and target properties during the interpretation of field measurements, this thesis made three main contributions, the key aspects of which are outlined below.

Chapter 3 introduced the accurate conversion of tomographic IP measurements from the time domain (TD) into the frequency domain (FD) by means of Debye decomposition (DD), enabling their quantitative analysis using complex resistivity (CR) imaging. The conversion uses a minimal amount of prior assumptions on the spectral characteristic of the IP measurement, inverting transients into smooth relaxation-time distributions (RTD) from which equivalent spectra can be calculated analytically. As a consequence, it achieves a superior degree of generalizability compared to other conversion and imaging approaches that assume the subsurface to exhibit CPA or Cole-Cole like polarization characteristics. The associated error propagation scheme isolates the propagated error of the IP transient by explicitly excluding the uncertainty of the prior characteristic introduced during the estimation of the RTD from the error propagation, which is kept small by following an Occam's approach during the choice of the applied regularization strength. During the subsequent imaging step of the analysis, the FD data points are therefore only weighted according to the propagated uncertainty of the measurement. The obtained FD uncertainty estimates follow established error models, confirming that the assumptions underlying the error propagation scheme are reasonable. Because every time domain transient is converted individually, the approach parallelizes very well and can be applied efficiently to large tomographic data sets. The application to tomographic field measurements was demonstrated on a data set from Kamchatka, Russia. Spectral information was extracted at frequencies of 1 Hz and 20 Hz, and the associated electrical impedances were inverted into subsurface images of complex electrical resistivity using the established deterministic inversion approach to CR imaging introduced by Kemna (2000).

Chapter 4 described a probabilistic framework for the solution of geophysical inverse problems in complex variables, explicitly formulating the likelihood and prior terms as complex probability distributions. Reducing to the weighted-least squares framework originally introduced by Kemna (2000) under simplifying assumptions with regard to data errors and regularization characteristics, the introduced framework represents a probabilistic generalization of the established inversion approach for CR measurements in complex variables, thereby providing valuable theoretical insight into its positioning in a probabilistic context. The extended mathematical formalism of the probabilistic framework ensures that available information on the individual impedance magnitude and phase errors is not lost during the inversion. Instead, it is accounted for accurately during the inference of the subsurface conductivity distribution and propagated into the uncertainty estimate of the solution. Furthermore, the probabilistic framework provides the possibility to balance the data uncertainties against individual regularization characteristics applied to the imaged conductivity magnitude and phase. This makes it possible to fit the complex data adequately in the context of their errors and allows for a higher flexibility in the formulation of the prior term. Both of these features allow for a more sophisticated model inference and uncertainty propagation, improving upon the established weighted-least squares framework. The probabilistic formulation is solved deterministically by means of Gauss-Newton optimization, accurately accounting for cross-sensitivities caused by the complex forward calculation and yielding a maximum a posteriori (MAP) solution with an appropriate data fit. While the optimization yields a good estimate of the MAP solution, it does not provide enough information to perform a global uncertainty quantification. Variances and covariances of the inferred model parameters can only be approximated locally under the simplifying assumption of a linearized forward operator and normally distributed model parameters in the vicinity of the MAP solution. Still, a demonstration of the probabilistic framework reveals the significantly improved local uncertainty quantification, compared to the established weighted-least squares framework.

To overcome the limitations of solving the probabilistic formulation described in Chapter 4 by means of optimization, Chapter 5 introduced the probabilistic geophysical inversion of CR measurements using Hamiltonian Monte Carlo (HMC) sampling. The objective of HMC is to achieve an accurate evaluation of integral estimators over the complete posterior distribution, with this thesis focusing on the estimation of the mean model, variances and covariances, as well as correlations between inferred model parameters. As the CR imaging problem is characterized by the non-linearity of the forward calculation, its high dimension and strong correlations between model parameters, efficiently sampling from the posterior distribution is challenging. HMC incorporates the sensitivity information available for the inversion of CR measurements to efficiently sample from the posterior distribution. By using a variant of HMC called the No-U-Turn sampler, the benefit of a given number of forward calculations is maximized. An adjusted mass matrix accounts for the different scales of the complex conductivity's magnitude and phase, stabilizing the model update. When applying the probabilistic inversion approach to a tomographic set of CR measurements, we achieved convergence of the generated sample. The mean model deviates from the MAP solution estimated by the deterministic inversion according to Chapter 4 in regions of low resolution, yielding a larger data misfit and model roughness, and indicating the influence of non-linearity leading to a skewed posterior distribution. Within the limited length of the random walk performed by HMC, no model realization was generated that minimizes the data misfit and model roughness equally well as the MAP solution. While this is to be expected, it emphasizes the practical value of optimization approaches in geophysical inversion, as the efficient estimation of the subsurface image corresponding to the MAP solution is often of high practical interest. Covariances and correlations exhibit spatial patterns that are consistent with expectations, indicating the validity of the employed approach. A comparison of the uncertainties approximated by the deterministic inversion to the uncertainties estimated by HMC demonstrated the inability of the deterministic approach to accurately estimate the complete posterior covariance matrix. Given these findings, it is recommended that global sampling methods, such as HMC, be employed when an accurate uncertainty quantification is essential for a given application. Therefore, we conclude that the inversion approaches introduced in Chapter 4 and Chapter 5 complement each other in the objective of characterizing the posterior distribution.

Together, the three parts of this thesis contribute to the goal of improved model inference and uncertainty quantification for the analysis of tomographic IP measurements by means of CR imaging, enhancing the quantitative diagnostic potential of the IP method. The contributions allow for an improved quantitative interpretability of derived complex conductivity images using established relationships with target parameters, while the improved uncertainty quantification provides a basis for a reliable assessment of the validity of the conclusions drawn.

## 6.2 Future research perspectives

The role of applied geophysics is to provide quantitative information on the state of the subsurface, and the processes that control its change over time, to other earth scientists, engineers and decision makers. Within this context, the interpretability of results is critically dependent on the accuracy of the inferred subsurface images, as well as on an adequate uncertainty quantification. This thesis contributed to three different aspects of the CR imaging problem. Below, the key limitations are outlined, followed by an overview of possible directions for future research to improve upon them.

The first aspect is the accurate conversion of tomographic TD IP measurements into the FD, to enable their analysis by means of CR imaging. Chapter 3 introduced a deterministic approach, based on the DD, that uses heuristics to determine appropriate hyperparameter choices. While the error propagation scheme was validated using a synthetic study, it relies on a local and linear approximation of the underling relations, and is therefore not exact.

The second aspect is the formalization of the CR imaging problem within a probabilistic inversion framework, introduced in Chapter 4. The probabilistic framework accounts for two main sources of uncertainty, namely stochastic data errors and the uncertainty associated with the prior. Other sources of uncertainty, stemming from choices made with regard to the design of the forward operator, the model parameterization, and the measurement setup, are disregarded. Consequentially, their effects are not reflected in the uncertainty estimate of the solution.

Chapter 5 covered the estimation of global uncertainties by means of McMC sampling, representing the third aspect addressed within this thesis. Here, the quality of the numerically obtained uncertainty estimates is limited by the effective size of the sample, which is proportional to the number of uncorrelated realizations that have been generated during the random walk. For the presented results, the runtime of the probabilistic inversion was considerable, spanning multiple days to ensure approximate convergence of the generated sample. More efficient sampling schemes may further increase the accuracy of the uncertainty estimate and improve the applicability of the overall approach.

With regard to the introduced conversion approach for IP measurements from TD to FD, future research should investigate possibilities to improve the error propagation by implementing the DD in a probabilistic framework and performing the error propagation numerically by means of McMC sampling. The DD has been previously realized using probabilistic frameworks, for example by Bérubé et al. (2017), who employed the Metropolis-Hastings (MH) method. However, for the parameterization of the relaxation-time distribution, they used a polynomial approximation. The associated reduction in model-space dimension simplifies the application of the MH method, but comes at the cost of a reduced generalizability, compared to a regularized approach like the one taken in Chapter 3 of this thesis. Compared to deterministic methods, the solution of high dimensional inverse problems, such as the regularized DD, by means of McMC methods is typically associated with an increased computational cost, possibly rendering their application to the conversion of tomographic datasets comprised of numerous transients unpractical. Furthermore, it remains to be investigated how the dynamic adaptation of the regularization strength can be realized explicitly in a probabilistic framework, and how the propagation of the data error can be isolated. Nevertheless, using a probabilistic formulation could help to integrate the conversion approach described in Chapter 3 more consistently with the probabilistic imaging step discussed in Chapters 4 and 5.

The accurate numerical characterization of the posterior distribution offers insight into the manner in which the known aleatoric uncertainties of the data and prior propagate into the uncertainty of the inferred complex conductivity image. Given the mathematical formalism introduced in Chapter 4, the propagation of these uncertainties is limited only by the ability to efficiently characterize the posterior distribution. Consequentially, future research should focus on the development and application of more technically sophisticated optimization methods and sampling schemes. An accurate, unbiased and efficient evaluation of the propagated uncertainties by means of HMC sampling is restricted by the computational cost of the method, most of which can be attributed to the necessity of evaluating the forward response multiple times during each proposal step. As the evaluation of the forward response dominates the total computational effort of the HMC inversion, the runtime could be drastically reduced by accelerating the solution of the forward problem. As discussed in Chapter 5, this may be achieved by solving the forward and inverse problem on a reduced parameter space (e.g., Cui et al. 2015), or by employing an accelerated machine-learning based approximation of the forward calculation (e.g., Aleardi et al. 2022). A reduced runtime would also improve the overall applicability of the method, especially with respect to use cases in which time is a critical factor, like monitoring applications.

While the accurate propagation of uncertainties associated with the data and the prior on the complex conductivity image is a key challenge, there are many sources of epistemic uncertainty associated with the tomographic inversion of IP measurements that are not considered by the mathematical formalism described in Chapters 4 and 5 of this thesis. These include choices made with regard to the design of the forward operator, the model parameterization and measurement setup, the hyperparameters of the error models describing the data uncertainties, as well as the assumed prior characteristics themselves. Future research should continue to identify relevant sources of uncertainty and quantify their characteristics, thereby building a basis from which to proceed with their incorporation into the mathematical formalism. If a specific source of uncertainty is understood and can be quantitatively described in a meaningful way, it can make sense to carefully account for it in an extended formulation of the probabilistic inverse problem, in order to propagate its effect into the solution.

An extended formulation of the probabilistic inverse problem can take the form of a hierarchical posterior distribution, which may include hyperparameters as additional random variables that are to be inferred. The benefits of using an extended formulation, that accounts for additional sources of uncertainty, have to be balanced against the drawbacks due to the added degrees of freedom. These degrees of freedom have to be constraint by information in the data, or by additional independent prior information. Blatter et al. (2022) use a hierarchical approach for the inversion of electromagnetic data, incorporating the regularization strength as a random variable into the inversion process. Other researchers have used hierarchical posterior distributions to allow for variability in the parameterization of the model domain, especially with regard to the discretization of the subsurface (e.g., Bodin et al. 2009), and to account for uncertainties associated with the chosen hyperparameters of error models (e.g., Bodin et al. 2012) (compare Equations (4.34) and (4.35)).

To qualitatively assess the uncertainty associated with the choice of the prior, evaluating equivalent solutions of the CR imaging problem for different, equally plausible, prior assumptions might help to communicate uncertainties and promote a more robust interpretation of the results. A variational-inference based approach that could be employed for this purpose was described recently by Zhao and Curtis (2024), who demonstrated how prior assumptions could be exchanged within an existing approximation of a posterior distribution, without the need to reevaluate the full solution. For a given CR imaging result, equivalent complex conductivity images may also be constructed using methods of qualitative nullspace exploration. To achieve this, the concepts underlying the HMC method (compare Chapter 5) can be adapted to construct models from the effective nullspace in a systematic manner (Fichtner and Zunino 2019; Giraud et al. 2024).

Finally, it is a non-trivial problem how to communicate obtained uncertainty estimates to users and decision makers. While the spatial distribution of estimators like the variance can help to assess the validity of certain results, their implications with regard to specific interpretations are often not intuitive to grasp. Future research should explore methods to communicate uncertainty efficiently to users from other scientific fields, and to make results more usable in general, so that the insights gained from IP measurements can continue to provide value across earth sciences.

# References

Abadi, M., Agarwal, A., Barham, P., Brevdo, E., Chen, Z., Citro, C., Corrado, G. S., Davis, A., Dean, J., Devin, M., Ghemawat, S., Goodfellow, I., Harp, A., Irving, G., Isard, M., Jia, Y., Jozefowicz, R., Kaiser, L., Kudlur, M., Levenberg, J., Mané, D., Monga, R., Moore, S., Murray, D., Olah, C., Schuster, M., Shlens, J., Steiner, B., Sutskever, I., Talwar, K., Tucker, P., Vanhoucke, V., Vasudevan, V., Viégas, F., Vinyals, O., Warden, P., Wattenberg, M., Wicke, M., Yu, Y., and Zheng, X.: TensorFlow: Large-Scale Machine Learning on Heterogeneous Systems, URL `https://www.tensorflow.org/`, software available from tensorflow.org, 2015.

Aleardi, M. and Salusti, A.: Hamiltonian Monte Carlo algorithms for target- and interval-oriented amplitude versus angle inversions, Geophysics, 85, R177–R194, https://doi.org/10.1190/geo2019-0517.1, 2020.

Aleardi, M., Vinciguerra, A., Stucchi, E., and Hojat, A.: Machine learning-accelerated gradient-based Markov chain Monte Carlo inversion applied to electrical resistivity tomography, Near Surface Geophysics, 20, 440–461, https://doi.org/10.1002/nsg.12211, 2022.

Andersen, K. E., Brooks, S. P., and Hansen, M. B.: Bayesian inversion of geoelectrical resistivity data, Journal of the Royal Statistical Society Series B: Statistical Methodology, 65, 619–642, https://doi.org/10.1111/1467-9868.00406, 2003.

Andrieu, C. and Thoms, J.: A tutorial on adaptive MCMC, Statistics and computing, 18, 343–373, https://doi.org/10.1007/s11222-008-9110-y, 2008.

Archie, G. E.: The electrical resistivity log as an aid in determining some reservoir characteristics, Transactions of the AIME, 146, 54–62, https://doi.org/10.2118/942054-G, 1942.

Attwa, M. and Günther, T.: Spectral induced polarization measurements for predicting the hydraulic conductivity in sandy aquifers, Hydrology and Earth System Sciences, 17, 4079–4094, https://doi.org/10.5194/hess-17-4079-2013, 2013.

Bardsley, J. M., Solonen, A., Haario, H., and Laine, M.: Randomize-then-optimize: A method for sampling from posterior distributions in nonlinear inverse problems, SIAM Journal on Scientific Computing, 36, A1895–A1910, https://doi.org/10.1137/140964023, 2014.

Bayes, T.: LII. An essay towards solving a problem in the doctrine of chances. By the late Rev. Mr. Bayes, FRS communicated by Mr. Price, in a letter to John Canton, AMFR S, Philosophical transactions of the Royal Society of London, pp. 370–418, https://doi.org/10.1098/rstl.1763.0053, 1763.

Bérubé, C. L., Chouteau, M., Shamsipour, P., Enkin, R. J., and Olivo, G. R.: Bayesian inference of spectral induced polarization parameters for laboratory complex resistivity measurements of rocks and soils, Computers & Geosciences, 105, 51–64, https://doi.org/10.1016/j.cageo.2017.05.001, 2017.

Betancourt, M.: A conceptual introduction to Hamiltonian Monte Carlo, arXiv preprint arXiv:1701.02434, https://doi.org/10.48550/arXiv.1701.02434, 2017.

Binley, A. and Slater, L.: Resistivity and induced polarization: Theory and applications to the near-surface earth, Cambridge University Press, 2020.

Binley, A., Slater, L. D., Fukes, M., and Cassiani, G.: Relationship between spectral induced polarization and hydraulic properties of saturated and unsaturated sandstone, Water resources research, 41, https://doi.org/10.1029/2005WR004202, 2005.

Binley, A., Keery, J., Slater, L., Barrash, W., and Cardiff, M.: The hydrogeologic information in cross-borehole complex conductivity data from an unconsolidated conglomeratic sedimentary aquifer, Geophysics, 81, E409–E421, https://doi.org/10.1190/geo2015-0608.1, 2016.

Bishop, C. M.: Pattern recognition and machine learning, Springer, 2006.

Blatter, D., Morzfeld, M., Key, K., and Constable, S.: Uncertainty quantification for regularized inversion of electromagnetic geophysical data—Part I: motivation and theory, Geophysical Journal International, 231, 1057–1074, https://doi.org/10.1093/gji/ggac241, 2022.

Bleil, D. F.: Induced polarization: A method of geophysical prospecting, Geophysics, 18, 636–661, https://doi.org/10.1190/1.1437917, 1953.

Bodin, T., Sambridge, M., and Gallagher, K.: A self-parametrizing partition model approach to tomographic inverse problems, Inverse Problems, 25, 055 009, https://doi.org/10.1088/0266-5611/25/5/055009, 2009.

Bodin, T., Sambridge, M., Rawlinson, N., and Arroucau, P.: Transdimensional tomography with unknown data noise, Geophysical Journal International, 189, 1536–1556, https://doi.org/10.1111/j.1365-246X.2012.05414.x, 2012.

Börner, F., Schopper, J., and Weller, A.: Evaluation of transport and storage properties in the soil and groundwater zone from induced polarization measurements, Geophysical prospecting, 44, 583–601, https://doi.org/10.1111/j.1365-2478.1996.tb00167.x, 1996.

Börner, F. D. and Schon, J. H.: A relation between the quadrature component of electrical conductivity and the specific surface area of sedimentary rocks, The Log Analyst, 32, 1991.

Brooks, S. P. and Gelman, A.: General methods for monitoring convergence of iterative simulations, Journal of computational and graphical statistics, 7, 434–455, https://doi.org/10.1080/10618600.1998.10474787, 1998.

Bücker, M. B.: Pore-scale modelling of induced-polarization mechanisms in geologic materials, Ph.D. thesis, Universitäts-und Landesbibliothek Bonn, 2019.

Carter, S., Xie, X., Zhou, L., and Yan, L.: Hybrid Monte Carlo 1-D joint inversion of LOTEM and MT, Journal of Applied Geophysics, 194, 104 424, https://doi.org/10.1016/j.jappgeo.2021.104424, 2021.

Caterina, D., Orozco, A. F., and Nguyen, F.: Long-term ERT monitoring of biogeochemical changes of an aged hydrocarbon contamination, Journal of contaminant hydrology, 201, 19–29, https://doi.org/10.1016/j.jconhyd.2017.04.003, 2017.

Cole, K. S. and Cole, R. H.: Dispersion and absorption in dielectrics I. Alternating current characteristics, The Journal of chemical physics, 9, 341–351, https://doi.org/10.1063/1.1750906, 1941.

Cowles, M. K. and Carlin, B. P.: Markov chain Monte Carlo convergence diagnostics: a comparative review, Journal of the American statistical Association, 91, 883–904, https://doi.org/10.1080/01621459.1996.10476956, 1996.

Cui, T., Marzouk, Y. M., and Willcox, K. E.: Data-driven model reduction for the Bayesian solution of inverse problems, International Journal for Numerical Methods in Engineering, 102, 966–990, https://doi.org/10.1002/nme.4748, 2015.

Dahlin, T. and Loke, M. H.: Negative apparent chargeability in time-domain induced polarisation data, Journal of Applied Geophysics, 123, 322–332, https://doi.org/10.1016/j.jappgeo.2015.08.012, 2015.

Datta, D. and Sen, M. K.: Estimating a starting model for full-waveform inversion using a global optimization method, Geophysics, 81, R211–R223, https://doi.org/10.1190/geo2015-0339.1, 2016.

Dębski, W.: Seismic tomography by Monte Carlo sampling, Pure and applied geophysics, 167, 131–152, https://doi.org/10.1007/s00024-009-0006-3, 2010.

de Lima, P. D. S., Corso, G., Ferreira, M. S., and de Araújo, J. M.: Acoustic full waveform inversion with Hamiltonian Monte Carlo method, Physica A: Statistical Mechanics and its Applications, 617, 128 618, https://doi.org/10.1016/j.physa.2023.128618, 2023.

De Pasquale, G., Linde, N., Doetsch, J., and Holbrook, W. S.: Probabilistic inference of subsurface heterogeneity and interface geometry using geophysical data, Geophysical Journal International, 217, 816–831, https://doi.org/10.1093/gji/ggz055, 2019.

Debye, P. J. W.: Polar molecules, Dover publications, 1929.

deGroot Hedlin, C. and Constable, S.: Occam's inversion to generate smooth, two-dimensional models from magnetotelluric data, Geophysics, 55, 1613–1624, https://doi.org/10.1190/1.1442813, 1990.

Deng, S., Zhang, N., Kuang, B., Li, Y., and Sun, H.: Bayesian Markov Chain Monte Carlo inversion of surface-based transient electromagnetic data, SN Applied Sciences, 4, 254, https://doi.org/10.1007/s42452-022-05134-5, 2022.

Dhabaria, N. and Singh, S. C.: Hamiltonian Monte Carlo based elastic full-waveform inversion of wide-angle seismic data, Geophysical Journal International, 237, 1384–1399, https://doi.org/10.1093/gji/ggae112, 2024.

Ehosioke, S., Nguyen, F., Rao, S., Kremer, T., Placencia-Gomez, E., Huisman, J. A., Kemna, A., Javaux, M., and Garré, S.: Sensing the electrical properties of roots: A review, Vadose Zone Journal, 19, e20 082, https://doi.org/10.1002/vzj2.20082, 2020.

Everett, M. E.: Near-surface applied geophysics, Cambridge University Press, 2013.

Fiandaca, G., Auken, E., Christiansen, A. V., and Gazoty, A.: Time-domain-induced polarization: Full-decay forward modeling and 1D laterally constrained inversion of Cole-Cole parameters, Geophysics, 77, E213–E225, https://doi.org/10.1190/geo2011-0217.1, 2012.

Fiandaca, G., Ramm, J., Binley, A., Gazoty, A., Christiansen, A. V., and Auken, E.: Resolving spectral information from time domain induced polarization data through 2-D inversion, Geophysical Journal International, 192, 631–646, https://doi.org/10.1093/gji/ggs060, 2013.

Fichtner, A. and Zunino, A.: Hamiltonian nullspace shuttles, Geophysical research letters, 46, 644–651, https://doi.org/10.1029/2018GL080931, 2019.

Fichtner, A., Zunino, A., and Gebraad, L.: Hamiltonian Monte Carlo solution of tomographic inverse problems, Geophysical Journal International, 216, 1344–1363, https://doi.org/10.1093/gji/ggy496, 2019.

Fichtner, A., Zunino, A., Gebraad, L., and Boehm, C.: Autotuning Hamiltonian Monte Carlo for efficient generalized nullspace exploration, Geophysical Journal International, 227, 941–968, https://doi.org/10.1093/gji/ggab270, 2021.

Flores Orozco, A., Williams, K. H., Long, P. E., Hubbard, S. S., and Kemna, A.: Using complex resistivity imaging to infer biogeochemical processes associated with bioremediation of an uranium-contaminated aquifer, Journal of Geophysical Research: Biogeosciences, 116, https://doi.org/10.1029/2010JG001591, 2011.

Flores Orozco, A., Kemna, A., Oberdörster, C., Zschornack, L., Leven, C., Dietrich, P., and Weiss, H.: Delineation of subsurface hydrocarbon contamination at a former hydrogenation plant using spectral induced polarization imaging, Journal of contaminant hydrology, 136, 131–144, https://doi.org/10.1016/j.jconhyd.2012.06.001, 2012a.

Flores Orozco, A., Kemna, A., and Zimmermann, E.: Data error quantification in spectral induced polarization imaging, Geophysics, 77, E227–E237, https://doi.org/10.1190/geo2010-0194.1, 2012b.

Flores Orozco, A., Bücker, M., Steiner, M., and Malet, J.-P.: Complex-conductivity imaging for the understanding of landslide architecture, Engineering geology, 243, 241–252, https://doi.org/10.1016/j.enggeo.2018.07.009, 2018a.

Flores Orozco, A., Gallistl, J., Bücker, M., and Williams, K. H.: Decay curve analysis for data error quantification in time-domain induced polarization imaging, Geophysics, 83, E75–E86, https://doi.org/10.1190/geo2016-0714.1, 2018b.

Gao, Z., Yang, W., Tian, Y., Li, C., Jiang, X., Gao, J., and Xu, Z.: Global optimization with deep-learning-based acceleration surrogate for large-scale seismic acoustic-impedance inversion, Geophysics, 87, R35–R51, https://doi.org/10.1190/geo2021-0070.1, 2022.

Gebraad, L., Boehm, C., and Fichtner, A.: Bayesian elastic full-waveform inversion using Hamiltonian Monte Carlo, Journal of Geophysical Research: Solid Earth, 125, e2019JB018 428, https://doi.org/10.1029/2019JB018428, 2020.

Gelman, A. and Rubin, D. B.: Inference from iterative simulation using multiple sequences, Statistical science, 7, 457–472, https://doi.org/10.1214/ss/1177011136, 1992.

Geyer, C. J.: Practical markov chain monte carlo, Statistical science, pp. 473–483, https://doi.org/10.1214/ss/1177011137, 1992.

Giraud, J., Ford, M., Caumon, G., Ogarko, V., Grose, L., Martin, R., and Cupillard, P.: Geologically constrained geometry inversion and null-space navigation to explore alternative geological scenarios: a case study in the Western Pyrenees, Geophysical Journal International, 239, ggae192, https://doi.org/10.1093/gji/ggae192, 2024.

Griffiths, D. and Barker, R.: Electrical imaging in archaeology, Journal of Archaeological science, 21, 153–158, https://doi.org/10.1006/jasc.1994.1017, 1994.

Grünenbaum, N., Günther, T., Greskowiak, J., Vienken, T., Müller-Petke, M., and Massmann, G.: Salinity distribution in the subterranean estuary of a meso-tidal high-energy beach characterized by electrical resistivity tomography and direct push technology, Journal of Hydrology, 617, 129 074, https://doi.org/10.1016/j.jhydrol.2023.129074, 2023.

Gubbins, D.: Time series analysis and inverse theory for geophysicists, Cambridge University Press, https://doi.org/10.1017/CBO9780511840302, 2004.

Gurin, G.: Geophysical prospecting for epithermal gold deposits (a case study from the Maletoivayam gold ore field, Kamchatka Peninsula), Lithosphere (Russia), 21, 116–132, https://doi.org/10.24930/1681-9004-2021-21-1-116-132, 2021.

Gurin, G., Tarasov, A., Ilyin, Y., and Titov, K.: Time domain spectral induced polarization of disseminated electronic conductors: Laboratory data analysis through the Debye decomposition approach, Journal of Applied Geophysics, 98, 44–53, https://doi.org/10.1016/j.jappgeo.2013.07.008, 2013.

Gurin, G., Tarasov, A., and Titov, K.: Analysis of Transient Characteristics of Induced Polarization in Innovative Mineral Exploration Solutions (from Case Studies of Gold Deposits), Russian Geology and Geophysics, 64, 348–356, https://doi.org/10.2113/RGG20224477, 2023.

Hallof, P. G.: A comparison of the various parameters employed in the variable-frequency induced-polarization method, Geophysics, 29, 425–433, https://doi.org/10.1190/1.1439376, 1964.

Hase, J., Weigand, M., and Kemna, A.: A probabilistic solution to geophysical inverse problems in complex variables and its application to complex resistivity imaging, Geophysical Journal International, p. ggae045, https://doi.org/10.1093/gji/ggae045, 2024.

Hastings, W. K.: Monte Carlo sampling methods using Markov chains and their applications, Biometrika, 57, https://doi.org/10.1093/biomet/57.1.97, 1970.

Herring, T., Lewkowicz, A. G., Hauck, C., Hilbich, C., Mollaret, C., Oldenborger, G. A., Uhlemann, S., Farzamian, M., Calmels, F., and Scandroglio, R.: Best practices for using electrical resistivity tomography to investigate permafrost, Permafrost and Periglacial Processes, 34, 494–512, https://doi.org/10.1002/ppp.2207, 2023.

Hoffman, M. D., Gelman, A., et al.: The No-U-Turn sampler: Adaptively setting path lengths in Hamiltonian Monte Carlo., J. Mach. Learn. Res., 15, 1593–1623, https://doi.org/10.48550/arXiv.1111.4246, 2014.

Hönig, M. and Tezkan, B.: 1D and 2D Cole-Cole-inversion of time-domain induced-polarization data, Geophysical Prospecting, 55, 117–133, https://doi.org/10.1111/j.1365-2478.2006.00570.x, 2007.

Hördt, A., Hanstein, T., Hönig, M., and Neubauer, F. M.: Efficient spectral IP-modelling in the time domain, Journal of Applied Geophysics, 59, 152–161, https://doi.org/10.1016/j.jappgeo.2005.09.003, 2006.

Hördt, A., Blaschek, R., Kemna, A., and Zisser, N.: Hydraulic conductivity estimation from induced polarisation data at the field scale—the Krauthausen case history, Journal of Applied Geophysics, 62, 33–46, https://doi.org/10.1016/j.jappgeo.2006.08.001, 2007.

Johnson, T. C. and Thomle, J.: 3-D decoupled inversion of complex conductivity data in the real number domain, Geophysical Journal International, 212, 284–296, https://doi.org/10.1093/gji/ggx416, 2018.

Jordi, C., Doetsch, J., Günther, T., Schmelzbach, C., and Robertsson, J. O.: Geostatistical regularization operators for geophysical inverse problems on irregular meshes, Geophysical Journal International, 213, 1374–1386, https://doi.org/10.1093/gji/ggy055, 2018.

Kaipio, J. P., Kolehmainen, V., Somersalo, E., and Vauhkonen, M.: Statistical inversion and Monte Carlo sampling methods in electrical impedance tomography, Inverse problems, 16, 1487, https://doi.org/10.1088/0266-5611/16/5/321, 2000.

Keilis-Borok, V. and Yanovskaja, T.: Inverse problems of seismology (structural review), Geophysical Journal International, 13, 223–234, https://doi.org/10.1111/j.1365-246X.1967.tb02156.x, 1967.

Kemna, A.: Tomographic inversion of complex resistivity: Theory and application, PhD thesis Ruhr Universität Bochum, 2000.

Kemna, A., Räkers, E., and Binley, A.: Application of complex resistivity tomography to field data from a kerosene-contaminated site, in: 3rd EEGS Meeting, pp. cp–95, EAGE Publications BV, https://doi.org/10.3997/2214-4609.201407300, 1997.

Kemna, A., Binley, A., Ramirez, A., and Daily, W.: Complex resistivity tomography for environmental applications, Chemical Engineering Journal, 77, 11–18, https://doi.org/10.1016/S1385-8947(99)00135-7, 2000.

Kemna, A., Binley, A., and Slater, L.: Crosshole IP imaging for engineering and environmental applications, Geophysics, 69, 97–107, https://doi.org/10.1190/1.1649379, 2004.

Kemna, A., Binley, A., Cassiani, G., Niederleithinger, E., Revil, A., Slater, L., Williams, K. H., Orozco, A. F., Haegel, F.-H., Hördt, A., et al.: An overview of the spectral induced polarization method for near-surface applications, Near Surface Geophysics, 10, 453–468, https://doi.org/10.3997/1873-0604.2012027, 2012.

Kenkel, J., Hördt, A., and Kemna, A.: 2D modelling of induced polarization data with anisotropic complex conductivities, Near Surface Geophysics, 10, 533–544, https://doi.org/10.3997/1873-0604.2012050, 2012.

Kneisel, C., Hauck, C., Fortier, R., and Moorman, B.: Advances in geophysical methods for permafrost investigations, Permafrost and periglacial processes, 19, 157–178, https://doi.org/10.1002/ppp.616, 2008.

Knödel, K., Krummel, H., and Lange, G.: Handbuch zur Erkundung des Untergrundes von Deponien und Altlasten: Band 3: Geophysik, Springer-Verlag, 2013.

Koestel, J., Kemna, A., Javaux, M., Binley, A., and Vereecken, H.: Quantitative imaging of solute transport in an unsaturated and undisturbed soil monolith with 3-D ERT and TDR, Water resources research, 44, https://doi.org/10.1029/2007WR006755, 2008.

Krautblatter, M., Verleysdonk, S., Flores-Orozco, A., and Kemna, A.: Temperature-calibrated imaging of seasonal changes in permafrost rock walls by quantitative electrical resistivity tomography (Zugspitze, German/Austrian Alps), Journal of Geophysical Research: Earth Surface, 115, https://doi.org/10.1029/2008JF001209, 2010.

Kreutz-Delgado, K.: The complex gradient operator and the CR-calculus, arXiv preprint arXiv:0906.4835, https://doi.org/10.48550/arXiv.0906.4835, 2009.

Kumar, I., Kumar, B. V., Babu, R. V., Dash, J. K., and Chaturvedi, A. K.: Relaxation time distribution approach of mineral discrimination from time domain-induced polarisation data, Exploration Geophysics, 50, 337–350, https://doi.org/10.1080/08123985.2019.1606198, 2019.

LaBrecque, D. J., Miletto, M., Daily, W., Ramirez, A., and Owen, E.: The effects of noise on Occam's inversion of resistivity tomography data, Geophysics, 61, 538–548, https://doi.org/10.1190/1.1443980, 1996.

Limbrock, J. K. and Kemna, A.: Relationship between Cole–Cole model parameters in permittivity and conductivity formulation, Geophysical Journal International, 239, 964–970, https://doi.org/10.1093/gji/ggae300, 2024.

Maierhofer, T., Hauck, C., Hilbich, C., Kemna, A., and Flores-Orozco, A.: Spectral induced polarization imaging to investigate an ice-rich mountain permafrost site in Switzerland, The Cryosphere, 16, 1903–1925, https://doi.org/10.5194/tc-16-1903-2022, 2022.

Marshall, D. J. and Madden, T. R.: Induced polarization, a study of its causes, Geophysics, 24, 790–816, https://doi.org/10.1190/1.1438659, 1959.

Martin, T. and Günther, T.: Complex resistivity tomography (CRT) for fungus detection on standing oak trees, European Journal of Forest Research, 132, 765–776, https://doi.org/10.1007/s10342-013-0711-4, 2013.

Martin, T., Titov, K., Tarasov, A., and Weller, A.: Spectral induced polarization: frequency domain versus time domain laboratory data, Geophysical Journal International, 225, 1982–2000, https://doi.org/10.1093/gji/ggab071, 2021.

Martin, T., Weller, A., and Behling, L.: Desaturation effects of pyrite–sand mixtures on induced polarization signals, Geophysical Journal International, 228, 275–290, https://doi.org/10.1093/gji/ggab333, 2022.

Maurer, H., Holliger, K., and Boerner, D. E.: Stochastic regularization: Smoothness or similarity?, Geophysical Research Letters, 25, 2889–2892, https://doi.org/10.1029/98GL02183, 1998.

Metropolis, N., Rosenbluth, A. W., Rosenbluth, M. N., Teller, A. H., and Teller, E.: Equation of state calculations by fast computing machines, The journal of chemical physics, 21, 1087–1092, https://doi.org/10.1063/1.1699114, 1953.

Minsley, B. J.: A trans-dimensional Bayesian Markov chain Monte Carlo algorithm for model assessment using frequency-domain electromagnetic data, Geophysical Journal International, 187, 252–272, https://doi.org/10.1111/j.1365-246X.2011.05165.x, 2011.

Moreira, C. A., Paes, R. A. S., Ilha, L. M., and da Cruz Bittencourt, J.: Reassessment of copper mineral occurrence through electrical tomography and pseudo 3D modeling in Camaquã Sedimentary Basin, Southern Brazil, Pure and Applied Geophysics, 176, 737–750, https://doi.org/10.1007/s00024-018-2019-2, 2019.

Morgan, F. D. and Lesmes, D. P.: Inversion for dielectric relaxation spectra, The Journal of Chemical Physics, 100, 671–681, https://doi.org/10.1063/1.466932, 1994.

Mosegaard, K. and Tarantola, A.: Monte Carlo sampling of solutions to inverse problems, Journal of Geophysical Research: Solid Earth, 100, 12 431–12 447, https://doi.org/10.1029/94JB03097, 1995.

Mosegaard, K., Tarantola, A., et al.: Probabilistic approach to inverse problems, International Geophysics Series, 81, 237–268, https://doi.org/10.1016/S0074-6142(02)80219-4, 2002.

Mudler, J., Hördt, A., Kreith, D., Sugand, M., Bazhin, K., Lebedeva, L., and Radić, T.: Broadband spectral induced polarization for the detection of Permafrost and an approach to ice content estimation - a case study from Yakutia, Russia, The Cryosphere, 16, 4727–4744, https://doi.org/10.5194/tc-16-4727-2022, 2022.

Muir, J. B. and Tkalčić, H.: Probabilistic joint inversion of lowermost mantle P-wave velocities and core mantle boundary topography using differential travel times and hierarchical Hamiltonian Monte-Carlo sampling, AGU Fall Meeting Abstracts, 2015, S14A–03, 2015.

Muir, J. B. and Tkalčić, H.: Probabilistic lowermost mantle P-wave tomography from hierarchical Hamiltonian Monte Carlo and model parametrization cross-validation, Geophysical Journal International, 223, 1630–1643, https://doi.org/10.1093/gji/ggaa397, 2020.

Nabighian, M. N. and Elliot, C. L.: Negative induced-polarization effects from layered media, Geophysics, 41, 1236–1255, https://doi.org/10.1190/1.2035915, 1976.

Neal, R. M. et al.: MCMC using Hamiltonian dynamics, Handbook of markov chain monte carlo, 2, 2, https://doi.org/10.48550/arXiv.1206.1901, 2011.

Nordsiek, S. and Weller, A.: A new approach to fitting induced-polarization spectra, Geophysics, 73, F235–F245, https://doi.org/10.1190/1.2987412, 2008.

Oldenburg, D. W. and Li, Y.: Inversion of induced polarization data, Geophysics, 59, 1327–1341, https://doi.org/10.1190/1.1443692, 1994.

OpenStreetMap contributors: Planet dump retrieved from https://planet.osm.org, https://www.openstreetmap.org, 2017.

Oristaglio, M. and Worthington, M.: Inversion of surface and borehole electromagnetic data for two-dimensional electrical conductivity models, Geophysical Prospecting, 28, 633–657, https://doi.org/10.1111/j.1365-2478.1980.tb01248.x, 1980.

Pelton, W. H., Ward, S., Hallof, P., Sill, W., and Nelson, P. H.: Mineral discrimination and removal of inductive coupling with multifrequency IP, Geophysics, 43, 588–609, https://doi.org/10.1190/1.1440839, 1978.

Peng, R., Yogeshwar, P., Liu, Y., and Hu, X.: Transdimensional Markov Chain Monte Carlo joint inversion of direct current resistivity and transient electromagnetic data, Geophysical Journal International, 224, 1429–1442, https://doi.org/10.1093/gji/ggaa535, 2021.

Peng, R., Han, B., Hu, X., Li, J., and Liu, Y.: 2-D probabilistic inversion of MT data and uncertainty quantification using the Hamiltonian Monte Carlo method, Geophysical Journal International, 237, 1826–1841, https://doi.org/10.1093/gji/ggae131, 2024.

Picinbono, B.: Second-order complex random vectors and normal distributions, IEEE Transactions on Signal Processing, 44, 2637–2640, https://doi.org/10.1109/78.539051, 1996.

Placencia-Gómez, E., Slater, L., Ntarlagiannis, D., and Binley, A.: Laboratory SIP signatures associated with oxidation of disseminated metal sulfides, Journal of Contaminant Hydrology, 148, 25–38, https://doi.org/10.1016/j.jconhyd.2013.02.007, 2013.

Press, F.: Earth models obtained by Monte Carlo inversion, Journal of Geophysical Research, 73, 5223–5234, https://doi.org/10.1029/JB073i016p05223, 1968.

Ramirez, A. L., Nitao, J. J., Hanley, W. G., Aines, R., Glaser, R. E., Sengupta, S. K., Dyer, K. M., Hickling, T. L., and Daily, W. D.: Stochastic inversion of electrical resistivity changes using a Markov Chain Monte Carlo approach, Journal of Geophysical Research: Solid Earth, 110, https://doi.org/10.1029/2004JB003449, 2005.

Revil, A., Koch, K., and Holliger, K.: Is it the grain size or the characteristic pore size that controls the induced polarization relaxation time of clean sands and sandstones?, Water Resources Research, 48, https://doi.org/10.1029/2011WR011561, 2012.

Revil, A., Florsch, N., and Mao, D.: Induced polarization response of porous media with metallic particles—Part 1: A theory for disseminated semiconductors, Geophysics, 80, D525–D538, https://doi.org/10.1190/geo2014-0577.1, 2015.

Revil, A., Vaudelet, P., Su, Z., and Chen, R.: Induced polarization as a tool to assess mineral deposits: A review, Minerals, 12, 571, https://doi.org/10.3390/min12050571, 2022.

Rodi, W. L.: A technique for improving the accuracy of finite element solutions for magnetotelluric data, Geophysical Journal International, 44, 483–506, https://doi.org/10.1111/j.1365-246X.1976.tb03669.x, 1976.

Römhild, L., Fiandaca, G., and Bayer, P.: Joint inversion of induced polarization and hydraulic tomography data for hydraulic conductivity imaging, Geophysical Journal International, 238, ggae197, https://doi.org/10.1093/gji/ggae197, 2024.

Roudsari, M. S., Ghanati, R., and Bérubé, C. L.: Spectral Induced Polarization Tomography Inversion: Hybridizing Homotopic Continuation with Bayesian Inversion, Geophysics, 89, 1–63, https://doi.org/10.1190/geo2023-0644.1, 2024.

Rücker, C., Günther, T., and Wagner, F. M.: pyGIMLi: An open-source library for modelling and inversion in geophysics, Computers and Geosciences, 109, 106–123, https://doi.org/10.1016/j.cageo.2017.07.011, 2017.

Sambridge, M. and Mosegaard, K.: Monte Carlo methods in geophysical inverse problems, Reviews of Geophysics, 40, 3–1, https://doi.org/10.1029/2000RG000089, 2002.

Sasaki, Y. and Matsuo, K.: Surface-to-tunnel resistivity tomography at a copper mine, SEG Technical Program Expanded Abstracts, 1990, 550–553, https://doi.org/10.1190/1.1890260, 1990.

Seigel, H., Nabighian, M., Parasnis, D. S., and Vozoff, K.: The early history of the induced polarization method, The Leading Edge, 26, 312–321, https://doi.org/10.1190/1.2715054, 2007.

Seigel, H. O.: Mathematical formulation and type curves for induced polarization, Geophysics, 24, 547–565, https://doi.org/10.1190/1.1438625, 1959.

Sen, M. K. and Biswas, R.: Transdimensional seismic inversion using the reversible jump Hamiltonian Monte Carlo algorithm, Geophysics, 82, R119–R134, https://doi.org/10.1190/geo2016-0010, 2017.

Sen, M. K. and Stoffa, P. L.: Bayesian inference, Gibbs' sampler and uncertainty estimation in geophysical inversion, Geophysical Prospecting, 44, 313–350, https://doi.org/10.1111/j.1365-2478.1996.tb00152.x, 1996.

Shaw, R. and Srivastava, S.: Particle swarm optimization: A new tool to invert geophysical data, Geophysics, 72, F75–F83, https://doi.org/10.1190/1.2432481, 2007.

Slater, L., Ntarlagiannis, D., and Wishart, D.: On the relationship between induced polarization and surface area in metal-sand and clay-sand mixtures, Geophysics, 71, A1–A5, https://doi.org/10.1190/1.2187707, 2006.

Sogade, J. A., Scira-Scappuzzo, F., Vichabian, Y., Shi, W., Rodi, W., Lesmes, D. P., and Morgan, F. D.: Induced-polarization detection and mapping of contaminant plumes, Geophysics, 71, B75–B84, https://doi.org/10.1190/1.2196873, 2006.

Sorber, L., Barel, M. V., and Lathauwer, L. D.: Unconstrained optimization of real functions in complex variables, SIAM Journal on Optimization, 22, 879–898, https://doi.org/10.1137/110832124, 2012.

Spearman, C.: The proof and measurement of association between two things., Appleton-Century-Crofts, https://doi.org/10.1037/11491-005, 1961.

Tarantola, A.: Inverse problem theory and methods for model parameter estimation, vol. 89, SIAM, 2005.

Tarasov, A. and Titov, K.: Relaxation time distribution from time domain induced polarization measurements, Geophysical Journal International, 170, 31–43, https://doi.org/10.1111/j.1365-246X.2007.03376.x, 2007.

Tezkan, B.: 2D Cole Cole Inversion of Time Domain Induced Polarization Data-Model Studies and Field Measurements, EAGE Publications BV, 2014, 1–5, https://doi.org/10.3997/2214-4609.20142042, 2014.

Tolstykh, N., Vymazalová, A., Tuhỳ, M., and Shapovalova, M.: Conditions of formation of Au–Se–Te mineralization in the Gaching ore occurrence (Maletoyvayam ore field), Kamchatka, Russia, Mineralogical Magazine, 82, 649–674, https://doi.org/10.1180/mgm.2018.84, 2018.

Tong, M., Li, L., Wang, W., and Jiang, Y.: Determining capillary-pressure curve, pore-size distribution, and permeability from induced polarization of shaley sand, Geophysics, 71, N33–N40, https://doi.org/10.1190/1.2195989, 2006a.

Tong, M., Li, L., Wang, W., and Jiang, Y.: A time-domain induced-polarization method for estimating permeability in a shaly sand reservoir, Geophysical Prospecting, 54, 623–631, https://doi.org/10.1111/j.1365-2478.2006.00568.x, 2006b.

Tso, C.-H. M., Kuras, O., Wilkinson, P. B., Uhlemann, S., Chambers, J. E., Meldrum, P. I., Graham, J., Sherlock, E. F., and Binley, A.: Improved characterisation and modelling of measurement errors in electrical resistivity tomography (ERT) surveys, Journal of Applied Geophysics, 146, 103–119, https://doi.org/10.1016/j.jappgeo.2017.09.009, 2017.

Tso, C.-H. M., Iglesias, M., and Binley, A.: Ensemble Kalman inversion of induced polarization data, Geophysical Journal International, 236, 1877–1900, https://doi.org/10.1093/gji/ggae012, 2024.

Van Voorhis, G., Nelson, P., and Drake, T.: Complex resistivity spectra of porphyry copper mineralization, Geophysics, 38, 49–60, https://doi.org/10.1190/1.1440333, 1973.

Vanhala, H.: Mapping oil-contaminated sand and till with the spectral induced polarization (SIP) method, Geophysical prospecting, 45, https://doi.org/10.1046/j.1365-2478.1997.00338.x, 1997.

Vehtari, A., Gelman, A., Simpson, D., Carpenter, B., and Bürkner, P.-C.: Rank-normalization, folding, and localization: An improved R-hat for assessing convergence of MCMC (with discussion), Bayesian analysis, 16, 667–718, https://doi.org/10.1214/20-BA1221, 2021.

Vinciguerra, A., Aleardi, M., Hojat, A., and Stucchi, E.: Discrete cosine transform for parameter space reduction in Bayesian ERT inversion, in: NSG2020 26th European Meeting of Environmental and Engineering Geophysics, vol. 2020, pp. 1–5, European Association of Geoscientists & Engineers, https://doi.org/10.3997/2214-4609.202020047, 2020.

Vinegar, H. and Waxman, M.: Induced polarization of shaly sands, Geophysics, 49, 1267–1287, https://doi.org/10.1190/1.1441755, 1984.

Volchkov, A. and Zvezdov, V.: The nature of Cu-As mineralization occurrences in the Maletoyvayamsky stratovolcano, RUDY I METALLY, pp. 44–51, 1997.

Wagner, F. M. and Uhlemann, S.: An overview of multimethod imaging approaches in environmental geophysics, Advances in Geophysics, 62, 1–72, https://doi.org/10.1016/bs.agph.2021.06.001, 2021.

Wagner, F. M., Mollaret, C., Günther, T., Kemna, A., and Hauck, C.: Quantitative imaging of water, ice and air in permafrost systems through petrophysical joint inversion of seismic refraction and electrical resistivity data, Geophysical Journal International, 219, 1866–1875, https://doi.org/10.1093/gji/ggz402, 2019.

Wang, H., Zimmermann, E., Weigand, M., Vereecken, H., and Huisman, J. A.: Comparison of different inversion strategies for electrical impedance tomography (EIT) measurements, Geophysical Journal International, p. ggad398, https://doi.org/10.1093/gji/ggad398, 2023.

Waxman, M. H. and Smits, L.: Electrical conductivities in oil-bearing shaly sands, Society of Petroleum Engineers Journal, 8, 107–122, https://doi.org/10.2118/1863-A, 1968.

Weigand, M. and Kemna, A.: Debye decomposition of time-lapse spectral induced polarisation data, Computers & Geosciences, 86, 34–45, https://doi.org/10.1016/j.cageo.2015.09.021, 2016.

Weigand, M. and Kemna, A.: Multi-frequency electrical impedance tomography as a non-invasive tool to characterize and monitor crop root systems, Biogeosciences, 14, 921–939, https://doi.org/10.5194/bg-14-921-2017, 2017.

Weigand, M. and Kemna, A.: Imaging and functional characterization of crop root systems using spectroscopic electrical impedance measurements, Plant and Soil, 435, 201–224, https://doi.org/10.1007/s11104-018-3867-3, 2019.

Weigand, M., Orozco, A. F., and Kemna, A.: Reconstruction quality of SIP parameters in multi-frequency complex resistivity imaging, Near Surface Geophysics, 15, 187–199, https://doi.org/10.3997/1873-0604.2016050, 2017.

Weigand, M., Zimmermann, E., Michels, V., Huisman, J. A., and Kemna, A.: Design and operation of a long-term monitoring system for spectral electrical impedance tomography (sEIT), Geoscientific Instrumentation, Methods and Data Systems, 11, 413–433, https://doi.org/10.5194/gi-11-413-2022, 2022.

Weller, A., Gruhne, M., Börner, F. D., and Seichter, M.: Monitoring hydraulic experiments by complex conductivity tomography, Society of Exploration Geophysicists, pp. 745–754, https://doi.org/10.4133/1.2922452, 1996a.

Weller, A., Seichter, M., and Kampke, A.: Induced-polarization modelling using complex electrical conductivities, Geophysical Journal International, 127, 387–398, https://doi.org/10.1111/j.1365-246X.1996.tb04728.x, 1996b.

Weller, A., Slater, L., Nordsiek, S., and Ntarlagiannis, D.: On the estimation of specific surface per unit pore volume from induced polarization: A robust empirical relation fits multiple data sets, Geophysics, 75, WA105–WA112, https://doi.org/10.1190/1.3471577, 2010.

Weller, A., Slater, L., and Nordsiek, S.: On the relationship between induced polarization and surface conductivity: Implications for petrophysical interpretation of electrical measurements, Geophysics, 78, D315–D325, https://doi.org/10.1190/geo2013-0076.1, 2013.

Weller, A., Slater, L., Huisman, J. A., Esser, O., and Haegel, F.-H.: On the specific polarizability of sands and sand-clay mixtures, Geophysics, 80, A57–A61, https://doi.org/10.1190/geo2014-0509.1, 2015.

Wenzel, T., Bell, R., Dietze, M., and Schrott, L.: Persistent post-flood hillslope activity posing a potential landslide dam hazard in the Ahr valley, Germany, Environmental Sciences Europe, 36, 158, https://doi.org/10.1186/s12302-024-00985-8, 2024.

West, R. M., Aykroyd, R. G., Meng, S., and Williams, R. A.: Markov chain Monte Carlo techniques and spatial–temporal modelling for medical EIT, Physiological measurement, 25, 181, https://doi.org/10.1088/0967-3334/25/1/025, 2004.

Whiteley, J., Chambers, J., Uhlemann, S., Wilkinson, P. B., and Kendall, J.: Geophysical monitoring of moisture-induced landslides: A review, Reviews of Geophysics, 57, 106–145, https://doi.org/10.1029/2018RG000603, 2019.

Williams, K. H., Kemna, A., Wilkins, M. J., Druhan, J., Arntzen, E., N'Guessan, A. L., Long, P. E., Hubbard, S. S., and Banfield, J. F.: Geophysical monitoring of coupled microbial and geochemical processes during stimulated subsurface bioremediation, Environmental science & technology, 43, 6717–6723, https://doi.org/10.1021/es900855j, 2009.

Wolpert, D. H. and Macready, W. G.: No free lunch theorems for optimization, IEEE transactions on evolutionary computation, 1, 67–82, https://doi.org/10.1109/4235.585893, 1997.

Wong, J.: An electrochemical model of the induced-polarization phenomenon in disseminated sulfide ores, Geophysics, 44, 1245–1265, https://doi.org/10.1190/1.14410050, 1979.

Yuval, D. and Oldenburg, W.: DC resistivity and IP methods in acid mine drainage problems: results from the Copper Cliff mine tailings impoundments, Journal of Applied Geophysics, 34, 187–198, https://doi.org/10.1016/0926-9851(95)00020-8, 1996.

Zhang, X., Curtis, A., Galetti, E., and De Ridder, S.: 3-D Monte Carlo surface wave tomography, Geophysical Journal International, 215, 1644–1658, https://doi.org/10.1093/gji/ggy362, 2018.

Zhao, X. and Curtis, A.: Variational prior replacement in Bayesian inference and inversion, Geophysical Journal International, 239, 1236–1256, https://doi.org/10.1093/gji/ggae334, 2024.

Zhao, Z. and Sen, M. K.: A gradient-based Markov chain Monte Carlo method for full-waveform inversion and uncertainty analysis, Geophysics, 86, R15–R30, https://doi.org/10.1190/geo2019-0585.1, 2021.

Zimmermann, E., Kemna, A., Berwix, J., Glaas, W., Münch, H., and Huisman, J.: A high-accuracy impedance spectrometer for measuring sediments with low polarizability, Measurement Science and Technology, 19, 105 603, https://doi.org/10.1088/0957-0233/19/10/105603, 2008.

Zunino, A., Ghirotto, A., Armadillo, E., and Fichtner, A.: Hamiltonian Monte Carlo probabilistic joint inversion of 2D (2.75 D) gravity and magnetic data, Geophysical Research Letters, 49, e2022GL099 789, https://doi.org/10.1029/2022GL099789, 2022.

# Abbreviations and symbols

## Abbreviations

| | |
|---|---|
| CC | Cole-Cole |
| CPA | Constant phase angle |
| CR | Complex resistivity |
| DD | Debye decomposition |
| EDL | Electrical double layer |
| ERT | Electrical resistivity tomography |
| FD | Frequency domain |
| FE | Finite element |
| FEM | Finite-element modeling |
| HMC | Hamiltonian Monte Carlo |
| HS | High sulfidation |
| IP | Induced polarization |
| MAP | Maximum a posteriori |
| McMC | Markov chain Monte Carlo |
| MH | Metropolis Hastings |
| MOF | Maletoyvaemskoie ore field |
| NUTS | No-U Turn sampler |
| PSRF | Potential-scale reduction factor |
| RMSE | Root-mean square error |
| RTD | Relaxation-time distribution |
| TD | Time domain |
| WLSQ | Weighted-least squares |

## Symbols

| | |
|---|---|
| $\tilde{\mathbf{a}} = \mathbf{a}' + i\mathbf{a}''$ | Complex value |
| $\tilde{\mathbf{a}}^*$ | Complex conjugate |
| $\tilde{\mathbf{a}}^H$ | Conjugate transpose |
| $\mathbb{C}$ | Set of complex numbers |
| $\tilde{\mathbf{C}} = E(\tilde{\mathbf{x}}\tilde{\mathbf{x}}^T)$ | Complex covariance matrix |

| | |
|---|---|
| $Cov(\cdot,\cdot)$ | Covariance operator |
| $\mathbf{C}_{\mathbf{y}}$ | Covariance matrix of $\mathbf{y}$ |
| $\tilde{\mathbf{D}}$ | Displacement flux |
| $\mathbf{d}$ | Data vector |
| $\bar{d}_c$ | Mean correlation distance |
| $\tilde{e}$ | Complex error |
| $E(\cdot)$ | Expected value |
| $\tilde{\mathbf{E}}$ | Electric field |
| $\varepsilon$ | Step length |
| $\eta(t)$ | Normalized induced polarization transient |
| $\tilde{\epsilon}$ | Complex permittivity |
| $\mathbf{f}(\cdot)$ | Forward operator |
| $\tilde{\mathbf{\Gamma}} = E(\tilde{\mathbf{x}}\tilde{\mathbf{x}}^H)$ | Complex relation matrix |
| $\mathbf{G}$ | Linear forward operator / Jacobian matrix |
| $\mathbf{G}_q$ | Jacobian matrix at iteration $q$ |
| $\gamma_k$ | Contribution of $k-$th Debye term to the superposition |
| $H = U + K$ | Hamiltonian |
| $\tilde{\mathbf{H}}$ | Magnetic field |
| $\mathbf{I}$ | Identity matrix |
| $i = \sqrt{-1}$ | Imaginary unit |
| $\tilde{\mathbf{J}}_s$ | Complex source current density |
| $K$ | Kinetic energy |
| $k$ | Geometric factor of 4-point configuration |
| $\lambda$ | Regularization strength |
| $\mathbf{m}$ | Model vector |
| $\mathbf{M}$ | Mass matrix |
| $M_a$ | Apparent chargeability |
| $M_{tot}$ | Total chargeability |
| $\mathcal{N}(\text{mean}, \text{covariance})$ | Normal distribution |
| $\mathbf{p}$ | Momentum of particle |
| $p(\mathbf{x})$ | Probability of $\mathbf{x}$ |
| $p(\mathbf{x}\|\mathbf{y})$ | Conditional probability of $\mathbf{x}$ given $\mathbf{y}$ |
| $\Phi$ | Porosity |
| $\phi$ | Phase of complex conductivity |
| $\varphi$ | Phase of complex impedance |
| $\Psi$ | Cost function |
| $\hat{\Psi}$ | Approximated cost function |
| $\tilde{\psi}$ | Complex electric potential |
| $R$ | Resistance |
| $r$ | Pearson correlation coefficient |
| $r_s$ | Spearman correlation coefficient |
| $\mathbb{R}$ | Set of real numbers |
| $\mathbf{R}_{\mathbf{x}}$ | Inverse covariance matrix for random variable $\mathbf{x}$ |
| $\tilde{\rho}$ | Complex electrical resistivity |

| | |
|---|---|
| $\tilde{\rho}_a$ | Apparent complex electrical resistivity |
| $\varrho$ | Electric charge density |
| $\tilde{\sigma}$ | Complex electrical conductivity |
| $\tilde{\sigma}_a$ | Apparent complex electrical conductivity |
| $S_w$ | Water saturation |
| $\mathrm{std}(\cdot)$ | Standard deviation operator |
| $t$ | time (fictitious in the context of HMC) |
| $T(\mathbf{x}_j \| \mathbf{x}_i)$ | Transition probability from state $\mathbf{x}_i$ to state $\mathbf{x}_j$ |
| $\tau$ | Relaxation time |
| $U$ | Potential energy |
| $V$ | Voltage |
| $\mathrm{var}(\cdot)$ | Variance |
| $\tilde{\mathbf{W}}_{\mathbf{d}}$ | Data weighting matrix |
| $\tilde{\mathbf{W}}_{\mathbf{m}}$ | Model weighting matrix |
| $\omega$ | Angular frequency |
| $\nabla_{\mathbf{x}} U$ | Gradient of potential energy |
| $\mathbf{x}$ | State |
| $\Delta \mathbf{x}_q$ | State update for iteration $q$ |
| $\mathbf{x}^+$ | Proposed state during random walk update |
| $\mathbf{x}_p$ | Prior state |
| $\mathbf{y}$ | Observations |
| $\tilde{Z}$ | Complex electrical impedance |